

FREE ELECTRON LASER ABLATION OF SOFT TISSUE: THE EFFECTS
OF CHROMOPHORE AND PULSE CHARACTERISTICS
ON ABLATION MECHANICS

By

STEPHEN R. UHLHORN

Dissertation

Submitted to the Faculty of the
Graduate School of Vanderbilt University
in partial fulfillment of the requirements
for the degree of

DOCTOR OF PHILOSOPHY

in

Biomedical Engineering

August, 2002

Nashville, Tennessee

Approved By:

Professor E. Duco Jansen
Professor Robert Roselli
Professor Robert Galloway
Professor Richard Haglund
Professor Peter Konrad
Dr. Richard London

Copyright 2002 by Stephen R. Uhlhorn
All rights reserved.

*This dissertation is dedicated to the memory of
Roger W. Uhlhorn.*

ACKNOWLEDGEMENTS

First of all, I would like to thank my dissertation committee for giving me enough guidance and direction to keep me on the right track, while still allowing me to fully explore and develop the research. Special thanks go to Dr. Richard A. London of Lawrence Livermore National Laboratory who served on my committee. His support of the research project went well beyond the modeling effort at LLNL, and the time I spent working at the laboratory has allowed me to gain experience in areas I would not have been exposed to otherwise.

To my advisor, Dr. Duco Jansen, I am especially thankful for giving me the freedom to develop the research independently, and to make mistakes, because only through these mistakes does one really learn and gain solid understanding. Furthermore, the Biomedical Optics Laboratory that has been developed by Dr. Jansen in the Free Electron Laser Center has always been a fun place to do research.

I would also like to thank Dr. Hans Pratisto, who served as a Post-Doctoral Fellow during my initial time in the program. I credit Dr. Pratisto with teaching me so many of the practical laboratory techniques that are invaluable in optical experiments and research. Special thanks go to the entire staff of the Free Electron Laser Center, including the engineers and operators, who have done a phenomenal job of turning the FEL into a stable, reliable device. The staff of the center has also been a source of information and expertise, in all areas technical, and to that, I am grateful.

Finally, I would also like to thank my family, whose encouragement helped me get through the difficult times, and my wife Carolyn, whose support and infinite patience has allowed me to complete this work.

TABLE OF CONTENTS

	Page
DEDICATION	iii
ACKNOWLEDGEMENTS	iv
LIST OF FIGURES	viii
LIST OF TABLES	1
Chapter	
I. INTRODUCTION	2
I.1 Motivation	2
I.2 Research Objectives	3
I.3 Overview of Dissertation	4
I.4 Original Contribution	5
II. BACKGROUND	6
II.1 Laser Ablation of Soft Biological Tissues	6
II.1.1 UV Photoablation	6
II.1.2 IR Photoablation	6
II.2 FEL Ablation of Soft Tissues	7
II.2.1 Effect of Protein Absorption	7
II.2.2 Effect of Pulse Characteristics	9
References	13
III. FREE ELECTRON LASER ABLATION OF SKIN: MEASUREMENT OF ABLATION DEPTH AND THRESHOLD	14
III.1 Introduction	16
III.1.1 Ablation Threshold	17
III.1.2 Steady-State Ablation	18
III.2 Materials and Methods	19
III.2.1 Tissue Samples	19

III.2.2	Laser Source and Delivery	20
III.2.3	Ablation Threshold Measurements	20
III.2.4	Ablation Depth Measurements	22
III.3	Results	22
III.3.1	Rat Dermis FTIR	22
III.3.2	Ablation Threshold Measurements	24
III.3.3	Ablation Depth Measurements	24
III.4	Discussion	28
III.4.1	FTIR Spectrum	28
III.4.2	Ablation Threshold Measurements	28
III.4.3	Plume Screening	32
III.4.4	Heat of Ablation	32
III.4.5	Dynamic Absorption	33
III.4.6	Protein Absorption	34
III.5	Conclusions	34
	Acknowledgements	35
	References	37

IV. THE EFFECT OF PROTEIN ABSORPTION AND MECHANICAL STRENGTH

	IN THE ABLATION OF SOFT TISSUE WITH A FREE ELECTRON LASER	38
IV.1	Introduction	40
IV.2	Background	43
IV.2.1	Thermoelastic Stress	43
IV.2.2	Steady-State Surface Vaporization	44
IV.2.3	Explosive Characteristics of IR Ablation	46
IV.3	Experimental Methods	46
IV.4	Results	48
IV.4.1	Acoustic Cross-Calibration	48
IV.4.2	Peak Pressure Measurements	48
IV.5	Discussion	49
IV.5.1	Acoustic Measurements in Air	49
IV.5.2	Surface Mediated Ablation	50
IV.5.3	Role of Protein Absorption	50
IV.6	Conclusions	52
	Acknowledgements	53
	References	55

V.	MODELING THE EFFECTS OF PULSE STRUCTURE AND DYNAMIC ABSORPTION DURING FREE ELECTRON LASER ABLATION OF SOFT TISSUE	62
V.1	Introduction	63
V.2	Modelling Methods	64
	V.2.1 Laser Irradiation	65
	V.2.2 Absorption Model	66
V.3	Simulation Results	67
	V.3.1 Ablation Time	67
	V.3.2 Effect of Pulse Structure	67
	V.3.3 Effect of Dynamic Absorption	69
	V.3.4 Effect of Pulse Duration	69
V.4	Discussion	75
	V.4.1 Pulse Structure	75
	V.4.2 Dynamic Absorption	78
V.5	Conclusions	78
	Acknowledgements	78
	References	80
VI.	CONCLUDING REMARKS	81
VI.1	Summary	81
VI.2	Future Directions	84
Appendix		
A.	BEAM DELIVERY OF THE VANDERBILT FREE ELECTRON LASER WITH HOLLOW WAVE GUIDES: EFFECT ON TEMPORAL AND SPATIAL PULSE PROPAGATION	85
A.1	Introduction	87
A.2	Materials and Methods	87
	A.2.1 Characteristics of the Vanderbilt Free Electron Laser	87
	A.2.2 Pulse width and beam profile measurement	88
A.3	Results	90
A.4	Discussion	91
A.5	Conclusion	102
	Acknowledgements	102
	References	103

LIST OF FIGURES

Figure	Page
II.1	Conditions for energy confinement in water. 11
III.1	Experimental setup for the measurement of ablation threshold. 21
III.2	Normalized rat dermis FTIR absorption spectrum. 23
III.3	Probit measurement of rat dermis surface ablation threshold. 25
III.4	Rat dermis ablation threshold as a function of wavelength. 26
III.5	Rat dermis ablation threshold as a function of tissue absorption coefficient. . . 27
III.6	Rat skin ablation depth as a function of wavelength. 29
III.7	Rat skin ablation depth as a function of the tissue absorption coefficient. . . . 30
IV.1	Experimental setup for measuring the peak pressure generated during FEL irradiation. 56
IV.2	Cross-calibration of piezoelectric microphone and piezoelectric needle hydrophone. 57
IV.3	Recorded peak pressure as a function of radiant exposure at 3.3 μm in gelatin and rat dermis. 58
IV.4	Recorded peak pressure as a function of radiant exposure at 6.45 μm in gelatin and rat dermis. 59
IV.5	Model fit of peak pressure as a function of radiant exposure at 3.3 μm in gelatin and rat dermis. 60

IV.6	Model fit of peak pressure as a function of radiant exposure at $6.45 \mu\text{m}$ in gelatin and rat dermis.	61
V.1	Surface zone velocity as a function of time for laser pulses below and above the threshold for ablation.	68
V.2	Pressure profile in the mesh during laser irradiation.	70
V.3	Expanded view of the pressure profile near the surface.	71
V.4	Effect of pulse structure on the ablation threshold.	72
V.5	Absorption coefficient as a function of mesh depth for two absorption models.	73
V.6	Effect of dynamic absorption on the ablation threshold.	74
V.7	Normalized ablation time for multiple pulse durations.	76
V.8	Effect of pulse duration on the ablation time.	77
A.1	Setup for beam profile and pulse width measurement.	89
A.2	Beam profile and micropulse width measured after transmission through a $250 \mu\text{m}$ straight HWG. Coupling is aligned for optimal mode propagation.	93
A.3	Beam profile and micropulse width measured propagating in a misaligned $250 \mu\text{m}$ straight HWG.	94
A.4	Transmission through a straight $250 \mu\text{m}$ HWG (length = 1.5 m).	95
A.5	Beam profile and micropulse width measured after transmission through a $530 \mu\text{m}$ straight HWG.	96
A.6	Beam profile and micropulse width measured after transmission through a $530 \mu\text{m}$ HWG bent through two loops (720° , bending radius = 9 cm.)	97

A.7	Transmission through a straight and bent $530\ \mu\text{m}$ HWG (length = 1.5 m, bending through 2 loops, bending radius 9 cm.)	98
A.8	Pulse broadening caused by propagation of a 1 ps FEL micropulse through 1.5 m HWG. Shown are the results of waveguides with bore sizes of $250\ \mu\text{m}$ and $530\ \mu\text{m}$, and theoretical pulse broadening based on a simple theoretical model.	101

LIST OF TABLES

Table	Page
A.1 Overview of the coupling conditions used in the experiments.	92

CHAPTER I

INTRODUCTION

I.1 MOTIVATION

The Vanderbilt University Mark-III Free Electron Laser (FEL) is a continuously tunable source of pulsed mid-infrared (IR) radiation with a tuning range of $\lambda \approx 2 - 10 \mu\text{m}$. The wavelength tunability of the FEL makes it an excellent research tool for investigating the feasibility of new medical laser procedures. Traditionally, the choice of laser wavelengths for a medical procedure has been limited to commercially available laser systems with a fixed wavelength. With the FEL comes the possibility of choosing a wavelength based on the requirements of the procedure and the desired outcome, rather than the more common practice of developing a procedure around the available laser sources in a “reverse-engineered” fashion. Because of the considerable flexibility that the FEL provides, it is well suited to aid the development of novel procedures. However, FEL’s are large, expensive devices which require extensive expertise just to operate, and are not likely to be found in every operating room. Consequently, the development model of surgical procedures employed in the FEL center involves using the FEL to determine the ideal laser parameters for a given procedure, and then having industrial partners develop compact, less expensive systems that are designed to produce the best clinical outcome for a specific procedure.

The ability to design a medical laser procedure that results in the best clinical outcome relies on having a thorough knowledge of the role of all the laser parameters in a procedure. This can only be done when there is a clear understanding of the mechanism of interaction of the laser light with the tissue. Laser tissue interactions can loosely be classified into photothermal, photomechanical, or photochemical interactions, however, most interactions do not fall clearly into one of these categories, and often multiple processes are competing with each other. Hence, it is extremely difficult to unravel the mechanism of interaction. To date, many studies have been carried out (see chapter II) investigating the effects of FEL irradiation on biological tissues, but the results of these studies have not presented a clear picture of the mechanism involved, and in many cases, conflict with each other. Despite the lack of a clear understanding of the processes involved, the Vanderbilt FEL is currently being used in a clinical setting to test the feasibility of its use in human neurosurgical and ophthalmic procedures.

I.2 RESEARCH OBJECTIVES

The overall goal of this research project is to gain a deeper understanding of the processes involved in the ablation of soft tissues with the FEL. An investigation into the mechanism of laser ablation of biological tissues is a complicated problem in itself, but it is made more so due to the nature of the FEL characteristics. For example, while the wavelength tunability of the laser provides much flexibility for investigating potential applications, it complicates basic investigations on the interaction mechanism since changing the laser wavelength can potentially change the chromophore and absorption properties for a given sample. In the mid-IR spectrum, most soft tissues are primarily composed of water, however, several prominent protein absorption lines exist as well, and one can expect that the interaction mechanism and ablation mechanics would be significantly different depending on the acting chromophore. Further, the pulse characteristics of the FEL place it in a unique temporal regime. The pulse consists of a $\approx 5 \mu\text{s}$ macropulse that consists of a 3 GHz train of micropulses with a 1 ps duration. This pulse structure presents the possibility of producing a number of types of interactions, ranging from purely photothermal, to possibly photomechanical effects due to the short duration micropulses.

Several studies have been published (see chapter II) suggesting that protein absorption plays a major role in the ablation of soft tissues with the FEL, however the effect of the temporal pulse characteristics of the FEL have been largely ignored. The working hypothesis of this dissertation is that the unique pulse structure of the FEL plays a role in the ablation of soft tissues, and the high-quality ablations that are typically observed can not be explained by the selective absorption of the FEL radiation by tissue protein alone.

In order to fulfill the overall research goal, several techniques have been employed to investigate the ablation process from a variety of standpoints, in the hope that a consistent picture of the process can be drawn. First, an integrative view of the ablation process is taken by looking at the macroscopic effects of soft tissue ablation with the FEL over a broad range of wavelengths to get an overall picture of the process. This was done by analyzing the depth of the craters produced by the ablation of soft tissue. Second, a more detailed view is taken by investigating the ablation dynamics at specific wavelengths. The acoustic stresses that are generated from FEL irradiation of soft tissue are analyzed to reveal information about the dynamics involved in the process. Finally, a microscopic view was taken to investigate the effects that the short micropulses have on the ablation process. This was carried out using numerical modeling which allows the study of processes on time scales that are too short to study experimentally.

I.3 OVERVIEW OF DISSERTATION

The body of this dissertation is essentially divided into three independent manuscripts that have been submitted, or prepared for submission, to peer reviewed journals. The manuscripts are preceded by some background material, and followed by some concluding remarks. Chapter II presents a brief review of the previous research that has been performed investigating tissue ablation with the FEL.

The background material is followed by Chapter III, which presents a manuscript that has been submitted for review to *Lasers in Surgery and Medicine*, titled, “Free Electron Laser Ablation of Skin: Measurement of Ablation Depth and Threshold.” This paper reports the findings of experiments in which the FEL was used to irradiate rat dermis over a broad range of wavelengths. The ablation depth and ablation threshold were measured and analyzed by applying the data to theoretical models predicting the results. The data analysis was used to draw conclusions about the overall effects of soft tissue ablation with the FEL, from an integrative viewpoint.

Chapter IV present a manuscript that has been prepared for submission to *Physics in Medicine and Biology*, titled, “The Effect of Protein Absorption and Mechanical Strength in the Ablation of Soft Tissue with a Free Electron Laser.” In this paper, the acoustic transients that are generated during FEL irradiation of gelatin and rat dermis are measured and compared to theoretical models predicting the results. By comparing the results of the analysis performed in samples with differing material properties, and at wavelengths where different chromophores dominate absorption, conclusions can be drawn about the ablation mechanics from a dynamics standpoint.

Chapter V presents a manuscript entitled, “Modeling the Effects of Pulse Structure and Dynamic Absorption During Free Electron Laser Ablation of Soft Tissue” and will be submitted to *Applied Optics*. This paper describes the results of numerical simulations that were performed to investigate the role that the FEL micropulses have on the ablation process on very short time scales. It also reports on the effect that dynamic absorption has on ablation, based on a saturation model of water.

Finally, chapter VI summarizes the work in whole, and draws conclusions about how the results of each manuscript relate to each other. It also presents suggestions for future directions to continue the research.

The body of the dissertation is followed by Appendix A, which contains a manuscript that has been published in *Fiber and Integrated Optics*. This paper reports on some aspects of a clinical beam delivery system that was designed and constructed in our laboratory, to use the FEL for neurosurgery. Specifically, a hand-held surgical probe was built using

hollow dielectric waveguides to deliver the FEL radiation to the operating field. The paper describes the effects that hollow waveguide transmission has on the FEL pulse characteristics and discusses the implications on surgical procedures. This manuscript was included as an appendix because it does not include information regarding the mechanism of tissue ablation with the FEL, however, it does represent a significant amount of time and effort that was invested at the early stages of the research project.

I.4 ORIGINAL CONTRIBUTION

The work presented in this dissertation represents a significant contribution to the laser-tissue interaction field of research. It addresses fundamental questions regarding the nature of the ablation process in soft-tissues, specifically with a free electron laser. To the best of the author's knowledge, the first quantitative evidence is presented implicating protein absorption as a major factor in IR soft tissue ablation. Furthermore, the relationship of the protein structural matrix in soft tissues and its impact on the mechanical strength of the tissue is outlined. These contributions are important because it changes the traditional view of IR soft tissue ablation being completely dependent on the optical and thermal properties of water. This work demonstrates that factors including protein absorption and material strength play a significant role in soft tissue ablation, and must be taken into account when developing models of ablation and designing clinical procedures.

CHAPTER II

BACKGROUND

II.1 LASER ABLATION OF SOFT BIOLOGICAL TISSUES

Laser ablation of soft tissues is performed routinely in clinical procedures and research experiments, however, even after years of studying the mechanisms involved in the process, questions still remain. Most soft tissues are primarily composed of a solid protein matrix that gives the tissue its mechanical strength surrounded by liquid water. Depending on the laser used and the tissue being irradiated, any one of several responses may be observed from the ablation of soft tissue, which may arise from a variety of mechanisms. Generally, the results of soft tissue ablation can be grouped by the region of the spectrum that the laser operates in; either ultraviolet (UV) or infrared (IR).

II.1.1 UV Photoablation

In UV photoablation, the primary tissue chromophore is the protein contained in the structural matrix of the tissue. The mechanism of ablation has been described by both photochemical [1] and purely photothermal models [2]. For material to be removed, bonds that hold the tissue together must be broken. The photochemical model of ablation involves the direct absorption and breakage of the bonds by high energy photons in a process termed photoablative decomposition [1], while the photothermal model involves the rapid heating and subsequent denaturation of the structural matrix which allows for tissue decomposition [2]. UV ablation of soft tissue typically appears to be a surface-mediated process that is characterized by clean margins around the ablation site with little collateral damage [3], and the material ejected during ablation appeared to be composed of a fine mist, suggesting that most of the irradiated volume had been vaporized [3]. It has also been observed that the onset of material removal occurred immediately following the incident laser pulse [2].

II.1.2 IR Photoablation

In IR photoablation, the primary tissue chromophore is the liquid water that surrounds the structural matrix. The mechanism of ablation involves a purely photothermal interaction. In one common model, the tissue water absorbs the incident radiation and is

superheated to temperatures above the boiling point of liquid water at atmospheric pressure. This leads to a phase explosion when the superheated water temperature approaches the critical temperature, which is the point at which water can no longer remain a liquid, regardless of the surrounding pressure. Material is removed by fracturing the tissue matrix, and ejecting the solid material. This explosive process is typically characterized by the mechanical tearing of tissue surrounding the ablation site [4], and observations of the ablation plume have described the ejected material as being particulate in nature [5, 6]. It has also been observed that the onset of material removal is delayed with respect to the incident laser pulse [7], suggesting that it takes some time in order for the tissue water to achieve the superheated state.

II.2 FEL ABLATION OF SOFT TISSUES

II.2.1 *Effect of Protein Absorption*

Much of the previous research investigating the mechanism of soft tissue ablation with the FEL has been focused on determining the effect of protein absorption. The results published from previous studies generally fall into one of two categories; those that support the theory that protein absorption plays an important role in the ablation process, and those that do not.

Traditionally, IR laser ablation of soft tissues has focused on using the strong water absorption peak around $\lambda = 3.0 \mu\text{m}$ to rapidly heat the tissue beyond vaporization temperatures, thereby removing tissue during this explosive process. Only recently have researchers begun to consider targeting various absorption bands of proteins as a means of laser ablation. The first of these was reported by Edwards et al. [8], where they investigated several wavelengths between $\lambda = 3.0 - 6.85 \mu\text{m}$ using cadaver cornea. It was observed that a maximum ablation yield and minimal collateral damage occurred at a wavelength of $\lambda = 6.45 \mu\text{m}$, which corresponds to the amide II absorption band of protein. These results were compared to those from $\lambda = 3.0 \mu\text{m}$ which had a lower ablation yield and more thermal damage and were explained by the fact that at $\lambda = 3.0 \mu\text{m}$, the macropulse of the FEL is not thermally confined, allowing heat to be conducted into the tissue during the laser pulse. With a penetration depth one order of magnitude greater than at $3.0 \mu\text{m}$, one would not expect to see higher ablation rates at $6.45 \mu\text{m}$. To account for this, Edwards et al. [8] originally proposed an ablation model involving a partitioning of the absorbed energy between the protein and water components of tissue. Some of the incident laser light is absorbed by the amide II bonds in protein. It was postulated that this energy heats the structural proteins of the

tissue beyond its melting point which compromises the mechanical integrity of tissue while the liquid-vapor transition of the heated water develops a pressure head driving the ablation.

Since the initial study by Edwards et al. [8], several studies have presented evidence that protein absorption does not play a significant role in the ablation process. Tribble et al. [9] investigated the ablation dynamics of gelatin which has absorption properties similar to most soft tissues. The gelatin was irradiated with several wavelengths of the FEL, including $\lambda = 3.0, 3.36,$ and $6.45 \mu\text{m}$. Pressure transients were recorded for each of these wavelengths and at radiant exposures below the ablation threshold, the stress waves followed the standard model of thermoelastic expansion. However at laser radiant exposures above threshold, two types of ablation dynamics were observed. They used shadow imaging to monitor the ablation plume with a second laser beam perpendicular to the FEL. At a wavelength of $3.0 \mu\text{m}$, a single maximum of the shadow was seen, while at both 3.36 and $6.45 \mu\text{m}$, a second maximum was resolved at later times. In addition, at 3.36 and $6.45 \mu\text{m}$ the duration of the momentum recoil was twice as long as at $3.0 \mu\text{m}$, implying that the dynamics that govern the ablation are similar for $\lambda = 3.36$ and $6.45 \mu\text{m}$. At $\lambda = 2.94 \mu\text{m}$, water is the dominant absorber in gelatin and most soft tissues, with a penetration depth of only $\approx 1 \mu\text{m}$, whereas at $6.45 \mu\text{m}$, protein represents a significant percentage of the overall absorption cross-section, and contributes to the penetration depth of $\approx 10 \mu\text{m}$. It should be noted that while protein absorption is strong at $\lambda = 6.45 \mu\text{m}$ in soft tissues, water also absorbs the incident radiation strongly as well. The wavelength $3.36 \mu\text{m}$ was chosen for study because it has the same penetration depth as at $6.45 \mu\text{m}$, but without the protein absorption. The findings by Tribble et al. [9], that at $3.0 \mu\text{m}$ the momentum recoil was much faster than at either 3.36 or $6.45 \mu\text{m}$, is not surprising since the penetration depth is an order of magnitude smaller. Furthermore, the fact that the ablation dynamics were similar for 3.36 and $6.45 \mu\text{m}$ suggests that the ablation process is governed by the overall absorption cross section of the sample, rather than the selective absorption of the individual components. However, the interpretation of the data by Tribble et al. is debatable because the irradiation conditions were not held constant from one experiment to another.

Following the lead set forth by the early investigations of the role of protein absorption in ablation, Auerhammer et al. [10] studied a wide range of IR wavelengths with the FELIX free electron laser at Rijnhuizen in the Netherlands. Using porcine cornea as a tissue model, wavelengths between $6 \leq \lambda \leq 20 \mu\text{m}$ were investigated, focusing on the range $6 \leq \lambda \leq 8 \mu\text{m}$ where protein absorption becomes significant due to the excitation of the amide (I–V) modes. They found that the ablation thresholds exhibited a clear inverse proportionality to the overall corneal absorption coefficient, which was given by the weighted sum of the absorption

coefficients of the individual chromophores according to:

$$\mu_{a,\text{cornea}} = A \cdot \mu_{a,\text{water}} + B \cdot \mu_{a,\text{protein}}, \quad (\text{II.1})$$

where A and B are the mass fractions of each chromophore, and it appeared that the laser light was absorbed homogeneously, i.e.—no preference was given to the structure of the absorber.

While some of the data presented by Auerhammer et al. [10] suggested that protein absorption plays a minimal role, the distinction of whether or not protein absorption impacts the ablation process is not so clear. Regarding the ablated mass, Auerhammer et al. [10] noticed that if protein absorption contributed to a major extent, the ablation depth was still comparable to values at wavelengths where water is the dominant absorber. Compared to measurements from Edwards et al. [8], similar ablation rates were found, however the strong increase in ablated mass at $6.45 \mu\text{m}$ as compared to other protein absorption bands was not seen. By using high-speed video imaging, Auerhammer et al. [10] viewed the size and composition of the ejected particles and water vapor during ablation. They noticed that at wavelengths where water is the only absorber ($\lambda = 14.5 \mu\text{m}$), the ejected particles appeared as large chunks, while at wavelengths where protein contributes to the absorption cross section, the particles were much smaller. Also, at $\lambda = 6.2$ and $6.45 \mu\text{m}$, it was observed that the ablation plumes appeared as a fine mist during subsequent pulses when irradiated with multiple shots. This observation was attributed to the melting of the collagen matrix, in a manner similar to the explanation put forth by Edwards et al. [8]. It should be noted that this observation is also consistent with observations of UV soft tissue ablation, where protein is the dominant chromophore. Here, it is commonly seen that the material ejected is composed of a fine mist [11], which suggests that protein absorption in the IR may play a role in the ablation process, as it does in the UV.

The data presented in these studies do not present a clear picture of the role of protein absorption in soft tissue ablation with a FEL. The interpretation of the results and conclusions drawn from the studies often conflict with each another, and the relative roles of protein absorption and the FEL pulse characteristics are still not clear.

II.2.2 Effect of Pulse Characteristics

The studies discussed thus far have investigated the effect of wavelength and chromophore on the ablation process, but have neglected to address the issue of the FEL pulse characteristics. The pulse structure of the FEL places it in a unique temporal regime. The pulse

consists of a $\approx 5 \mu\text{s}$ macropulse that consists of a 3 GHz train of micropulses with a 1 ps duration. This pulse structure presents the possibility of producing a number of types of interactions, ranging from purely photothermal, to possibly photomechanical effects due to the short duration micropulses. The type of interaction that is likely to be seen largely depends on the relationship between the absorption properties of the tissue and the laser pulse duration. Depending on the relationship between these two parameters, the irradiation of tissue can enter certain energy confinement conditions, outlined below, and summarized in Fig. II.1.

Thermal confinement in laser ablation occurs when the laser pulse duration (τ_L) is shorter than the time it takes heat to diffuse out of the irradiated volume. When the penetration depth is much less than the laser spot radius, the condition for thermal confinement is given by

$$\tau_L \leq \tau_T = \frac{\delta^2}{4\alpha}, \quad (\text{II.2})$$

where δ is the absorption depth of the laser and α is the thermal diffusivity of the tissue ($\alpha = 0.15 \text{ mm}^2/\text{s}$ for water at 37°C). For laser pulses that are thermally confined, the temperature distribution is determined by the laser light distribution [12]. In one study, Walsh and Deutsch [13] found that by keeping the pulse duration shorter than the thermal diffusion time (τ_T), the thermal damage to the surrounding tissue was minimized and the depth of thermally damaged tissue increased with increasing pulse duration. It should be noted that the FEL macropulse of $\approx 5 \mu\text{s}$ is thermally confined for all wavelengths except at the water absorption peak near $3.0 \mu\text{m}$, where here $\tau_T = 1.7 \mu\text{s}$.

When a laser pulse is shorter than the time it takes a stress wave to propagate out of an irradiated volume (τ_σ), it is said to be inertially confined. The criterion for inertial (or stress) confinement is

$$\tau_L \leq \tau_\sigma = \frac{\delta}{\sigma}, \quad (\text{II.3})$$

where δ is the absorption depth and σ is the speed of sound in tissue ($\sigma = 1500 \text{ m/s}$). An inertially confined laser pulse can generate large peak stresses that may contribute to the ablation mechanism and inflict damage to the surrounding tissue [14]. Some of the photomechanical interactions that stress confined laser pulses can elicit are the thermoelastic expansion due to the heating of the target, and the recoil caused by the forced ejection of the ablated material. The ultrashort micropulses of the FEL ($\approx 1 \text{ ps}$) are stress confined at all wavelengths. Even the micropulse separation of 350 ps is short compared to the confinement time, since at $\lambda = 3.0 \mu\text{m}$, $\tau_\sigma = 670 \text{ ps}$.

While consideration of the FEL pulse characteristics leads one to expect a photothermal or photomechanical mechanism, the ultrashort micropulse duration also led investigators

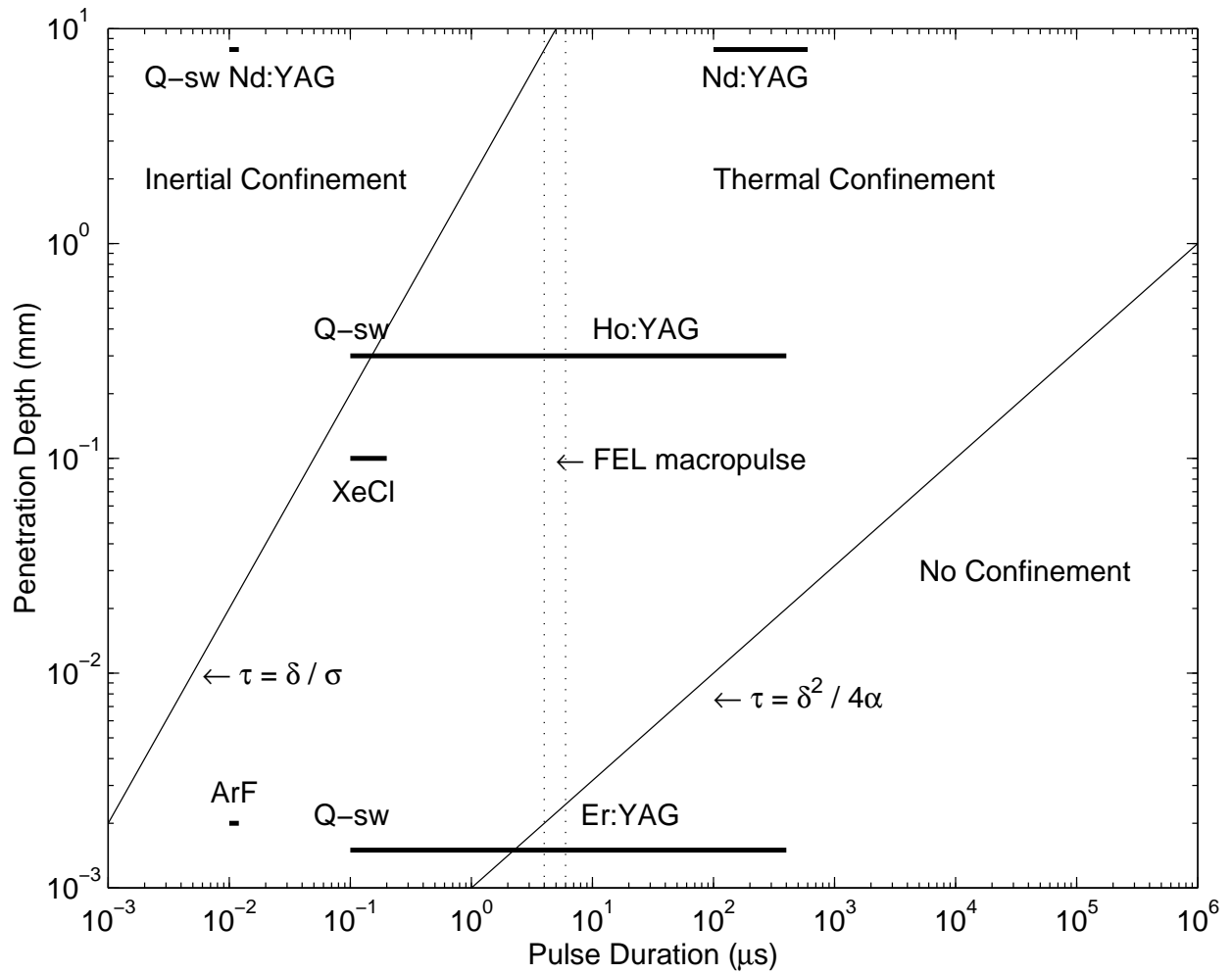


Figure II.1: Conditions for energy confinement in water with the pulse characteristics of the FEL and several other common laser systems.

to consider photochemical effects resulting from fast protein dynamics. Recently, Edwards et al. [15] compared the results of FEL irradiation with that of an optical parametric amplifier (OPA), both operating at $\lambda = 6.45 \mu\text{m}$ and containing picosecond duration micropulses, however, the OPA has a kilohertz repetition rate which reduces its average power by a factor of 10^6 compared to the FEL. Irradiation of ocular tissue with the OPA showed no observable effect, while the FEL ablated the tissue with clear, observable craters. This implied that picosecond time scale protein dynamics were not a factor in the ablation process. This led Edwards et al. [16] to refine the original proposed model of selective absorption by developing a heat diffusion model of tissue ablation that incorporates chemical kinetics of protein denaturation. Edwards concluded that the differential absorption of protein denatured the protein matrix of the tissue, thereby affecting its material strength.

A consistent picture of the processes involved in FEL ablation of soft tissues cannot be determined by the data published thus far. The interpretation of the role of protein absorption conflicts from one study to another, and even sometimes within a single set of experiments. Furthermore, the effects of the complex FEL pulse characteristics have not been sufficiently addressed to date.

REFERENCES

- [1] Srinivasan R, Dyer PE, Braren B, “Far-ultraviolet laser ablation of the cornea: Photoacoustic studies,” *Lasers in Surgery and Medicine*, 6(6):514–519, 1987.
- [2] Venugopalan V, Nishioka NS, Mikic BB, “The thermodynamic response of soft biological tissues to pulsed ultraviolet laser irradiation,” *Biophysical Journal*, 69:1259–1271, 1995.
- [3] Puliafito CA, Stern D, Kreuger RR, Mandel ER, “High-speed photography of excimer laser ablation of the cornea,” *Archives of Ophthalmology*, 105(9):1255–1259, 1987.
- [4] Cummings JP, Walsh Jr. JT, “Tissue tearing caused by pulsed laser-induced ablation pressure,” *Applied Optics*, 32(4):494–503, 1993.
- [5] Cummings JP, Walsh Jr. JT, “Q-switched laser ablation of tissue: Plume dynamics and the effect of tissue mechanical properties,” in *Laser-Tissue Interaction III*, vol. 1646, pp. 242–253, SPIE, 1992.
- [6] Walsh JT, Deutsch TF, “Measurement of Er:YAG laser ablation plume dynamics,” *Applied Physics B*, 52:217–224, 1991.

- [7] Venugopalan V, Nishioka NS, Mikic BB, “The thermodynamic response of soft biological tissues to pulsed infrared-laser irradiation,” *Biophysical Journal*, 70:2981–2993, 1996.
- [8] Edwards G, Logan R, Copeland M, Reinisch L, Davidson J, Johnson B, Maciunas R, Mendenhall M, Ossoff R, Tribble J, Werkhaven J, O’Day D, “Tissue ablation by a free-electron laser tuned to the amide II band,” *Nature*, 371:416–419, 1994.
- [9] Tribble J, Lamb DC, Reinisch L, Edwards G, “Dynamics of gelatin ablation due to free-electron laser irradiation,” *Phys. Rev. E*, 55:7385–7389, 1997.
- [10] Auerhammer JM, Walker R, van der Meer AFG, Jean B, “Dynamic behavior of photoablation products of corneal tissue in the mid-IR: A study with FELIX,” *Applied Physics B: Lasers and Optics*, 68:111–119, 1999.
- [11] Puliafito CA, Steinert RF, Deutsch TF, Hillenkamp F, Dehm EJ, Adler CM, “Excimer laser ablation of the cornea and lens,” *Ophthalmology*, 92(6):741–748, 1985.
- [12] Welch AJ, van Gemert MJC, eds., *Optical-Thermal Response of Laser-Irradiated Tissue*, chap. 21, pp. 709–763, Plenum Press, New York, 1995.
- [13] Walsh JT, Deutsch TF, “Pulsed CO₂ laser tissue ablation: Measurement of the ablation rate,” *Lasers in Surgery and Medicine*, 8:264–275, 1988.
- [14] Paltauf G, Reichel E, Schmidt-Kloiber H, “Study of different ablation models by use of high-speed-sampling photography,” in *Laser-Tissue Interaction III*, vol. 1646, pp. 343–352, SPIE, 1992.
- [15] Edwards G, Hutson MS, Hauger S, Kozub J, Shen J, Shieh C, Topadze K, Joos K, “Comparison of OPA and Mark-III FEL for tissue ablation at 6.45 μ m,” in *Commercial and Biomedical Applications of Ultrafast and Free-Electron Lasers*, Edwards GS, Neev J, Ostendorf A, Sutherland JC, eds., vol. 4633, pp. 194–200, SPIE, Bellingham, WA, USA, 2002.
- [16] Edwards GS, Hutson MS, Hauger S, “Heat diffusion and chemical kinetics in Mark-III fel tissue ablation,” in *Commercial and Biomedical Applications of Ultrafast and Free-Electron Lasers*, Edwards GS, Neev J, Ostendorf A, Sutherland JC, eds., vol. 4633, pp. 184–193, SPIE, Bellingham, WA, USA, 2002.

CHAPTER III

FREE ELECTRON LASER ABLATION OF SKIN:
MEASUREMENT OF ABLATION DEPTH AND THRESHOLD

Stephen R. Uhlhorn, Mark A. Mackanos,
and E. Duco Jansen

Vanderbilt University
Department of Biomedical Engineering
Nashville, TN

Submitted for publication to
Lasers in Surgery and Medicine

ABSTRACT

Background and Objective: Previous studies involving soft tissue ablation with a free electron laser (FEL) have arrived at somewhat conflicting results. Our goal is to investigate the mechanism of soft tissue ablation with the FEL, in order to gain a better understanding of how the numerous laser parameters may impact the clinical outcome of a given laser surgical procedure. *Materials and Methods:* The ablation depth and threshold radiant exposure were measured in rat skin dermis using the FEL over a broad range of infrared wavelengths ($\lambda = 2.65 - 6.7 \mu\text{m}$). The results of the measurements were compared to theoretical models for both the steady-state ablation depth and the ablation threshold. *Results:* The ablation threshold follows the trend predicted by a basic photothermal model and the ablation depth follows the trend predicted by a steady-state ablation depth model that includes the effect of ablation plume screening. *Conclusions:* It appears that over a very broad range of mid-infrared wavelengths, the results of soft tissue ablation with the FEL are well described by a steady-state ablation model that incorporates the effect of plume screening, and the fundamental mechanism appears to be a water absorption dominated process.

III.1 INTRODUCTION

Laser surgical procedures involving the ablation of biological tissues often benefit from a thorough understanding of the mechanism of interaction between the laser and the tissue. Generally, the goal in such procedures is to minimize the effects of thermal damage, while at the same time maximizing the speed or quality of the wound healing process. These goals can often be attained when there is a clear understanding of the effects that the laser parameters have on a given procedure. This can be a difficult task when presented with the broad range of variables that must be controlled in order to reach the desired effect. The laser wavelength is one parameter whose effects are often the least understood. Most conventional laser systems have a fixed wavelength which limits the scope of an investigation of the ablation mechanics. However, the Vanderbilt University Free Electron Laser (FEL) is a continuously tunable source of pulsed mid-IR radiation with a wavelength tuning range of $\lambda = 2 - 10 \mu\text{m}$. This makes the FEL ideal to investigate the effect of wavelength on tissue ablation procedures. In this region of the spectrum, soft tissues are strongly absorbing due to their high water content, which makes the FEL an excellent tool to investigate the mechanism of soft tissue laser ablation.

There have been several investigations studying FEL ablation of tissues, however the interpretation of the results presented and the conclusions drawn from the studies have conflicted with each other. Throughout this spectral range, tissue water is the primary chromophore, but there are several prominent protein absorption bands as well. It has been reported that by tuning the FEL to the amide II absorption band ($\lambda = 6.45 \mu\text{m}$), one can ablate soft tissues with high efficiency and minimal collateral damage [1]. These results have been attributed to the selective absorption of the laser radiation by the amide II bonds in the tissue proteins, which leads to a melting of the tissue matrix, and the ablation dynamics proceeding in a less explosive manner. Other investigations observed no significant difference in the ablation results from different protein absorption bands [2]. Further, Auerhammer et al. [2] concluded that the ablation dynamics appeared to be governed solely by the absorption coefficient of the tissue. Clearly, it has been difficult to reach firm conclusions about the effectiveness or mechanism of soft tissue ablation with the FEL. In this paper, we report the results of the measurement of both the ablation threshold and ablation rate of rat skin dermis over a broad range of wavelengths, with the goal of gaining insight into the mechanism of ablation with the FEL.

The temporal pulse structure of the FEL is unlike that of most conventional laser systems. It consists of an $\approx 5 \mu\text{s}$ *macropulse* which is the envelope of a high frequency ($\approx 3 \text{ GHz}$) train of *micropulses*, each with a duration of $\approx 1 \text{ ps}$. This structure makes the FEL a laser system

that is capable of both high peak power from the micropulses (≈ 10 MW) as well as having sufficient power for ablation from the macropulses (≈ 10 kW), and places the FEL into an interesting temporal regime. The macropulses are too long to be considered in a “blow-off” ablation model, as is typically used with Q-switched, or other short pulse systems, where it is assumed that the entire laser pulse is delivered to the tissue before material ejection begins [3–6]. We have observed in our laboratory that material ejection begins as early as 500 ns into the FEL laser pulse during gelatin ablation [7]. However, the macropulses are short enough to satisfy the thermal confinement condition for nearly all wavelengths in the mid-IR spectrum, so it should be safe to neglect effects of thermal diffusion. These observations suggest that a steady-state ablation model would be the most appropriate when considering the macroscopic effects.

We hypothesize that, to a first approximation, the ablation rate of soft biological tissues using the Vanderbilt FEL can be explained by a steady-state model, and that the interaction of FEL tissue ablation is fundamentally photothermal in nature. Further, we expect that the thermal properties of water will be sufficient in modeling the ablation of soft tissue.

III.1.1 Ablation Threshold

The ablation process is initiated when a critical energy density has been established in the tissue volume. This energy is the heat of ablation, W_{abl} (J/cm³) and is commonly defined as [8, 9]

$$W_{\text{abl}} = \rho(c_v\Delta T + L_v), \quad (\text{III.1})$$

where ρ (g/cm³) is the density, c_v (J/g/K) is the specific heat at constant volume, ΔT (K) is the temperature rise required for ablation, and L_v (J/g) is the latent heat of the tissue. The heat of ablation is simply a function of the thermal properties of the tissue, and under common conditions, is a constant.

The ablation threshold H_{th} (J/cm²) is defined as the radiant exposure required for ablation to occur and is related to the heat of ablation through the tissue absorption coefficient μ_a (cm⁻¹) [8, 10],

$$H_{\text{th}} = \frac{W_{\text{abl}}}{\mu_a}. \quad (\text{III.2})$$

This assumes a constant absorption coefficient and no heat diffusion during the laser pulse. This is considered the theoretical ablation threshold, but typically a threshold much lower is measured experimentally [8, 10].

This can be explained by the partial vaporization of the irradiated volume and the forced ejection of material that has not been supplied the heat of ablation locally. This partial

vaporization model has been developed for pulsed mid-IR ablation of water [10]. If only a fraction f of the irradiated volume is actually vaporized, then the ablation threshold is given by

$$H_{\text{th}} = \frac{1}{\mu_a} \rho (c_v \Delta T + f L_v). \quad (\text{III.3})$$

At the ablation threshold, the volume of vaporized material is infinitesimally small, hence $f \rightarrow 0$, and the expression for the ablation threshold reduces to

$$H_{\text{th}} = \frac{1}{\mu_a} \rho (c_v \Delta T). \quad (\text{III.4})$$

III.1.2 Steady-State Ablation

The basis of steady-state ablation is that a certain amount of energy (heat of ablation) must be supplied to the tissue before ablation can begin. The absorption coefficient determines the spatial distribution of the energy, and hence, the time necessary for a given ablation threshold to be reached. If the heat of ablation is delivered to the tissue during the laser pulse, material ejection begins, and all of the laser energy following this point will be used to drive an ablation front that moves into the tissue at a constant velocity, until the end of the laser pulse. In the traditional steady-state model, it is assumed that the ablated material is removed instantaneously and no longer plays a role in the ablation process. However, a more realistic scenario is that once the ablation threshold is reached, material is ejected from the tissue surface and interacts with the incident beam. If the ablation begins early enough during the incident laser pulse, the plume of ejected particles may obscure the incident beam, and attenuate the beam by absorbing the laser radiation [11, 12]. We assume that the screening of the incident laser beam follows a Beer's law distribution in the plume,

$$E(z) = E_0 \exp[-\gamma z], \quad (\text{III.5})$$

where E (W/cm^2) and γ (cm^{-1}) is the plume attenuation coefficient.

By applying Eq. (III.5) to the source term for a 1-D heat equation and neglecting heat diffusion, one can derive an expression for the ablation depth [12],

$$D_{\text{abl}} = \frac{1}{\gamma} \ln \left[\frac{\gamma}{\mu_a} \left(\frac{H_0}{H_{\text{th}}} - 1 \right) + 1 \right]. \quad (\text{III.6})$$

If multiple (n) laser pulses are used to create an ablation crater, the total crater depth

becomes

$$D_{\text{abl}} = \sum_{i=1}^n \frac{1}{\gamma} \ln \left[\frac{\gamma}{\mu_a} \left(\frac{H_n}{H_{\text{th}}} - 1 \right) + 1 \right]. \quad (\text{III.7})$$

This assumes that successive laser pulses are sufficiently far apart in time so that ejecta from the previous pulse do not screen the current pulse.

Little is known about the nature of the plume attenuation coefficient γ . If plume screening is negligible, then $\gamma = 0$, and Eq. (III.6) can be simplified by eliminating γ . This can be done by expanding the logarithmic term in Eq. (III.6) with a power series expansion, and letting $\gamma \rightarrow 0$. This reduces to the familiar steady-state ablation depth without plume attenuation [4, 13]

$$D_{\text{abl}} = \frac{1}{\mu_a} \left(\frac{H_0}{H_{\text{th}}} - 1 \right). \quad (\text{III.8})$$

Here, if $H_0 > H_{\text{th}}$, the ablation depth increases with increasing tissue absorption coefficient until a plateau is reached. At this point, an increase in absorption coefficient does not increase the ablation depth any more.

However, if plume attenuation is not negligible, then we assume the plume attenuation coefficient to be proportional to the tissue absorption coefficient ($\gamma \propto \mu_a$) since the material composition of the ejecta should be the same as the unablated tissue. Furthermore, we expect $\gamma \ll \mu_a$ since much of the plume consists of vapor with a much lower density than the native tissue. With these assumptions, we substitute $\gamma = \beta\mu_a$, where β is a proportionality constant, into Eq. (III.6) to arrive at a modified form of the ablation depth model:

$$D_{\text{abl}} = \frac{1}{\beta\mu_a} \ln \left[\beta \left(\frac{H_0}{H_{\text{th}}} - 1 \right) + 1 \right] \quad (\text{III.9})$$

In this case, as the tissue absorption coefficient rises, the increasing plume attenuation coefficient causes the ablation depth to plateau. As the absorption coefficient rises further, the plume attenuation coefficient (seen here as β) asserts a stronger effect, and begins to decrease the ablation depth as more of the laser pulse energy is attenuated.

III.2 MATERIALS AND METHODS

III.2.1 Tissue Samples

Rat dermis was harvested from sacrificed albino rats within 24 hours post-mortem. The skin was shaved and depilated using Nair and cleansed multiple times. Thin strips of skin approximately 1×5 cm were removed from the ventral side, cleaned of fascia, and stored in a refrigerator on 4% saline soaked gauze until use. The skin strips were used within 24 hours

of harvesting. Prior to irradiation, the strips were again cleaned of any remaining fascia on the dermal side, and the epidermal side was gently scraped with a scalpel blade to remove any debris and to smooth the surface.

An FTIR spectrum was taken of the rat dermis (Bruker Instruments). The spectrum was measured in attenuated total reflectance (ATR) mode, by placing the dermal side of the skin on the sample window. The measured tissue absorbance was converted to absolute absorption coefficient units (cm^{-1}) by normalizing the spectrum at two wavelengths where μ_a is known, $\lambda = 2.12$ and $2.94 \mu\text{m}$. These correspond to the Ho:YAG and Er:YAG laser lines, respectively, and at these wavelengths tissue water is the dominant absorber. Hence, the rat skin spectrum was normalized to the absorption coefficient of water at these wavelengths: $\mu_a \approx 30 \text{ cm}^{-1}$ at $\lambda = 2.12 \mu\text{m}$ and $\mu_a \approx 13,300 \text{ cm}^{-1}$ at $\lambda = 2.94 \mu\text{m}$ [14].

Based on the FTIR spectrum, laser wavelengths were chosen for irradiation that correspond to the peaks, valleys, and rising and falling edges of the absorption spectrum in order to investigate the broadest range of absorption properties. The wavelengths investigated were $\lambda = 2.65, 2.8, 2.94, 3.0, 3.15, 3.3, 3.6, 4.0, 4.4, 5.5, 5.7, 5.9, 6.1, 6.45,$ and $6.7 \mu\text{m}$.

III.2.2 Laser Source and Delivery

The FEL beam is delivered to the laboratory via a vacuum beam transport system which is terminated by a BaF_2 window. The FEL beam is delivered to the tissue surface by focusing it with a CaF_2 lens ($f = 200 \text{ mm}$). The spot diameter on the tissue surface is set to $500 \pm 10 \mu\text{m}$ by adjusting the lens position. The FEL spatial beam profile is Gaussian (TEM_{00}), and the laser spot diameter is confirmed using an automated scanning knife-edge measurement [15]. The FEL beam is linearly polarized and the pulse energy was adjusted by rotating a double Brewster plate polarizer mounted within the vacuum chamber. A schematic of the experimental setup is seen in Fig. III.1.

III.2.3 Ablation Threshold Measurements

For our experiments, the ablation threshold was defined as the radiant exposure necessary to produce visible material ejection from the surface of the tissue. To determine the ablation threshold, a *probit* method was used [16]. This is a statistical technique, which determines the probability of ablation as a function of the incident energy. In the experiment, the incident pulse energy is varied about the anticipated threshold, and for each pulse, an observer blinded to the pulse energy gives a score of 1 if material ejection is observed, or 0 if it is not. The observation of ejecta was aided with forward white light illumination of the irradiated surface

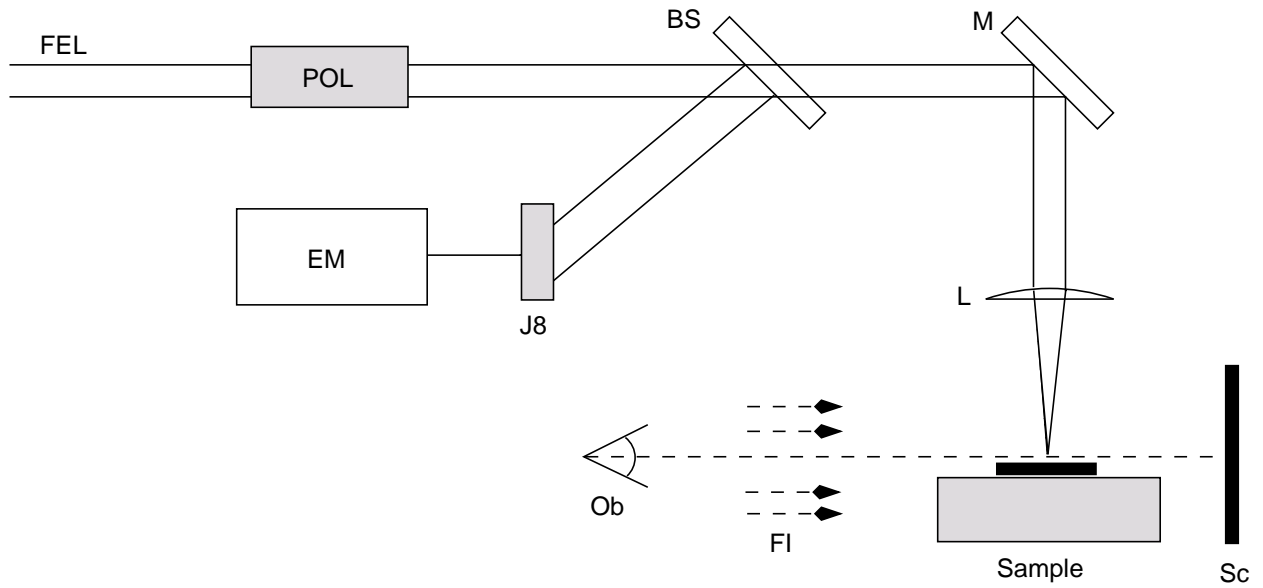


Figure III.1: Experimental setup for the measurement of ablation threshold. The FEL beam is delivered through a double Brewster plate polarizer (POL) to attenuate the beam. A portion of the beam is picked-off with a CaF₂ window (BS) and the pulse energy is measured with a pyroelectric detector (J8) and recorded with an energy meter (EM). The FEL beam is delivered to the tissue sample with a mirror (M) and focused onto it with an $f = 200$ mm lens (L). An observer (Ob) monitors whether ablation has occurred with the aid of forward white-light illumination (FI) and a black screen (Sc).

and a black screen behind to increase the contrast. Ten individual shots were delivered to a single location for the measurement, after which time a fresh location was used for another ten shots, up to a total of 100 pulses. Post-experimentally, the data were analyzed to find the energy dosage that produced a 50% probability (ED_{50}) of ablation.

The pulse energy for each pulse was monitored by picking off a portion of the incident beam ($\approx 10\%$) with a CaF_2 window and detecting the pulse energy with a pyroelectric detector (J8, Molelectron, Portland, OR). Prior to the experiment, the detector was calibrated against a second pyroelectric detector (J50, Molelectron, Portland, OR) with a dual channel energy meter (EPM2000, Molelectron, Portland, OR). Post-experimentally, the calibration coefficients were used to calculate the pulse energy that is actually delivered to the tissue, and the measured spot size (Gaussian ω_L parameter) was used to calculate the laser pulse radiant exposure.

III.2.4 Ablation Depth Measurements

The rat dermis strips were placed on a sample stage and irradiated with the FEL beam on the epidermal surface. For each wavelength, 10 craters were produced, and each crater was made by delivering 10 pulses at a fixed radiant exposure of 5 J/cm^2 per pulse, for a total delivered radiant exposure of 50 J/cm^2 . A low repetition rate (5 Hz) was used to minimize inter-pulse ablation plume screening. The crater depth was measured by imaging the ablation crater with an optical coherence tomography (OCT) system constructed in our laboratory with an axial resolution of $\approx 13 \mu\text{m}$ [17].

III.3 RESULTS

III.3.1 Rat Dermis FTIR

An FTIR spectrum of the rat dermis is shown in Fig. III.2. The spectrum shows the strong absorption peak at $\lambda = 2.94 \mu\text{m}$ due to the fundamental vibrational stretching mode of water. A second prominent peak is seen at $\lambda = 6.1 \mu\text{m}$ from the vibrational bending mode of water [18]. At $\lambda = 6.1 \mu\text{m}$ the amide I bonds, which primarily exist in the protein matrix of tissue, absorb as well and contribute to the overall absorption peak seen at this wavelength. At $\lambda = 6.45 \mu\text{m}$ a shoulder is observed which is due to the amide-II bonds in tissue proteins [19].

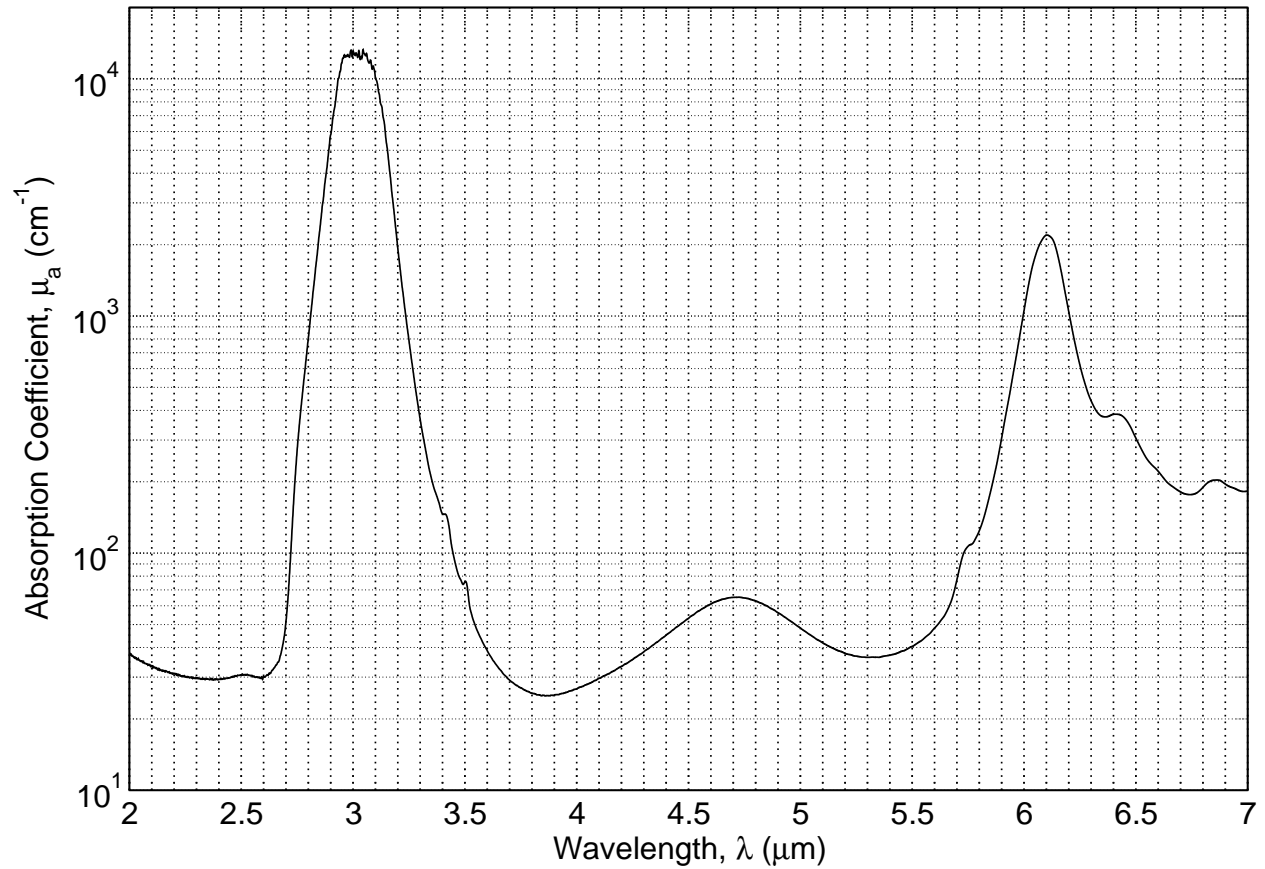


Figure III.2: Normalized rat dermis FTIR absorption spectrum. The spectrum was measured in ATR mode with the dermal surface of the rat skin placed on the sample window. The measured absorbance was converted to absorption coefficient units by normalizing the spectrum at $\lambda = 2.12$ and $2.94 \mu\text{m}$ to known values of the absorption coefficient of water.

III.3.2 Ablation Threshold Measurements

The probit measurement data (Fig. III.3) for the ablation of rat dermis are shown for $\lambda = 2.94 \mu\text{m}$. It is representative of the experimental threshold data for all wavelengths measured. The measured data points are plotted with the calculated probability of ablation and the upper and lower fiducial limits (95% confidence intervals).

The measured surface ablation threshold was plotted as a function of wavelength (Fig. III.4). Along with the measured threshold data, an ablation threshold was calculated from the FTIR absorption data using the partial vaporization model in Eq. (III.3). The threshold was calculated for the two extreme scenarios: (1) the volume fraction that needs to be vaporized for ablation to occur is infinitesimally small ($f = 0$) and (2) the entire irradiated volume (according to a Beer's law penetration depth of light) must be vaporized for ablation to occur ($f = 1$). From the plot, we can see that the measured surface ablation threshold generally follows the shape of the calculated threshold, based on the thermal model.

The measured ablation threshold was also plotted as a function of the absorption coefficient at each wavelength (Fig. III.5). The measured data points are also fit to the theoretical ablation threshold in Eq. (III.2) using a least-squares algorithm and setting W_{abl} as a free parameter. This calculated a heat of ablation of $W_{\text{abl}} = 52 \text{ J/cm}^3$. This inverse relationship shows that as the tissue absorption coefficient increases to very large values, the theoretical ablation threshold approaches zero. From the plot, we can see that the measured data follow this trend.

III.3.3 Ablation Depth Measurements

The measured crater depth was plotted as a function of the laser wavelength (Fig. III.6) along with the FTIR absorption spectrum for reference. The ablation depth tends to follow the shape of the absorption spectrum, as one would expect. However, one can see the effect of plume screening at the wavelengths where the absorption is strongest, e.g.—near $\lambda = 3.0 \mu\text{m}$ and at $\lambda = 6.1 \mu\text{m}$. Here, we can see that the ablation depth is decreased, relative to the absorption coefficient.

The crater depth data are also plotted as a function of the tissue absorption coefficient for each wavelength (Fig. III.7). The measured data were fit to the steady-state ablation depth model (Eq. III.6) in two forms. First, we applied the model where the effect of plume screening is negligible, i.e.— $\gamma = 0$ (Eq. III.8), by allowing W_{abl} to be a free parameter. This is the solid line in Fig. III.7, and the fit calculated a heat of ablation, $W_{\text{abl}} = 1507 \text{ J/cm}^3$. Second, we applied the model which assumes that plume attenuation coefficient is propor-

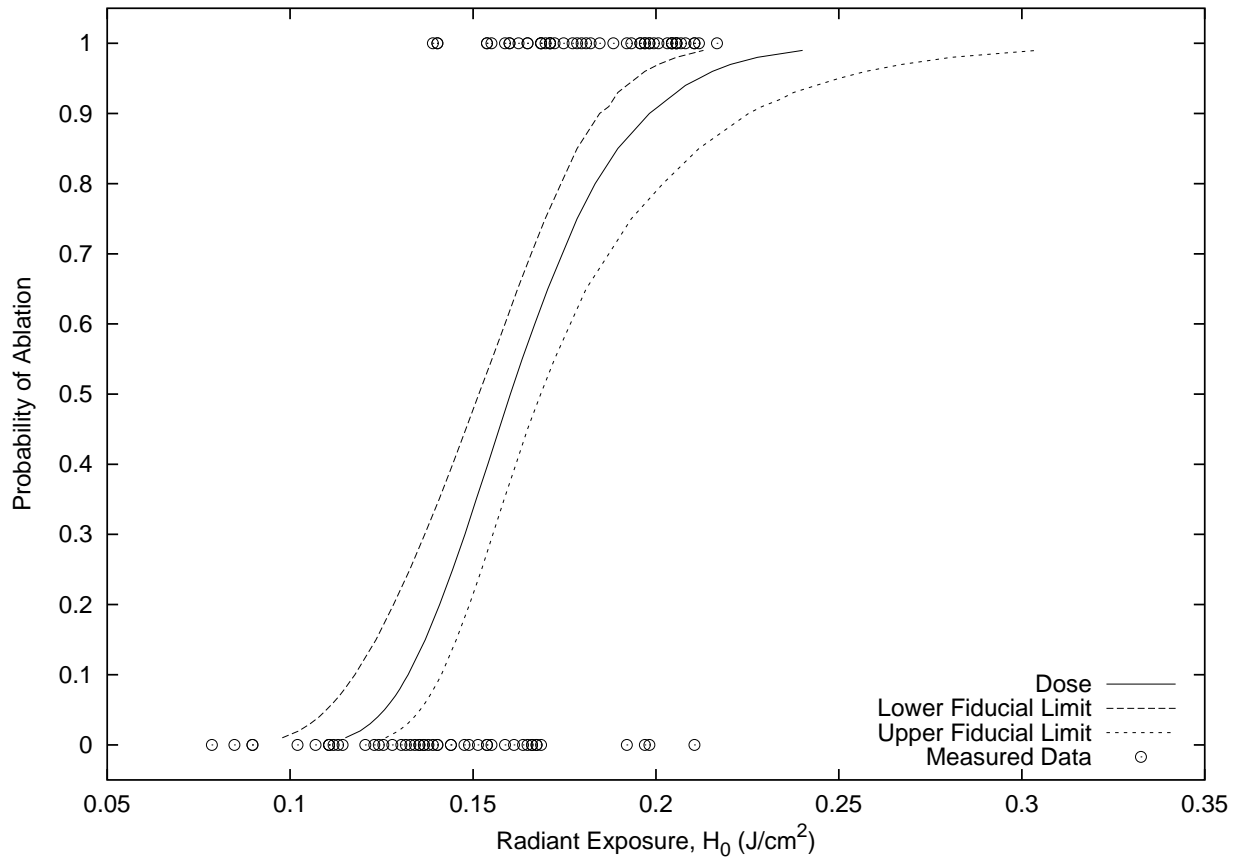


Figure III.3: Probit measurement of rat dermis surface ablation threshold. The measured ablation data (points) are used to calculate the probability of ablation as a function of the incident radiant exposure. The upper a lower fiducial limits were calculated using 95% confidence intervals and represent the measurement error for a given probability. The ablation threshold is taken as the radiant exposure at which there is a 50% probability of ablation (ED50).

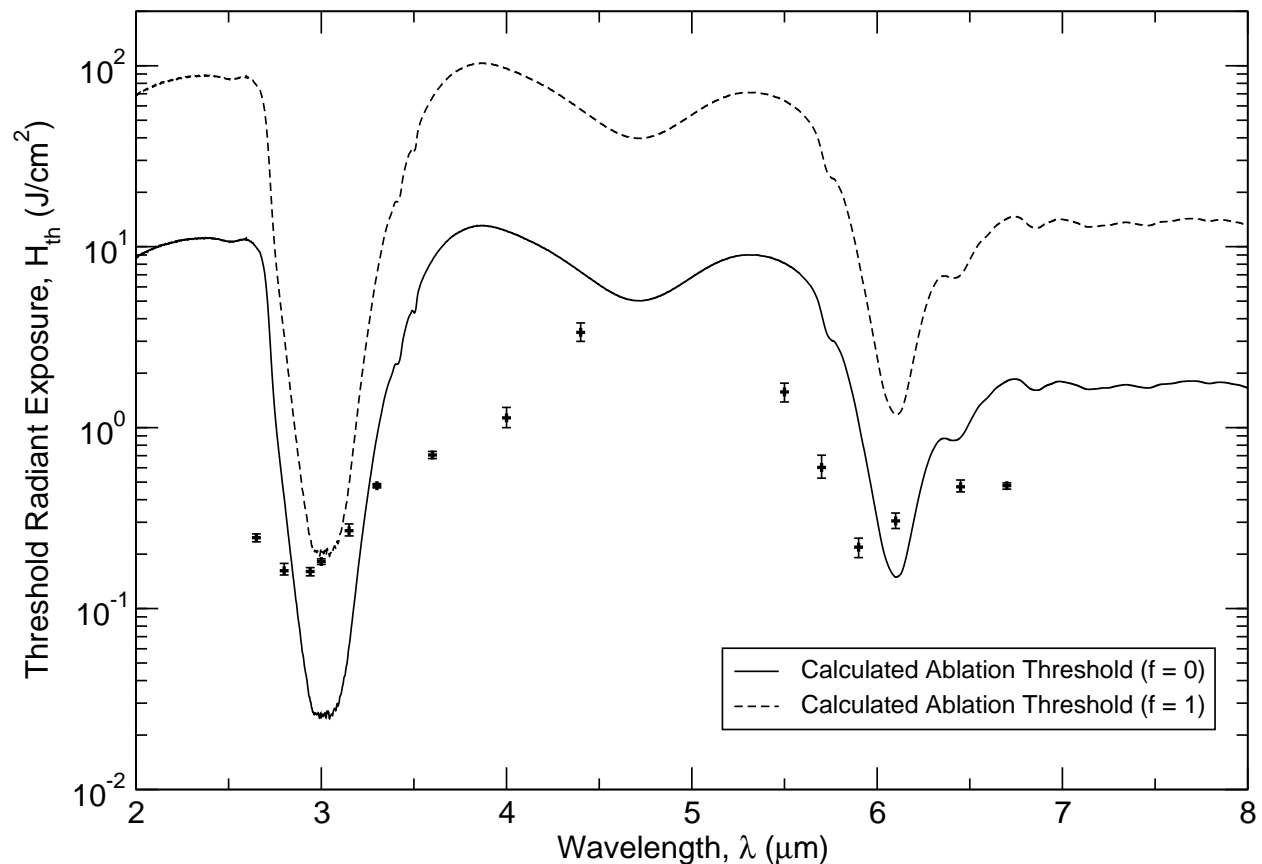


Figure III.4: Rat dermis ablation threshold as a function of wavelength. The measured threshold is plotted with ablation threshold calculated from the partial vaporization model (Eq. III.3). The theoretical threshold is calculated for two situations: (1) assuming that no latent heat is necessary for ablation ($f = 0$), and (2) the maximum amount of the latent heat of vaporization of water is necessary for ablation ($f = 1$). The error bars are the upper and lower fiducial limits of the threshold measurement which were calculated on a 95% confidence interval.

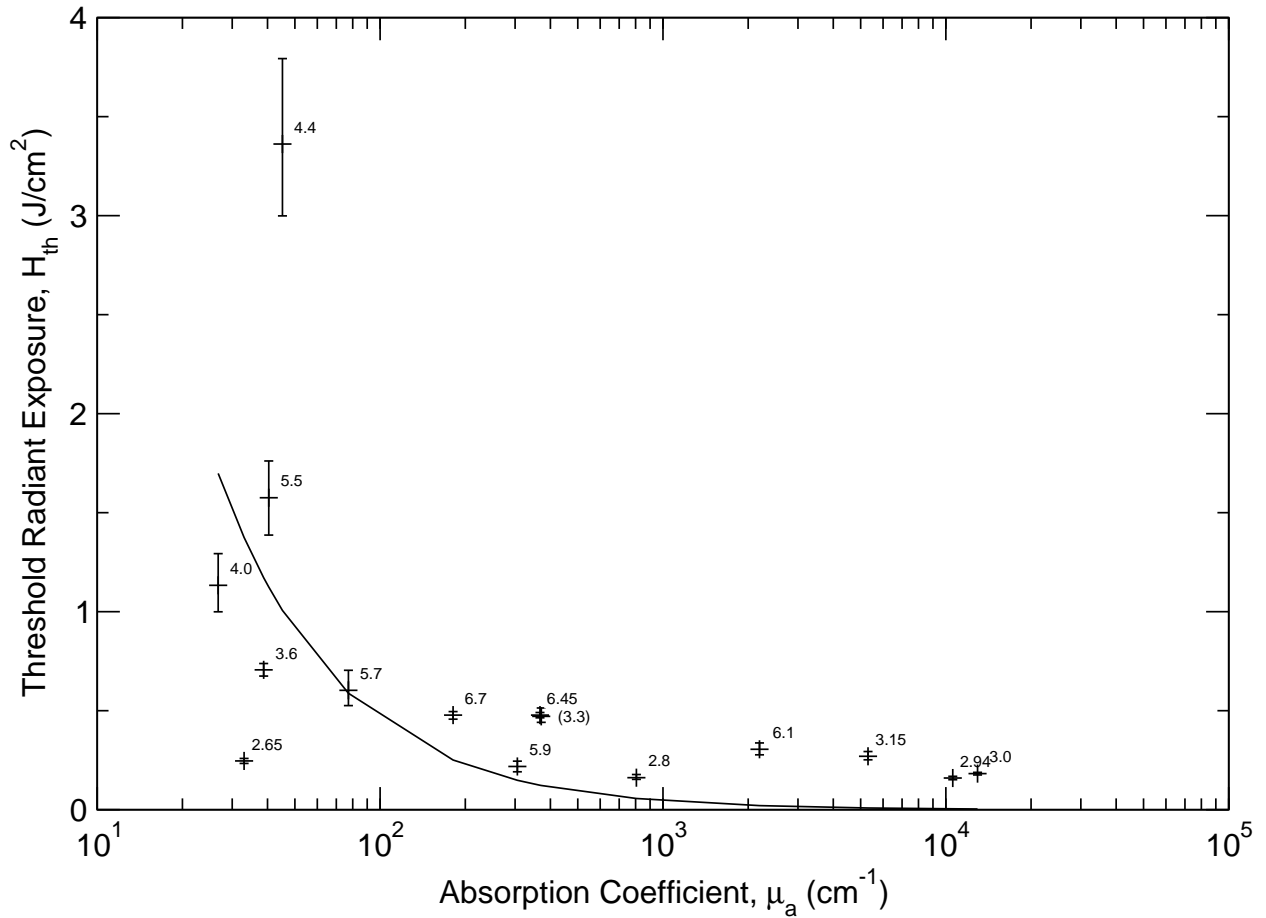


Figure III.5: Rat dermis ablation threshold as a function of tissue absorption coefficient. The measured data are fit to the theoretical ablation threshold in Eq. (III.2). The fit calculated a heat of ablation of $W_{\text{abl}} = 52 \text{ J}/\text{cm}^3$. The error bars are the upper and lower fiducial limits of the threshold measurement which were calculated on a 95% confidence interval and the fit was forced through zero. *Note:* The data point at $\lambda = 6.45 \mu\text{m}$ lies on top of the point from $\lambda = 3.3 \mu\text{m}$.

tional to the tissue absorption coefficient (Eq. III.9), by allowing both W_{abl} and β to be free parameters. This is the dashed line in Fig. III.7, and the fitting algorithm reported a heat of ablation, $W_{\text{abl}} = 1358 \text{ J/cm}^3$, and a plume attenuation coefficient, $\gamma = 0.0045\mu_{\text{a}}$.

III.4 DISCUSSION

III.4.1 FTIR Spectrum

The absorbance data from the FTIR absorption spectrum were converted to units of absorption coefficient so that the ablation threshold and ablation rate models could be applied to the experimental data. The spectrum was normalized to known absorption coefficients of water at two wavelengths, $\lambda = 2.10$ and $2.94 \mu\text{m}$, which correspond to the Ho:YAG and Er:YAG laser lines, respectively. At these wavelengths, water is the dominant chromophore in most soft tissues, including skin, so the absorbance calibration should be accurate for those wavelengths where water is the dominant chromophore. This is generally the case for most of the mid-IR spectrum of soft tissues, with the exception of the protein absorption bands, most notably, the amide bands at $\lambda = 6.1$ and $6.45 \mu\text{m}$. Here, there is the possibility of a distortion in the absorption coefficient of dermis, as the absorbance calibration using water does not account for the protein absorption. This could affect the accuracy of these data points in Figs. III.5 and III.7 since the points are plotted as a function of the calibrated absorption coefficient.

III.4.2 Ablation Threshold Measurements

There is a significant discrepancy between the measured ablation threshold data and the threshold calculated according to the partial vaporization model (Fig. III.4). According to the model, we would expect all of the measured threshold points to fall somewhere in between the two curves, designated by $f = 0$ and $f = 1$ in Eq. (III.3). In principle, the actual ablation threshold is in an infinitely small volume of the irradiated tissue ($f \rightarrow 0$). An observation threshold may require that a minimum volume must be vaporized for an ablation plume to be visible, so we would expect to find a fraction of the irradiated volume to be slightly larger than 0 ($f > 0$). However, we see that most of the points lie below the $f = 0$ curve. This suggests that the heat of ablation is well below what we would expect from the partial vaporization model, i.e.— $W_{\text{abl}} < \rho c_v \Delta T$. This is confirmed in Fig. III.5, where the data points were fit to the ablation threshold relation (Eq. III.2), which calculated a heat of ablation, $W_{\text{abl}} = 52 \text{ J/cm}^3$. This is indeed well below the theoretical minimum

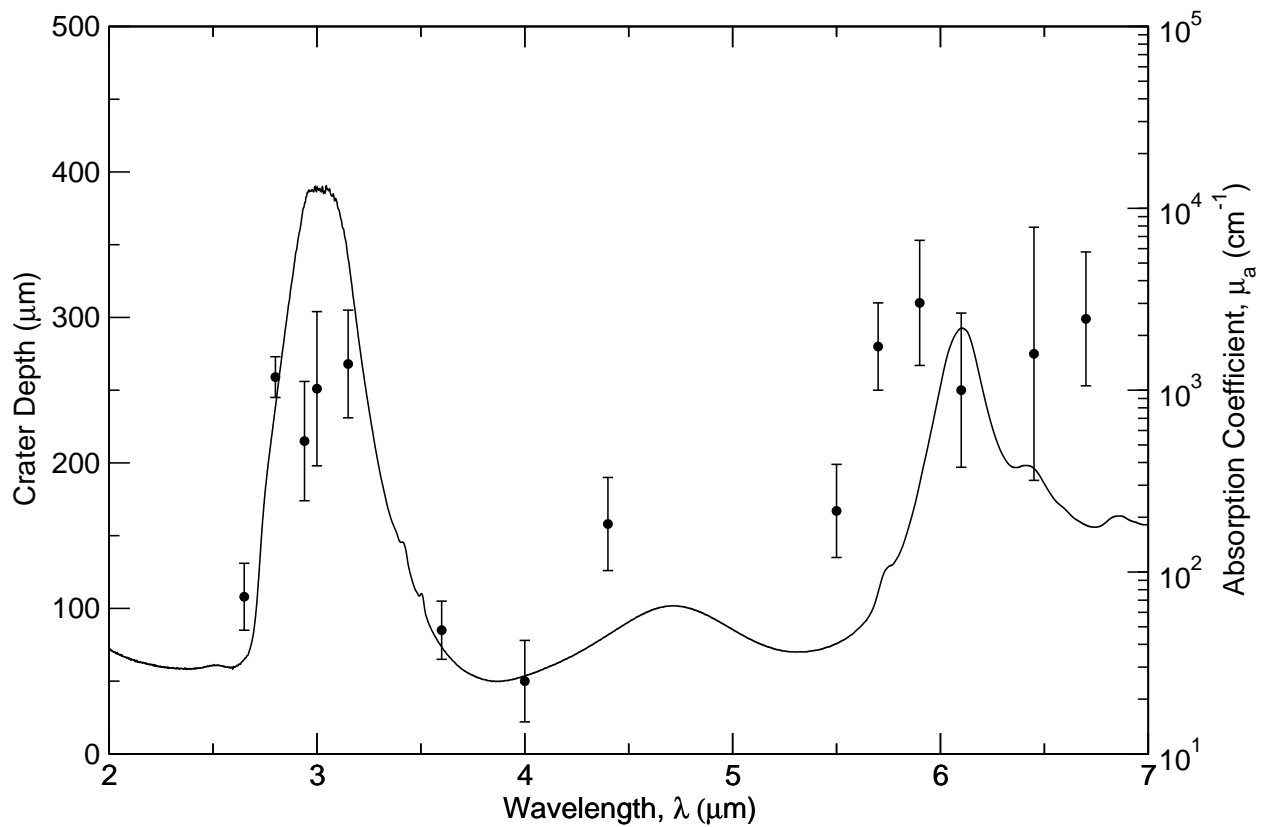


Figure III.6: Rat skin ablation depth as a function of wavelength. The measured ablation depth is plotted with the FTIR absorption spectrum. One can see the effect of plume screening in the decreased ablation depth at wavelengths with large absorption coefficients, e.g.—near $\lambda = 3.0 \mu\text{m}$ and at $\lambda = 6.1 \mu\text{m}$.

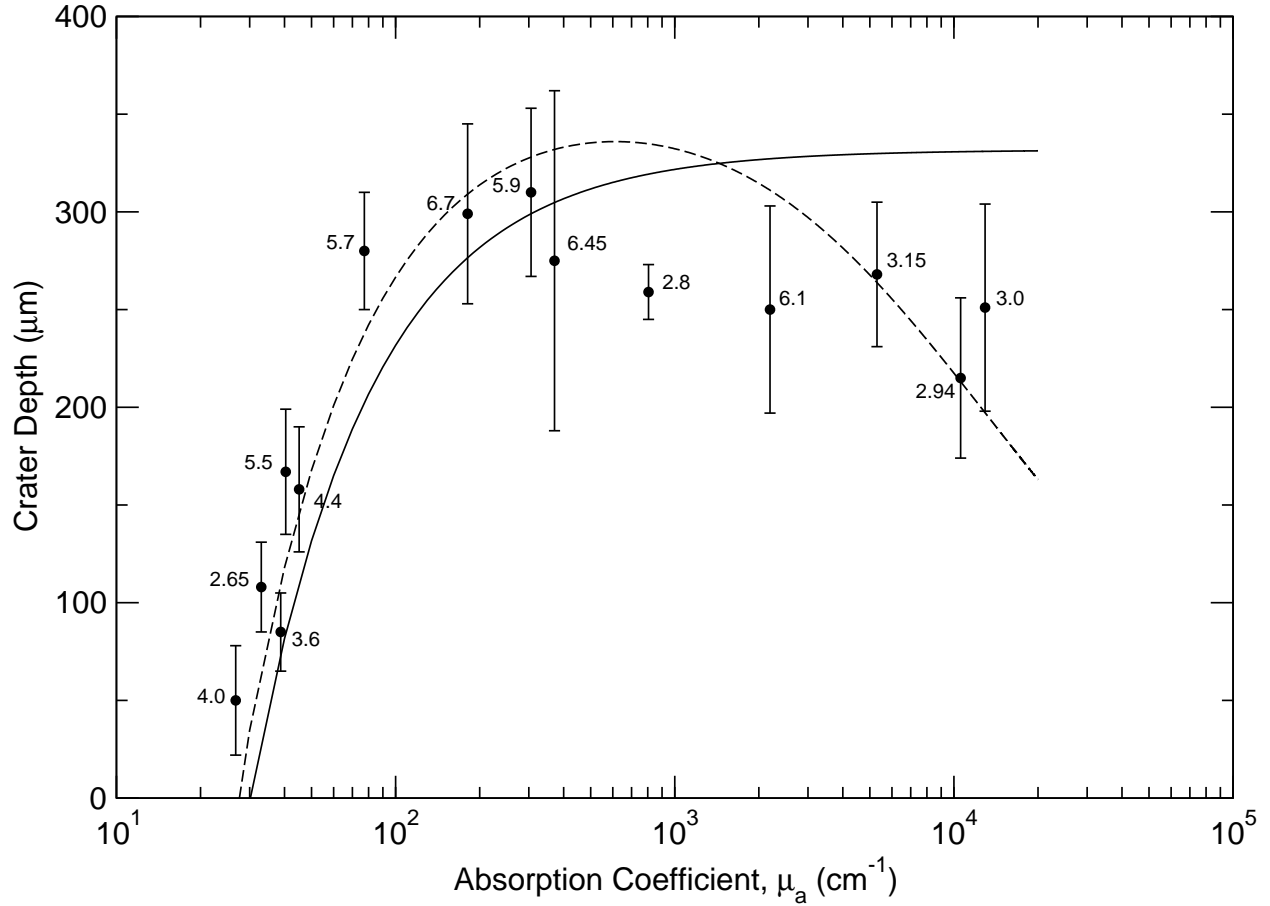


Figure III.7: Rat skin ablation depth as a function of the tissue absorption coefficient. The data are fit to the steady-state ablation depth model in Eq. (III.6). The solid line is the model fit when the plume attenuation coefficient, $\gamma = 0$ (Eq. III.8); the fitting algorithm calculated a heat of ablation, $W_{\text{abl}} = 1507 \text{ J/cm}^3$. The dashed line is the model fit when $\gamma = \beta\mu_a$ (Eq. III.9), which calculated a heat of ablation, $W_{\text{abl}} = 1358 \text{ J/cm}^3$, and a plume attenuation coefficient, $\gamma = 0.0045\mu_a$.

threshold one would expect according to the thermal properties of water. Assuming that $\rho = 1.0 \text{ g/cm}^3$, $c_v = 4.18 \text{ J/g/K}$ and $\Delta T = 78 \text{ K}$, this minimum would be $W_{\text{abl}} = 326 \text{ J/cm}^3$.

One explanation for the ablation threshold results could be related to the FEL beam properties. The FEL beam has a Gaussian spatial profile. In the experiments, the radiant exposure was calculated by dividing the laser pulse energy by the spot area, where it was assumed that the beam energy was uniform, i.e.— the spot area was calculated according to $A = \pi\omega_L^2$, where ω_L is the Gaussian beam waist. This is the average radiant exposure H_{avg} and does not give an accurate value for the true radiant exposure, since it is a function of the beam radius. We can calculate the peak radiant exposure, $H(r = 0)$ by integrating the beam energy E over the laser spot area, which gives

$$H(r = 0) = 2 \frac{E}{\pi\omega_L^2} = 2H_{\text{avg}}. \quad (\text{III.10})$$

Theoretically, the threshold for ablation involves the vaporization of an infinitely small volume of tissue. In such a small region, we should certainly consider the peak radiant exposure $H(r = 0)$ to be the actual incident exposure. If this is the case, then the actual ablation thresholds should be a factor of 2 lower than the measured thresholds, and the heat of ablation that is calculated from the model fit in Eq. (III.2), would be a factor of 2 larger, closer to $W_{\text{abl}} \approx 100 \text{ J/cm}^3$. This is still smaller than one would expect from the partial vaporization model, but it might explain part of the difference.

Another potential explanation for the low calculated heat of ablation may have to do with the FEL pulse structure. In a surface ablation geometry, we are depositing the laser energy just below the tissue surface, which behaves as a free boundary. The laser energy deposition serves to heat the tissue, but it can generate large amplitude stress waves as well [20–22]. If the laser pulse duration is shorter than the time it takes an acoustic wave to travel out of the irradiated volume. This is known as the inertial confinement time τ , and the condition for it is: $\tau = \delta/\sigma$, where δ is the optical penetration depth, and σ is the speed of sound in the tissue. The minimum confinement time occurs at the most strongly absorbing wavelengths. Assuming $\delta \approx 1 \mu\text{m}$, and $\sigma = 1500 \text{ m/s}$, $\tau \approx 0.66 \text{ ns}$. The FEL micropulse duration, $\tau_L \approx 1 \text{ ps}$ is much shorter than the confinement time. Indeed, even the micropulse separation of 350 ps is short compared to the inertial confinement time. The importance of this is that when inertially confined pulses are delivered to the tissue surface, large amplitude tensile stress waves are created. These tensile stress waves serve to reduce the pressure locally which can impact the temperature as well. According to the ideal gas law, water can boil at room temperature if a pressure of -9 bar is created at constant volume. In a theoretical study, we have calculated that tensile stresses on the order of -10 bar are generated in water by the

FEL under typical irradiation conditions [23]. This suggests the micropulse structure of the FEL may impact the ablation process by reducing the temperature rise that is necessary to deliver the heat of ablation.

III.4.3 Plume Screening

The effects of plume screening can be seen in Figs. III.6 and III.7. In Fig. III.6, we can see a decrease in the measured ablation depth at wavelengths with large absorption coefficients, e.g.—near $\lambda = 3.0 \mu\text{m}$ and at $\lambda = 6.1 \mu\text{m}$. This is more clearly seen in Fig. III.7, where there is a clear decrease in the ablation depth with increasing absorption coefficient. The steady-state ablation model fits show several things. First, both the model without plume screening ($\gamma = 0$), and with plume screening ($\gamma = \beta\mu_a$), fit the data well. As the absorption coefficient increases, they begin to diverge as the effect of plume screening becomes stronger. The data shows that the form of the plume attenuation coefficient chosen appears to be a good one, where it is proportional to the tissue absorption coefficient, and much smaller. Indeed, the model fit calculated a value of $\gamma = 0.0045\mu_a$. This implies that the plume is composed of tissue “droplets,” however, it is difficult to generalize the plume attenuation coefficient over such a broad range of wavelengths with potentially different absorption characteristics.

III.4.4 Heat of Ablation

The steady-state ablation model fit in Fig. III.7, also reveals another important parameter in the experiments, the heat of ablation. Using the ablation depth model with plume screening ($\gamma = \beta\mu_a$), the model predicts a heat of ablation of $W_{\text{abl}} = 1358 \text{ J/cm}^3$. This value is reasonable, as it falls in the range of what one would expect according the partial vaporization model. Using the thermal properties of water, we can calculate a fraction of latent heat that is necessary for ablation. Substituting $\rho = 1.0 \text{ g/cm}^3$, $c_v = 4.18 \text{ J/g/K}$, $\Delta T = 78 \text{ K}$, and $L_v = 2260 \text{ J/g}$ into Eq. (III.3), we find a fraction of latent heat of $f = 46\%$. This means that only 46% of the irradiated volume must be vaporized in order for material ejection to occur. This is consistent with experiments performed in our laboratory of high speed pump-probe imaging of the plume formed from the ablation of gelatin, where we have observed that the ejecta are composed of large chunks of material, along with a fine mist of water droplets. If the entire volume were vaporized during the irradiation, one would expect that the plume would be composed of a gaseous vapor instead.

The ablation depth data in Fig. III.7 were also fit to the steady-state ablation model without plume screening ($\gamma = 0$). This fit predicted a heat of ablation of $W_{\text{abl}} = 1507 \text{ J/cm}^3$,

which gives a fraction of latent heat of $f = 52\%$. This is important for two reasons. First, it give us confidence that the ablation process does indeed follow the steady-state model. While the two equations that were used to fit the ablation depth data have different characteristics at high absorptions, they only differ in their choice of the plume attenuation coefficient, γ . Therefore, we would expect both models to fit the data within a certain error, since they are both based on the same fundamental assumptions. Second, this also supports our hypothesis that the underlying ablation mechanism with the FEL is primarily photothermal in nature which obeys much of the thermodynamics of water

III.4.5 Dynamic Absorption

It has long been known that the absorption coefficient of water is strongly influenced by temperature [24–27]. This temperature dependence has been attributed to the deposited energy density in the absorbing material [28, 29]. One result of this strong temperature dependence is that the water absorption band at $\lambda = 3 \mu\text{m}$ is shifted to shorter wavelengths during rapid energy deposition, i.e.—temperature rise. This causes the absorption coefficient of water to increase at wavelengths on the blue side of the peak (shorter wavelengths), and to decrease on the red side (longer wavelengths).

This effect can clearly be seen in ablation depth data. In Fig. III.7, several of the wavelengths near the $3 \mu\text{m}$ water absorption peak have had their absorption coefficients increased or decreased as a result of the dynamic absorption. For example, the wavelength $\lambda = 2.8 \mu\text{m}$, lies on the steep rising edge of the absorption band. As the absorption peak is blue-shifted from the dynamic absorption, this would increase the effective absorption coefficient by possibly as much as one order of magnitude (see Fig. III.2). This would shift the data point in Fig. III.7 to right, placing it nearly on the ablation depth model curve for $\gamma = \beta\mu_a$ (dashed line). Another example is the data point at $\lambda = 3.0 \mu\text{m}$. Since this is at the peak of the water absorption band, a blue shift would place this wavelength on the falling edge of the band, decreasing its effective absorption coefficient. As a result, the data point would be shifted to the left in the plot, again placing it closer to the model fit.

The effect of dynamic absorption can also be seen in the ablation threshold data. In Fig. III.5, this is most evident at $\lambda = 2.65 \mu\text{m}$ which lies at the base of the water absorption band. A blue shift in the peak would cause this wavelength to have a much higher effective absorption coefficient, which moves the data point to the right in Fig. III.5, closer to the model fit.

When considering the effect of dynamic absorption, the experiments lend further support to our hypothesis that soft tissue ablation with the FEL is a water absorption dominated

process.

III.4.6 Protein Absorption

Given the size of the error bars of the data points at $\lambda = 6.1$ and $6.45 \mu\text{m}$ in Fig. III.7, it is difficult to draw conclusions about the effect of protein absorption in these experiments. At these wavelengths, protein in the tissue matrix absorbs a significant amount of the incident radiation [19]. By calibrating the entire FTIR spectrum of skin to water, we may underestimate the absorption coefficient at these wavelengths. If this is case, $\lambda = 6.1 \mu\text{m}$ would be shifted to the right in Fig. III.7, closer to the model fit. The same should be true for $\lambda = 6.45 \mu\text{m}$, however, it is difficult to make this argument considering the measurement error at these wavelengths. More accurate information about the absorption coefficient of collagen and tissue protein is required before this discrepancy can be resolved. However, we suspect that with this information, these wavelengths should follow a steady-state ablation model, governed by a basic photothermal interaction.

III.5 CONCLUSIONS

Several conclusions can be drawn from the data presented in this chapter. First, FEL ablation of soft tissue is largely explained by a steady-state ablation model. It was found that the ablation depth model incorporating the effect of plume screening fit our experimental data over a very wide range of tissue absorption, nearly three orders of magnitude. Second, the pulse duration and structure of the FEL appears to be very well suited for soft tissue ablation. Over almost the entire spectral range of the FEL, the macropulse is thermally confined, minimizing effects of thermal damage, while still possessing enough pulse energy to ablate efficiently. This efficiency may be aided by the micropulse structure, where after the heat of ablation has been supplied to the tissue, each successive micropulse removes a very fine layer of tissue according to the steady-state model, effectively drilling very deep crater. And finally, with the exception of two wavelengths in this study where protein absorption is significant, FEL ablation of soft tissue is a water-absorption dominated process. This is supported by the partial vaporization model which tells us that a realistic fraction of the irradiated volume must be vaporized for ablation to occur and by the dynamic absorption of water, which can explain many of the data points that do lie directly on the steady-state ablation depth curve.

ACKNOWLEDGEMENTS

The authors would thank Dr. Kin Chan for fruitful discussions. This research was supported in part by a grant from the Department of Defense through the MFEL Program under Award No. F49620-01-1-0429 and a Dissertation Enhancement Grant from the Graduate School at Vanderbilt University.

REFERENCES

- [1] Edwards G, Logan R, Copeland M, Reinisch L, Davidson J, Johnson B, Maciunas R, Mendenhall M, Ossoff R, Tribble J, Werkhaven J, O'Day D, "Tissue ablation by a free-electron laser tuned to the amide II band," *Nature*, 371:416–419, 1994.
- [2] Auerhammer JM, Walker R, van der Meer AFG, Jean B, "Dynamic behavior of photoablation products of corneal tissue in the mid-IR: A study with FELIX," *Applied Physics B: Lasers and Optics*, 68:111–119, 1999.
- [3] Esenaliev RO, Oraevsky AA, Lethokov VS, "Laser ablation of atherosclerotic blood vessel tissue under various irradiation conditions," *IEEE Transactions in Biomedical Engineering*, 36:1188–1194, 1989.
- [4] Hibst R, Keller U, "Experimental studies of the application of the Er:YAG laser on dental hard substances: I. Measurement of the ablation rate," *Lasers in Surgery and Medicine*, 9:338–344, 1989.
- [5] Muller G, Dorschel K, Kar H, "Biophysics of the photoablation process," *Lasers in Medical Science*, 6:251–254, 1991.
- [6] Walsh JT, Deutsch TF, "Pulsed CO₂ laser ablation of tissue: Effect of mechanical properties," *IEEE Transactions in Biomedical Engineering*, 36:1195–1201, 1989.
- [7] Uhlhorn SR, Harrison S, Pratisto HS, Jansen ED, "Tissue ablation with the free electron laser: Contributions of wavelength and pulse structure," in *Laser Tissue Interaction X*, Jacques SL, ed., vol. 3601, pp. 256–261, SPIE, Bellingham, WA, USA, 1999.
- [8] Welch AJ, van Gemert MJC, eds., *Optical-Thermal Response of Laser-Irradiated Tissue*, chap. 21, pp. 709–763, Plenum Press, New York, 1995.

- [9] Olmes A, Franke HG, Bänsh E, Lubatschowski H, Raible M, Dziuk G, Ertmer W, “Modeling of infrared soft-tissue photoablation process,” *Applied Physics B*, 65:659–666, 1997.
- [10] Jansen ED, van Leeuwen TG, Motamedi M, Borst C, Welch AJ, “Partial vaporization model for pulsed mid-infrared laser ablation of water,” *Journal of Applied Physics*, 78(1):564–571, 1995.
- [11] Izatt JA, Sankey ND, Partovi F, Fitzmaurice M, Rava RP, Itzkan I, Feld MS, “Ablation of calcified biological tissue using pulsed hydrogen fluoride laser radiation,” *IEEE Journal of Quantum Electronics*, 26(12):2261–2270, 1990.
- [12] Chan KF, Welch AJ, “Free electron laser ablation of urinary calculi: A theoretical review,” *Physics in Medicine and Biology*, submitted.
- [13] Partovi F, Strikwerda S, Izatt JA, Kittrell C, Kramer JR, Feld MS, “A model for thermal ablation of biological tissue using laser radiation,” *Lasers in Surgery and Medicine*, 7:141–154, 1987.
- [14] Irvine WM, Pollack JB, “Infrared optical properties of water and ice spheres,” *Icarus*, 8:324–360, 1968.
- [15] Khosrofian JM, Garetz BA, “Measurement of a gaussian laser-beam diameter through the direct inversion of knife-edge data,” *Applied Optics*, 22(21):3406–3410, 1983.
- [16] Cain CP, Noojin GD, Manning L, “A comparison of various probit methods for analyzing yes/no data on a log scale,” Tech. Rep. AL/OE-TR-1996-0102, USAF Armstrong Laboratory Technical Report, 1996.
- [17] Bouma BE, Tearney GJ, eds., *Handbook of Optical Coherence Tomography*, Marcel Dekker, Inc., 2002.
- [18] Walsh JT, Cummings JP, “Effect of the dynamic optical properties of water on mid-infrared laser ablation,” *Laser in Surgery and Medicine*, 15:295–305, 1994.
- [19] Yannas IV, “Collagen and gelatin in the solid state,” *Journal of Macromolecular Science—Reviews in Macromolecular Chemistry*, C7(1):49–104, 1972.
- [20] Dingus RS, Scammon J, “Grüneisen-stress induced ablation of biological tissue,” in *Laser-Tissue Interaction II*, vol. 1427, SPIE, 1991.

- [21] Esenaliev RO, Oraevsky AA, Letokhov VS, Karabutov AA, Malinsky TV, “Studies of acoustical and shock waves in the pulsed laser ablation of biotissue,” *Lasers in Surgery and Medicine*, 13:470–484, 1993.
- [22] Paltauf G, Reichel E, Schmidt-Kloiber H, “Study of different ablation models by use of high-speed-sampling photography,” in *Laser-Tissue Interaction III*, vol. 1646, pp. 343–352, SPIE, 1992.
- [23] Uhlhorn SR, London RA, Makarewicz AJ, Jansen ED, “Hydrodynamic modeling of tissue ablation with a free-electron laser,” in *Laser-Tissue Interaction XI*, vol. 3914A, SPIE, 2000.
- [24] Collins JR, “Changes in the infra-red absorption spectrum of water with temperature,” *Physical Review*, pp. 771–779, 1925.
- [25] Hale GM, Querry MR, Rusk AN, Williams D, “Influence of temperature on the spectrum of water,” *Journal of the Optical Society of America*, 62(9):1103–1108, 1972.
- [26] Falk M, Ford TA, “Infrared spectrum and structure of liquid water,” *Canadian Journal of Chemistry*, 44:1699–1707, 1966.
- [27] Pinkley LW, Sethna PP, Williams D, “Optical constants of water in the infrared: Influence of temperature,” *Journal of the Optical Society of America*, 67(4):494–499, 1977.
- [28] Vodopyanov KL, “Saturation studies of H₂O and HDO near 3400 cm⁻¹ using intense picosecond laser pulses,” *Journal of Chemical Physics*, 94(8):5389–5393, 1991.
- [29] Shori RK, Walston AA, Stafsudd OM, Fried D, Walsh JT, “Quantification and modeling of the dynamic changes in the absorption coefficient of water at $\lambda = 2.94\mu\text{m}$,” *IEEE Journal of Selected Topics in Quantum Electronics*, 7(6):959–970, 2001.

CHAPTER IV

THE EFFECT OF PROTEIN ABSORPTION AND MECHANICAL STRENGTH
IN THE ABLATION OF SOFT TISSUE WITH A FREE ELECTRON LASER

Stephen R. Uhlhorn and E. Duco Jansen

Vanderbilt University
Department of Biomedical Engineering
Nashville, TN

Prepared for submission to
Physics in Medicine and Biology

ABSTRACT

The Vanderbilt University Mark-III Free Electron Laser was used to irradiate gelatin and rat dermis samples at $\lambda = 3.3$ and $6.45 \mu\text{m}$. At $\lambda = 3.3 \mu\text{m}$, the primary chromophore in gelatin and tissue is water, whereas at $\lambda = 6.45 \mu\text{m}$ both protein and water absorb the incident radiation. In gelatin, the protein is distributed as globular structures, while in dermal tissue, the protein is assembled into a structural matrix that is capable of supporting significant stresses. The peak pressure generated from FEL irradiation of the samples was measured using a piezoelectric microphone below and above the threshold for material removal. The measured peak pressure as a function of the incident radiant exposure was fit to theoretical models predicting the peak pressure generated from thermoelastic expansion and material ejection. For both wavelengths, it was found that the ablation of gelatin and dermal tissue is explained by a steady-state surface mediated ablation model, regardless of the primary chromophore. The ablation threshold was measured by fitting the surface mediated ablation model to the peak pressure data recorded during material ejection. It was found that there is a significant decrease in the ablation threshold for dermal tissue at $\lambda = 6.45 \mu\text{m}$, compared to the threshold for gelatin, whereas at $\lambda = 3.3 \mu\text{m}$, this decrease was not observed. This suggests that protein absorption by dermal tissues results in the targeted destruction of the structural matrix.

IV.1 INTRODUCTION

Lasers are used to ablate tissue across a wide range of applications and over a wide range of wavelengths. Generally, laser wavelengths that are strongly absorbed are used in order to ensure precise control over the ablation process and to minimize collateral damage. Typically, this indicates the use of ultraviolet (UV) or infrared (IR) sources for cutting or removal of soft tissues. Depending on the laser used and the tissue being irradiated, any one of several responses may be observed arising from a variety of mechanisms. Most soft tissues are primarily composed of liquid water that is surrounded by a solid protein matrix that gives the tissue its mechanical strength. In the UV region of the spectrum, the ArF-excimer laser ($\lambda = 193 \text{ nm}$) is used for ophthalmic procedures such as PRK and LASIK, where the cornea is reshaped by controlled ablation [1]. At this wavelength, the primary chromophore is the peptide bond in collagen, which makes up the extracellular matrix and the ablation mechanism has been described by both photochemical [2] and purely photothermal models [3]. For material to be removed, bonds that hold the tissue together must be broken. The photochemical model of ablation involves the direct absorption and breakage of the peptide bonds [2], while the photothermal model involves the heating and subsequent denaturation of the extracellular matrix which allows for tissue decomposition [3]. In the IR spectrum, CO_2 , Ho:YAG, and Er:YAG lasers are commonly used for incision and excision of tissue. Here, the chromophore is tissue water, and the mechanism of ablation is generally photothermal. In one model, the tissue water absorbs the incident radiation and is heated to a vapor of high temperature and pressure. The expansion of the water vapor formed in the tissue is resisted by the extracellular matrix, but eventually, the pressure in the expanding vapor overcomes the strength of the matrix, and material removal takes place by fracturing the matrix in an explosive process [4–6].

The Vanderbilt University Free Electron Laser (FEL) is a continuously tunable source of pulsed mid-IR radiation with a wavelength tuning range of $\lambda = 2 - 10 \mu\text{m}$. While water is the dominant chromophore over most of this spectral range, there are also several protein absorption bands, most notably the amide II bond at $\lambda = 6.45 \mu\text{m}$. The amide II bond is present in the backbone of amino acid chains which form the structural proteins that make up the extracellular matrix of tissues. By tuning the laser wavelength to the amide II absorption band, it has been suggested that the mechanical integrity of tissues can be targeted directly during ablation [7]. This hypothesis is based on gross histological and mass removal data which has shown that the FEL can ablate tissue with minimal collateral damage at $\lambda = 6.45 \mu\text{m}$ when compared to other IR sources [7]. However, the mechanism of interaction of FEL tissue ablation is still not well understood.

This is in part due to the unique temporal pulse structure of the laser. The Vanderbilt Mark III FEL laser pulse consists of an approximately $5\ \mu\text{s}$ duration macropulse, made up of a 3 GHz pulsetrain of 1 ps duration micropulses, i.e.— there are approximately 14,000 micropulses in one macropulse. Initially, it was thought that the individual micropulses may play a key role in the ablation process, but preliminary time-resolved experiments did not produce any direct evidence to support this [8]. More recently, investigations comparing the results of FEL irradiation with an optical parametric amplifier (OPA) did not provide any evidence supporting picosecond time-scale protein dynamics [9]. Both sources were operated at $\lambda = 6.45\ \mu\text{m}$ and have picosecond duration pulses, but the OPA has a kilohertz repetition rate which reduces its average power by a factor of 10^6 compared to the FEL. During the irradiation of ocular tissue with an equivalent total radiant exposure from both sources, there was no observable effect from the OPA irradiation, suggesting that the individual picosecond pulses do not influence the ablation dynamics [9]. Ruling out picosecond time-scale dynamic effects from the micropulses, we primarily consider the tissue ablation process on the macropulse time-scale.

In this study, time-resolved acoustic measurements are combined with existing theoretical models to characterize the dynamics of soft tissue ablation with a FEL. The measurement of laser-induced stress transients allows the observation of stresses that arise from the transient heating of the tissue as well as the recoil that occurs from material ejection. This permits examination of the mechanisms responsible for ablation at radiant exposures both above and below the threshold for material removal. In this way, we may be able to correlate the transition from subablative exposures to those where material removal is achieved, to physical models based on different mechanisms.

Previous studies have demonstrated the effectiveness of determining physical mechanisms involved in tissue ablation by the study of the laser-induced stresses that are generated in the tissue [3, 4]. In these studies, thin-film piezoelectric transducers were used to measure the near-field acoustic stresses in tissue. In the current study, we attempt to correlate the laser-induced stresses generated in the tissue to those that are coupled into air and recorded with a piezoelectric microphone. While the physical models discussed below have been developed to reflect the stresses generated in the tissue, we argue that the stresses coupled into the surrounding air should be proportional to those in the tissue, and only differ in the magnitude of the response as determined by the acoustic coupling at the air-tissue interface. In this manner, the acoustic stresses recorded in air should reveal valuable information about the transient, dynamic behavior of tissue ablation with a FEL.

Despite the lack of a clear understanding of the mechanism of FEL tissue ablation, it is currently being used in a clinical setting for human neurosurgical [10] and ophthalmological

procedures. The goal of the work presented here is to gain a better understanding of the relationship between the selective absorption of proteins and water at different wavelengths, and the mechanical stresses that are induced by the FEL's temporal pulse structure. In this study, we investigate two hypotheses.

First, the absorption of FEL radiation by proteins leads to the targeted destruction of the tissue structural matrix. This scenario is similar to the mechanism of UV soft tissue ablation, and can only occur at wavelengths where the absorption by protein represents a significant fraction of the overall tissue absorption cross section. For this reason, acoustic stresses were measured in gelatin and rat dermis at $\lambda = 3.3$ and $6.45 \mu\text{m}$. For $\lambda = 3.3 \mu\text{m}$ radiation, water is the dominant chromophore in gelatin and dermal tissue, and absorption by protein is negligible, whereas for $\lambda = 6.45 \mu\text{m}$ radiation, absorption by protein exceeds that of water by up to a factor of 5 [11]. The results from the irradiation of gelatin samples were compared to those from rat dermis at both wavelengths because of the distribution of protein in each sample. In native dermal tissue, the protein primarily exists as part of the structural matrix that gives the tissue its mechanical strength, whereas in gelatin the protein is distributed as large globular clusters which are not capable of supporting significant stresses [11]. We postulate that if protein decomposition is to play a role in the ablation process, we should see a significant difference in the measured ablation threshold between gelatin and dermal tissue of equivalent composition at $\lambda = 3.3 \mu\text{m}$, whereas at $\lambda = 6.45 \mu\text{m}$, we should not. At $\lambda = 3.3 \mu\text{m}$, the dermal tissue should reveal an ablation threshold higher than the gelatin because of the increased strength in the tissue matrix. At $\lambda = 6.45 \mu\text{m}$, we expect that the difference in the measured ablation thresholds to be much smaller. The targeted destruction of the structural matrix in dermal tissue should affect its mechanical strength to a significant degree and lead to a lower ablation threshold that is closer to gelatin.

Second, ablation of dermal tissue with the FEL does not proceed in an explosive manner that is typical of IR ablation with other laser systems. In previous experiments measuring the ablation depth, we have shown that FEL ablation of rat dermis follows a steady-state process [12]. Previously, studies have shown that UV ablation of soft tissue proceeds by a surface-mediated process [3], while IR ablation exhibited an explosive characteristic [4]. We postulate that the relatively long macropulse duration, coupled with the high-frequency micropulse train facilitates a surface-mediated ablation process that is relatively insensitive to changes in the wavelength and chromophore.

IV.2 BACKGROUND

For the radiant exposures achievable with the FEL, the induced stresses generally fall into two categories: thermoelastic expansion and ablative recoil. At radiant exposures below the threshold for ablation, the thermoelastic effect is the primary mechanism by which deposited energy leads to stress generation. At radiant exposures higher than what is necessary to achieve material ejection, the generated stress is dominated by the ablative recoil. When the irradiated volume is ejected from the tissue, the momentum recoil from the ablated products generates a large compressive wave that propagates at high velocity into the tissue [13].

IV.2.1 Thermoelastic Stress

At low radiant exposures, laser radiation is absorbed by the tissue, converted to heat, and the irradiated volume tries to expand. If however, the energy is deposited faster than the time necessary for the mechanical stress to relax, i.e.— for an acoustic wave to propagate out of the irradiated volume, large amplitude compressive stress waves are formed that propagate into the tissue. This situation is known as inertial or stress confinement. When this stress wave is generated at a free surface and in a one-dimensional geometry, one component of the wave propagates into the tissue and another toward the free surface where it undergoes reflection and the polarity reverses. In this way, a bipolar stress wave is created that propagates into the sample.

A complete analysis of the thermoelastic wave equation [14, 15] reveals that for a laser pulse that is effectively a delta function in time irradiating a non-scattering medium, the stress profile follows a Beer's law absorption profile. When the laser spot radius r_s (cm) is larger than the optical penetration depth ($r_s \gg 1/\mu_a$), the problem becomes one-dimensional and the stress profile $\sigma(x)$ is

$$\sigma(x) = \Gamma \mu_a H \exp[-\mu_a x], \quad (\text{IV.1})$$

where μ_a (cm^{-1}) is the absorption coefficient, H (J/cm^2) is the radiant exposure and Γ is the dimensionless Grüneisen coefficient given by

$$\Gamma = \frac{\beta}{\rho c_v \kappa_T}, \quad (\text{IV.2})$$

with thermal expansion coefficient β (K^{-1}), density ρ (g/cm^3), specific heat at constant volume c_v ($\text{J}/\text{g} \cdot \text{K}$), and isothermal compressibility κ_T ($\text{m} \cdot \text{s}^2/\text{g}$). It should be pointed out that Γ is temperature dependent and ranges between 0.11 at $t = 20^\circ\text{C}$ and 0.42 at $t = 100^\circ\text{C}$ for tissue [16]. From this relation, we see that the peak stress σ_p (Pa) generated for inertially

confined laser pulses is

$$\sigma_p \propto \Gamma \mu_a H. \quad (\text{IV.3})$$

The expression for the thermoelastic stress applies to the stress transients generated in the sample, but we are interested in the acoustic transients that are coupled into the surrounding air. Most of the laser-induced thermoelastic stress wave that interacts with the free boundary at the air-sample interface undergoes reflection to generate the bipolar stress wave that propagates into the sample. However, a fraction of the stress wave is transmitted across the interface, which is detected by an airborne microphone. We modify the expression for the thermoelastic stress (Eq. IV.3) to reflect the pressure that is coupled into the surrounding air:

$$p_T = A_T \cdot H, \quad (\text{IV.4})$$

where p_T is the pressure in air resulting from the laser-induced thermoelastic stress and A_T is a constant that incorporates the acoustic coupling at the air-sample interface.

IV.2.2 Steady-State Surface Vaporization

Tissue ablation with UV excimer lasers has generally been associated with incisions that have almost no evidence of thermal injury and produce smooth edges around the ablation sites [1, 17], when performed in air. Further, in experiments using high-speed photography, the ablation plumes appeared to be a fine mist of condensed material [18] indicating that the ablation proceeded on a layer-by-layer basis. For $\lambda = 193 \text{ nm}$ radiation, the tissue chromophore is the protein contained in the extracellular matrix which is responsible for the mechanical strength and integrity of the tissue. Because of the large mass fraction of collagen ($\approx 25 - 30\%$) in tissues such as cornea, dermis, and cartilage, the radiation is very strongly absorbed, and results in an optical penetration depth of $1/\mu_a < 1 \mu\text{m}$ [1, 19]. It has been hypothesized that the means by which the tissue matrix is ablated is photochemical in nature and has been termed “ablative photodecomposition” [2]. At this wavelength, the single photon energy is quite high ($h\nu = 6.43 \text{ eV}$) and it has been suggested that these photons directly break the bonds in the polypeptide chain of collagen since these bonds have a characteristic energy of $\approx 3.0 \text{ eV}$ [20]. However, the UV ablation process has also been described by a purely photothermal mechanism where the extracellular matrix is denatured by the incident radiation (rather than decomposed photochemically) which leads to the targeted destruction of the matrix and material removal [3].

Regardless of the actual mechanism, the results from studies of UV ablation of tissue suggested that the process resembled one of rapid surface vaporization driven by the selective

absorption of proteins in the tissue matrix. This process can be described by the well established “piston model” originally formulated by Landau and Lifshitz [21] and applied to pulsed laser vaporization. Laser irradiation creates a layer of high-temperature, high-pressure gas which rapidly expands. This expansion results in the formation of a shock front emanating from the surface with the vapor following. By applying the laws of conservation of mass, momentum, and energy to this situation, an expression for the pressure in the expanding vapor plume (p_2) can be derived [3]:

$$p_2 = \left\{ \left[\frac{\gamma_1(\gamma_1 + 1)p_1}{2} \right]^{1/2} \frac{(\gamma_2 - 1)q_0}{\gamma_2 c_1} \right\}^{2/3}. \quad (\text{IV.5})$$

Here, p_1 and p_2 are the pressures (Pa) ahead of and behind the expanding shock front, respectively, γ_1 and γ_2 are the ratios of specific heats (c_p/c_v) for the medium ahead of, and behind the shock, respectively, and c_1 is the sound speed in the medium ahead of the shock. This relation is derived assuming a steady state vaporization driven by the laser irradiance q_0 . When applied to pulsed laser irradiation, the irradiance is replaced by the radiant exposure divided by the pulse duration H/t_p . Also, assuming that a threshold radiant exposure (H_{th}) is necessary to initiate material ejection, this must be subtracted from the radiant exposure absorbed by the target, which leads to the following expression for the peak pressure in the vapor plume:

$$p_2 = A_R \cdot (H - H_{\text{th}})^{2/3}, \quad (\text{IV.6})$$

where A_R ($\text{kg}^{1/3}/\text{m} \cdot \text{s}^{2/3}$) is a free parameter that can be adjusted to best fit the data and must satisfy the condition that

$$A_R \leq \left\{ \left[\frac{\gamma_1(\gamma_1 + 1)p_1}{2} \right]^{1/2} \frac{(\gamma_2 - 1)}{\gamma_2 c_1 t_p} \right\}^{2/3} \quad (\text{IV.7})$$

in order to ensure that the kinetic energy of the expanding vapor does not exceed the total energy available in the ablation process. When fit to experimental data, the parameter A_R represents the fraction of the acoustic energy that is coupled into the transducer.

Previously, this model has been used to describe the stress that is generated in the tissue as a result of the ablative recoil [3]. The model is based on the assumption that the pressure in the expanding vapor plume is proportional to the recoil stress that is coupled into the tissue. For our experiment, the airborne microphone performs a direct measurement of the pressure in the vapor plume, rather than an indirect measurement of the corresponding recoil stress.

IV.2.3 Explosive Characteristics of IR Ablation

Soft tissue ablation with IR sources has been described in many studies as having an explosive characteristic. This characteristic has been explained in terms of a phenomenon known as flash boiling or spinodal decomposition. Flash boiling involves the superheating of water to temperatures well above the boiling point, which is followed by a phase explosion. The phase explosion occurs when the superheated water reaches the spinodal limit, which is $\approx 90\%$ of the critical temperature [22]. The process of flash boiling has been shown to be a viable ablation mechanism in several studies involving IR irradiation [4, 6, 23, 24].

Two conditions have been formulated by Venugopalan et al. [4] under which flash boiling may be a viable mechanism for tissue ablation. First, a microscale thermal confinement must be established within the tissue chromophore. This occurs when the laser pulse duration is less than the time necessary for heat to diffuse across the characteristic length of the chromophore,

$$t_p < \tau_\delta = \delta^2/\alpha. \quad (\text{IV.8})$$

Here, τ_δ is the thermal diffusion time across the characteristic chromophore length, δ is the characteristic chromophore length, and α is the thermal diffusivity of the chromophore. For flash boiling of the tissue water, we assume values of $\alpha = 1.5 \times 10^{-3} \text{ cm}^2/\text{s}$ and $\delta = 10^{-4} \text{ cm}$ [4], and estimate the thermal diffusion time across the layer to be $\tau_\delta = 6.7 \mu\text{s}$. For the FEL pulse duration of $t_p = 5 \mu\text{s}$, the first condition is satisfied. The second condition is that the rate of energy deposition must be much greater than the rate of energy consumption by the growth of bubble nucleation centers formed below the tissue surface. By analyzing the rate of vapor bubble growth, Venugopalan et al. [4] has made an estimate of the volumetric power density that is necessary for flash boiling to occur within soft tissues. For the irradiation conditions at both $\lambda = 3.3$ and $6.45 \mu\text{m}$, the FEL is capable of $\approx 10^8 \text{ W}/\text{cm}^3$ near the ablation threshold in dermal tissue, which is significantly below the estimated requirement of $\approx 10^{12} \text{ W}/\text{cm}^3$ for the FEL pulse duration. Since the second condition is not satisfied, we expect that FEL ablation of soft tissue will not proceed in an explosive manner, but by a surface-mediated process.

IV.3 EXPERIMENTAL METHODS

Gelatin and rat skin samples were used to investigate the effect of laser induced stresses. The hot-cast collagen gels were prepared by melting 30% gelatin by mass into hot water, which is approximately equal to the concentration of protein in native dermis. The gels were solidified in a refrigerator for at least 1 hour prior to irradiation. Rat skin samples were

harvested from sacrificed albino rats within 24 hours post-mortem. The skin was shaved and depilated using Nair and cleansed multiple times. Thin strips of skin approximately 1×5 cm were removed from the ventral side, cleaned of fascia, and stored in a refrigerator on 4% saline soaked gauze until use. The skin strips were used within 24 hours of harvesting, and prior to irradiation, the strips were again cleaned of any remaining fascia on the dermal side.

The experimental setup for measuring the acoustic signals is shown in Figure IV.1. The FEL beam is Gaussian and linearly polarized. A double Brewster-plate polarizer (II-VI, Inc., Saxonburg, Pennsylvania) was used to attenuate the beam and vary the incident pulse energy. A portion of the beam ($\approx 10\%$) is picked off with a CaF_2 window and the pulse energy is monitored with pyroelectric detector (J8, Molectron, Portland, Oregon) and energy meter (EPM2000, Molectron, Portland, Oregon). The FEL beam is focused onto the gelatin sample with a CaF_2 lens ($f = 200$ mm) and the lens position was adjusted along the optical axis to produce a 1 mm diameter spot measured with a scanning knife-edge [25]. Prior to sample irradiation, a second pyroelectric detector (J50, Molectron, Portland, Oregon) was placed at the sample location, and a ratio measurement was made to calibrate the pulse energy monitored during irradiation to the pulse energy actually delivered to the sample. This pulse energy was divided by the $1/e^2$ laser spot area to calculate the incident radiant exposure (J/cm^2). Gelatin and rat dermis samples were irradiated with the FEL at $\lambda = 3.3$ and $6.45 \mu\text{m}$ at radiant exposures of $0.1 \leq H \leq 4.0 \text{ J}/\text{cm}^2$.

The acoustic transducer used to record the signals is a piezoelectric microphone (132A42, PCB Piezotronics, Depew, New York) with a bandwidth of 1 MHz and a sensitivity of 2125 mV/psi. The microphone is positioned as close to the optical axis as the FEL beam allows ($\approx 30^\circ$) and directed toward the irradiated surface. The distance from the sample surface was adjusted such that there was a $90 \mu\text{s}$ delay between the beginning of the laser pulse and the rising edge of the acoustic wave, corresponding to ≈ 3 cm. This ensured the amplitude of the recorded signals was comparable from one experiment to the next. The signals were captured and saved on a digitizing oscilloscope (TDS 640A, Tektronics, Wilsonville, Oregon) for post-experimental processing and analysis.

To ensure a positive correlation between the peak pressure in air and the peak compressive stress in the sample during ablation, the microphone was cross-calibrated against a piezoelectric hydrophone. The hydrophone was placed in a gelatin sample below the surface, and directed toward the surface. The microphone was kept in air as described above, and the two signals were recorded simultaneously at several radiant exposures at $\lambda = 6.45 \mu\text{m}$.

IV.4 RESULTS

IV.4.1 Acoustic Cross-Calibration

The piezoelectric microphone was cross-calibrated with a piezoelectric needle hydrophone to ensure that the peak pressure recorded in air corresponds to the peak stress in the sample. Figure IV.2 shows the results of the cross-calibration. For low radiant exposures, the response is linear. As the radiant exposure increases, the relationship between the microphone and hydrophone response begins to deviate from linear. It should be noted that the transition from the thermoelastic region to that of material ejection occurs for a microphone response of approximately 150 mV under the irradiation conditions. The point at which the microphone response starts to become nonlinear (≈ 1500 mV) corresponds to a radiant exposure of ≈ 2.5 J/cm².

IV.4.2 Peak Pressure Measurements

The peak pressure recorded from the irradiation of gelatin and rat skin at $\lambda = 3.3$ μ m is plotted as a function of radiant exposure in Figure IV.3. Two observations stand out when looking at the raw data. First, we can see a clear transition from the linear thermoelastic region at low radiant exposures to the ablative recoil region at high radiant exposures. This transition is remarkably distinct and is a clear indicator of the ablation threshold. Second, the peak pressures recorded for both the tissue and the gelatin are nearly identical. By noting the transition from thermoelastic expansion to ablative recoil in the peak pressure, we can estimate the ablation threshold to be ≈ 0.6 J/cm² for both the tissue and gelatin.

Similar observations can be made from the peak pressure recorded from irradiation at $\lambda = 6.45$ μ m, seen in Figure IV.4. For both the gelatin and tissue samples, there is clear transition from the thermoelastic region to ablative recoil. However, this transition occurs at different radiant exposures for the two samples. For the gelatin, the ablation threshold appears to be ≈ 0.5 J/cm², but the threshold for dermal tissue appears to be significantly lower, near ≈ 0.3 J/cm².

The models for the predicted peak pressure described in section IV.2 were applied to the measured data. Figure IV.5 shows the results of the data analysis for both gelatin and rat skin at $\lambda = 3.3$ μ m. For both samples, we see that the steady-state surface vaporization model (Eq. IV.6) explains the vapor plume peak pressure data well. For gelatin, the value of the ablation threshold calculated by applying the surface vaporization model to the ablative recoil data is $H_{\text{th}} = 0.71$ J/cm², and for dermis $H_{\text{th}} = 0.63$ J/cm², which is only a 12%

difference. This result is different from our hypothesis where we predicted that there would be a significantly larger ablation threshold for rat dermis than gelatin because of the increased mechanical strength in the tissue due to its structural protein matrix.

At $\lambda = 6.45 \mu\text{m}$ (Figure IV.6), again we see that the steady-state surface vaporization model describes the vapor plume peak pressure data well. As we noted from the raw data (Figure IV.4), there appeared to be a significant difference between the ablation thresholds in gelatin and skin. This is confirmed when applying the surface vaporization model, which calculated $H_{\text{th}} = 0.48 \text{ J/cm}^2$ for gelatin. The ablation threshold calculated for the dermal tissue is $H_{\text{th}} = 0.30 \text{ J/cm}^2$, which is a factor of 1.6 smaller than gelatin. Here again, this result is different from our hypothesis where we predicted that the ablation thresholds for the rat dermis and gelatin would be similar due to targeted destruction of the tissue matrix.

In Figures IV.5 and IV.6, we see from the inset plots that the linear thermoelastic scaling applies well to the subthreshold peak pressure data. At $\lambda = 3.3 \mu\text{m}$ (Figure IV.5), the subthreshold data points are very linear for the gelatin sample, while for skin, there is considerably more noise present. At $\lambda = 6.45 \mu\text{m}$ (Figure IV.6), both gelatin and skin subthreshold data show good linearity. Further, we can see very clearly the significant difference in the ablation threshold for the two samples.

IV.5 DISCUSSION

IV.5.1 Acoustic Measurements in Air

The acoustic cross-calibration (Figure IV.2) shows that for small radiant exposures, there is a linear relationship between the peak pressure measured in air, and the peak stress measured in the sample. The linearity breaks down however at a microphone response of $\approx 1500 \text{ mV}$. For the irradiation conditions of the cross-calibration, the ablation threshold occurs at the microphone signal level of $\approx 150 \text{ mV}$. This point is well below the point at which the response begins to deviate from linear, which gives us confidence that the peak pressure measured in air corresponds well to the peak stress measured in the sample. The response begins to deviate from linear at $\approx 1500 \text{ mV}$. At this point, the radiant exposure is $\approx 2.5 \text{ J/cm}^2$ which is near the upper bound of our exposure limit for the irradiation conditions of the peak pressure experiments in gelatin and dermis. For large incident exposures, there are several reasons that the hydrophone response may become nonlinear, thus making the cross-calibration between the two transducers nonlinear as well. In previous experiments using high-speed pump-probe imaging to investigate gelatin ablation, we have observed strong secondary shocks that propagate into the sample for large radiant expo-

tures. These secondary shocks may be superimposed on spurious signals due to multiple reflections, or with the natural ringing from the hydrophone output. If the signals from the multiple reflections or secondary shocks are large enough, the peak pressure recorded with the hydrophone would become artificially large, thereby producing the nonlinearity in the cross-calibration.

IV.5.2 Surface Mediated Ablation

The results of FEL irradiation of gelatin and skin for $\lambda = 3.3$ and $6.45 \mu\text{m}$ show that the measured peak pressures from ablative recoil follow those predicted by the steady-state surface vaporization model. At $\lambda = 6.45 \mu\text{m}$, both the protein structural matrix of tissue and the water that is bound within it are absorbing the incident radiation, while at $\lambda = 3.3 \mu\text{m}$ the only tissue component absorbing the incident radiation is water. Because of this, one might expect that the ablation dynamics at these two wavelengths to be significantly different. However, this result is consistent with previous measurements of the ablation depth in dermal tissue which have shown that, to a first approximation, soft tissue ablation with the FEL is governed by a steady-state ablation process over a broad range of wavelengths in the IR ($\lambda = 2.65$ to $6.7 \mu\text{m}$) [12]. This result is also consistent with our hypothesis that the ablation process follows a surface mediated process, and is not explosive in nature.

These findings are consistent with the physical picture of steady-state ablation. One description of the process by Hibst and Keller [26] is that the total incident radiant exposure is divided into many subpulses. Each of the subpulses is delivered to the target and converted to heat, and the heat from subsequent pulses is added. After a sufficient number of subpulses have been delivered to the target, the ablation threshold is reached, and all of the following subpulses remove a fine layer of tissue until the end of the laser pulse. Conceptually, this scenario is identical to the actual FEL macropulse. The energy contained in a single micropulse is insufficient to ablate, so many micropulses must be delivered to reach the ablation threshold. Once material removal begins, there is a quasi-continuous train of micropulses, each of which removes a fine layer of tissue. Keeping this picture in mind, it is not surprising that FEL ablation proceeds by a surface mediated process and that the surface vaporization model fits the recorded peak pressure during material removal.

IV.5.3 Role of Protein Absorption

The results of FEL ablation at $\lambda = 6.45 \mu\text{m}$ showed that there was a significant difference in the ablation threshold for gelatin and rat dermis samples, while at $\lambda = 3.3 \mu\text{m}$ there was

very little. At $\lambda = 3.3 \mu\text{m}$, the chromophore in both samples is water and protein absorption is negligible, while at $\lambda = 6.45 \mu\text{m}$ the contribution of protein to the overall absorption cross section is significant [8, 11]. The fact that there is a difference in the ablation thresholds at the two wavelengths shows us that the protein absorption plays a significant role in the ablation dynamics. However, the results of the measured ablation threshold for the different wavelengths and samples conflict with our hypothesis. If the material strength of the tissue structural matrix plays an important role in the ablation dynamics, one would expect that the measured ablation thresholds would be significantly different for wavelengths where protein absorption does *not* occur. For example, at $\lambda = 3.3 \mu\text{m}$, water is the chromophore, and presumably, material ejection begins when the pressure in the expanding vapor bubble is greater than the strength of the material. Since gelatin does not have a structural matrix to resist the expansion of the vapor, we would expect less energy to be required for ablation to begin, whereas in skin, the tissue matrix would counteract the expansion of the water vapor, and require more energy in a given volume to initiate ablation. Further, if we consider $\lambda = 6.45 \mu\text{m}$, we would expect the measured ablation thresholds to be more similar for gelatin and skin, since our premise is that the tissue structural matrix is compromised during $\lambda = 6.45 \mu\text{m}$ irradiation. If this is the case, then the effect that the structural matrix has on resisting the expansion of vaporized water would be negated, and the energy required for material ejection to occur would be more similar.

This discrepancy can be explained when considering the relative concentrations of protein and water in the gelatin and skin samples. The gelatin samples were prepared with 70% water by mass to mimic the absorption properties of native dermal tissue. However, we do not accurately know the level of hydration of the tissue at the time of irradiation. We assume that the tissue is 70% water, but in fact, it may be significantly lower than this. Normally, we would expect the ablation threshold to be higher in dermis than in gelatin when the primary chromophore is water. If however, the water content is higher in the tissue than the gelatin, we would see a decrease in the ablation threshold of the tissue, due to the increase in the absorption cross section of the sample. This explanation is consistent with our data at $\lambda = 3.3 \mu\text{m}$ which showed a decrease in the ablation threshold of dermis, presumably due to a higher water content, and thus a larger absorption cross section. The same reasoning applies to the data from $\lambda = 6.45 \mu\text{m}$, where the ablation threshold for dermis is significantly lower than for gelatin. Here, if we assume the water content in the dermal tissue is higher than the gelatin, then the ablation threshold would be lower, relative to the gelatin threshold. This effect of decreasing the threshold is enhanced by the protein absorption, where the tissue matrix is compromised by the irradiation. As the protein matrix is destroyed, the resistance to the formation of vapor bubbles is decreased, and material removal occurs with

lower incident energy, hence the significantly lower ablation threshold. The important point to bear in mind is that the *relative* difference in the ablation thresholds between gelatin and dermal tissue is significant wavelengths where protein absorption represents a significant fraction of the overall absorption cross section.

For the above argument to be valid, the tissue matrix must be structurally compromised on the time scale of the laser pulse. By applying the theory of absolute reaction rates to collagen denaturation, the amount of time the collagen must be exposed to a given temperature in order for denaturation to occur can be calculated [3]. It has been calculated that for an exposure time of $1 \mu\text{s}$ a temperature rise of only $\approx 95 - 100 \text{ }^\circ\text{C}$ would be sufficient to fully denature the collagen contained in the tissue structural matrix. This further supports our hypothesis that the absorption of $\lambda = 6.45 \mu\text{m}$ radiation leads to the targeted destruction of the tissue structural matrix.

IV.6 CONCLUSIONS

The peak pressure as a function of radiant exposure generated from the irradiation of gelatin and rat dermis at $\lambda = 3.3$ and $6.45 \mu\text{m}$ has been measured. It has been shown that the peak pressure measured in air correlates with the peak compressive stress in the sample, and by fitting the recorded data to theoretical models, we can make an accurate measurement of the ablation threshold.

The measured peak pressure in the vapor plume during material removal is well described by the surface vaporization model, independent of the wavelength and chromophore in the sample. This suggests that the ablation of soft tissues with a FEL proceeds by a surface mediated process, and is not explosive in nature, as is typical of ablation with other IR sources. We attribute this result in part to the duration of the macropulse, as well as the micropulse structure itself. The macropulse duration is too long to achieve a blow-off ablation scenario where all of the laser pulse energy is delivered before material ejection begins, and so ablation proceeds in a steady-state manner. The micropulse structure of the FEL pulse aids the surface mediated material ejection by removing a fine layer of tissue for each micropulse, once the ablation threshold is reached.

The role of protein absorption was investigated by comparing the ablation thresholds measured in gelatin and rat dermis at two wavelengths, $\lambda = 3.3$ and $6.45 \mu\text{m}$. For $\lambda = 3.3 \mu\text{m}$ irradiation, water is the chromophore and protein absorption is negligible, while at $\lambda = 6.45 \mu\text{m}$, the absorption of protein represents a significant fraction of the overall absorption cross section in the samples. The results show that there is a significant decrease in the ablation threshold measured in dermal tissue which has a structural matrix, over

that of gelatin, which does not, when protein absorption is significant ($\lambda = 6.45 \mu\text{m}$). This suggests that the material strength of the tissue is compromised by the targeted destruction of the structural matrix, leading to a decrease in the relative ablation threshold. A decrease in the ablation threshold suggests that less laser pulse energy is necessary for the ablation of collagenous tissues, which is one possible explanation for the clinical observation that ablation with the FEL at $\lambda = 6.45 \mu\text{m}$ produces incisions with minimal collateral damage.

ACKNOWLEDGEMENTS

This research was supported in part by a grant from the Department of Defense through the MFEL Program under Award No. F49620-01-1-0429 and a Dissertation Enhancement Grant from the Graduate School at Vanderbilt University.

REFERENCES

- [1] Puliafito CA, Steinert RF, Deutsch TF, Hillenkamp F, Dehm EJ, Adler CM, “Excimer laser ablation of the cornea and lens,” *Ophthalmology*, 92(6):741–748, 1985.
- [2] Srinivasan R, Dyer PE, Braren B, “Far-ultraviolet laser ablation of the cornea: Photoacoustic studies,” *Lasers in Surgery and Medicine*, 6(6):514–519, 1987.
- [3] Venugopalan V, Nishioka NS, Mikic BB, “The thermodynamic response of soft biological tissues to pulsed ultraviolet laser irradiation,” *Biophysical Journal*, 69:1259–1271, 1995.
- [4] Venugopalan V, Nishioka NS, Mikic BB, “The thermodynamic response of soft biological tissues to pulsed infrared-laser irradiation,” *Biophysical Journal*, 70:2981–2993, 1996.
- [5] Marjaron B, Plestenjak P, Lukač M, “Thermo-mechanical laser ablation of soft biological tissue: modeling the micro-explosions,” *Applied Physics B*, 69:71–80, 1999.
- [6] Nahen K, Vogel A, “Shielding by the ablation plume during Er:YAG laser ablation,” in *Laser-Tissue Interaction XII*, vol. 4257, SPIE, 2001.
- [7] Edwards G, Logan R, Copeland M, Reinisch L, Davidson J, Johnson B, Maciunas R, Mendenhall M, Ossoff R, Tribble J, Werkhaven J, O’Day D, “Tissue ablation by a free-electron laser tuned to the amide II band,” *Nature*, 371:416–419, 1994.
- [8] Tribble J, Lamb DC, Reinisch L, Edwards G, “Dynamics of gelatin ablation due to free-electron laser irradiation,” *Phys. Rev. E*, 55:7385–7389, 1997.

- [9] Edwards G, Hutson MS, Hauger S, Kozub J, Shen J, Shieh C, Topadze K, Joos K, “Comparison of OPA and Mark-III FEL for tissue ablation at $6.45\mu\text{m}$,” in *Commercial and Biomedical Applications of Ultrafast and Free-Electron Lasers*, Edwards GS, Neev J, Ostendorf A, Sutherland JC, eds., vol. 4633, pp. 194–200, SPIE, Bellingham, WA, USA, 2002.
- [10] Copeland ML, Cram G, Gabella B, Jansen ED, Mongin JD, Pratisto HS, Uhlhorn SR, Edwards GS, “First human application of a free-electron laser,” *Lancet*, submitted.
- [11] Yannas IV, “Collagen and gelatin in the solid state,” *Journal of Macromolecular Science—Reviews in Macromolecular Chemistry*, C7(1):49–104, 1972.
- [12] Uhlhorn SR, Mackanos MA, Jansen ED, “Free electron laser ablation of soft tissue: Measurement of ablation depth and threshold,” *Lasers in Surgery and Medicine*, 2001.
- [13] Esenaliev RO, Oraevsky AA, Letokhov VS, Karabutov AA, Malinsky TV, “Studies of acoustical and shock waves in the pulsed laser ablation of biotissue,” *Lasers in Surgery and Medicine*, 13:470–484, 1993.
- [14] Venugopalan V, *The Thermodynamic Response of Polymers and Biological Tissues to Pulsed Laser Irradiation*, Ph.D. thesis, Massachusetts Institute Of Technology, 1994.
- [15] Bushnell JC, McCloskey DJ, “Thermoelastic stress production in solids,” *Journal of Applied Physics*, 39(12):5541–5546, 1968.
- [16] Jacques SL, Gofstein G, Dingus RS, “Laser-flash photography of laser-induced spallation in liquid media,” in *Laser-Tissue Interaction III*, vol. 1646, pp. 284–294, SPIE, 1992.
- [17] Puliafito CA, Wong K, Steinert RF, “Quantitative and ultrastructural studies of excimer laser ablation of the cornea at 193 and 248 nanometers,” *Lasers in Surgery and Medicine*, 7(2):155–159, 1987.
- [18] Puliafito CA, Stern D, Kreuger RR, Mandel ER, “High-speed photography of excimer laser ablation of the cornea,” *Archives of Ophthalmology*, 105(9):1255–1259, 1987.
- [19] Ediger MN, Petit GH, Weiblinger RP, Chen CH, “Transmission of corneal collagen during ArF excimer laser ablation,” *Lasers in Surgery and Medicine*, 13(2):204–210, 1993.
- [20] Wetlaufer DB, “Ultraviolet spectra of proteins and amino acids,” in *Advances in Protein Chemistry*, Anfinsen Jr. CB, Anson ML, Bailey K, Edsall J, eds., vol. 17, pp. 304–390, Academic Press, New York, 1962.

- [21] Landau LD, Lifshitz EM, *Fluid Mechanics*, Pergammon Press, 2nd edn., 1987.
- [22] Martynyuk MM, “Phase explosion of a metastable fluid,” *Combust. Explos. Shock Waves*, 13:178–191, 1977.
- [23] Esenaliev RO, Oraevsky AA, Lethokov VS, “Laser ablation of atherosclerotic blood vessel tissue under various irradiation conditions,” *IEEE Transactions in Biomedical Engineering*, 36:1188–1194, 1989.
- [24] Oraevsky AA, Esenaliev RO, Letokhov VS, “Temporal characteristics and mechanism of atherosclerotic tissue ablation by nanosecond and picosecond laser pulses,” *Lasers Life Sci.*, 5:75–93, 1992.
- [25] Khosrofian JM, Garetz BA, “Measurement of a gaussian laser-beam diameter through the direct inversion of knife-edge data,” *Applied Optics*, 22(21):3406–3410, 1983.
- [26] Hibst R, Keller U, “Experimental studies of the application of the Er:YAG laser on dental hard substances: I. Measurement of the ablation rate,” *Lasers in Surgery and Medicine*, 9:338–344, 1989.

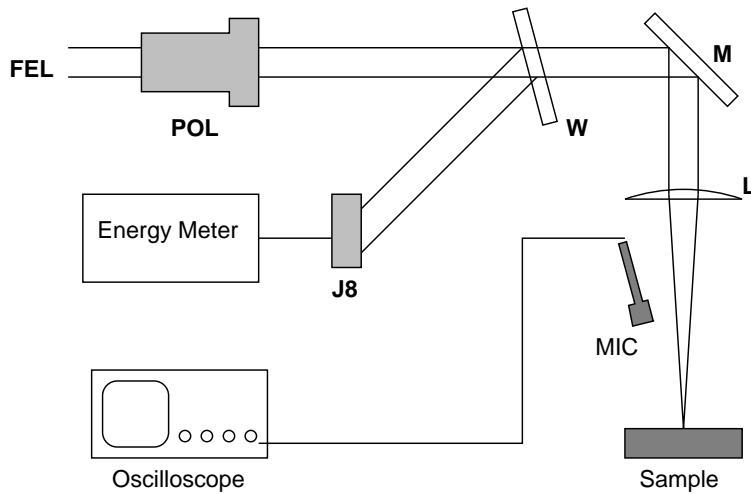


Figure IV.1: Experimental setup for measuring the peak pressure generated during FEL irradiation. The linearly polarized FEL beam is attenuated with a polarizer (POL) to vary the pulse energy. A CaF₂ window (W) picks off a portion of the beam ($\approx 10\%$) which is monitored by a pyroelectric detector (J8) and energy meter. A mirror (M) directs the beam through an $f = 200$ mm CaF₂ lens (L), where it is focused onto the gelatin surface. A piezoelectric microphone (MIC) detects the acoustic signature after laser irradiation, and the signal is recorded and saved with a digital storage oscilloscope.

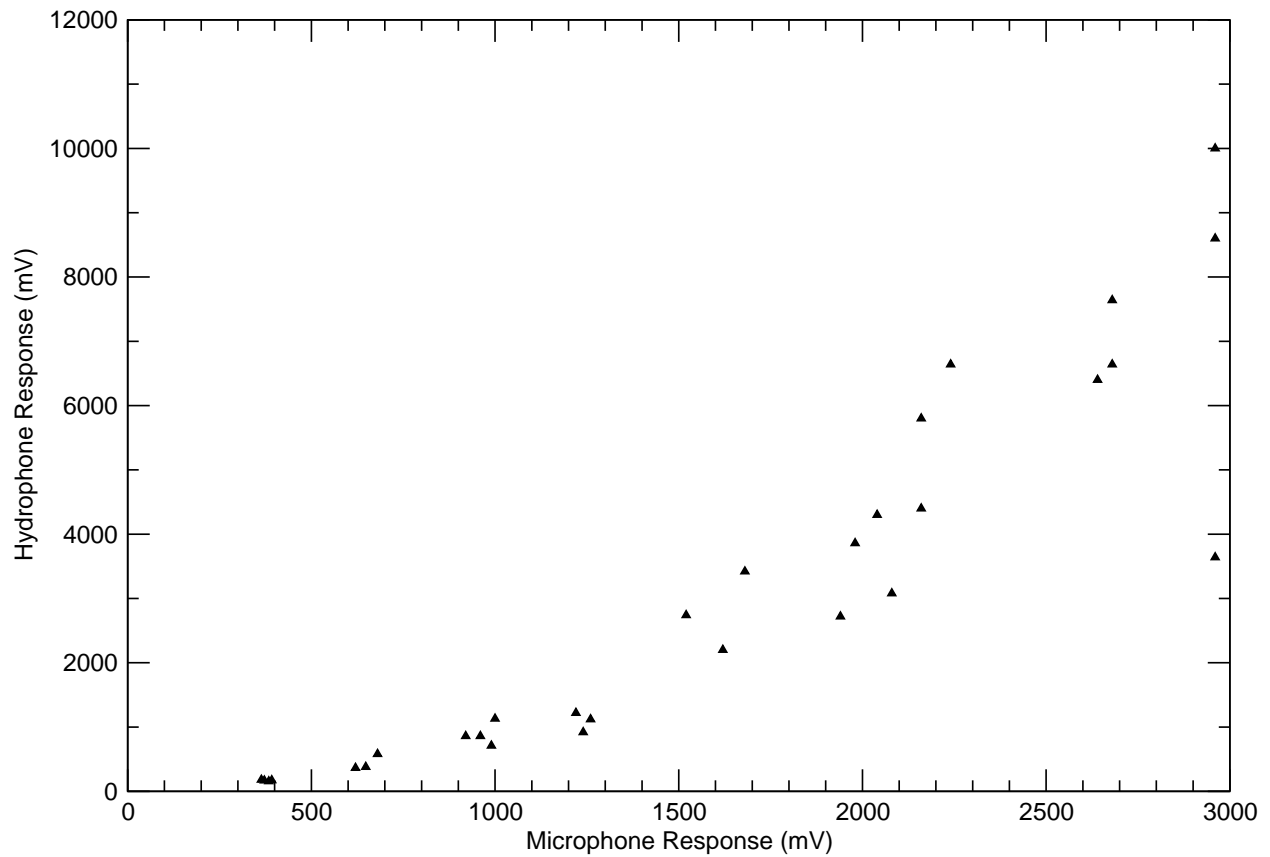


Figure IV.2: Cross-calibration of piezoelectric microphone and piezoelectric needle hydrophone. Gelatin was irradiated at $\lambda = 6.45 \mu\text{m}$ and the peak pressure in air was recorded simultaneously with the peak compressive stress in the gelatin for several radiant exposures.

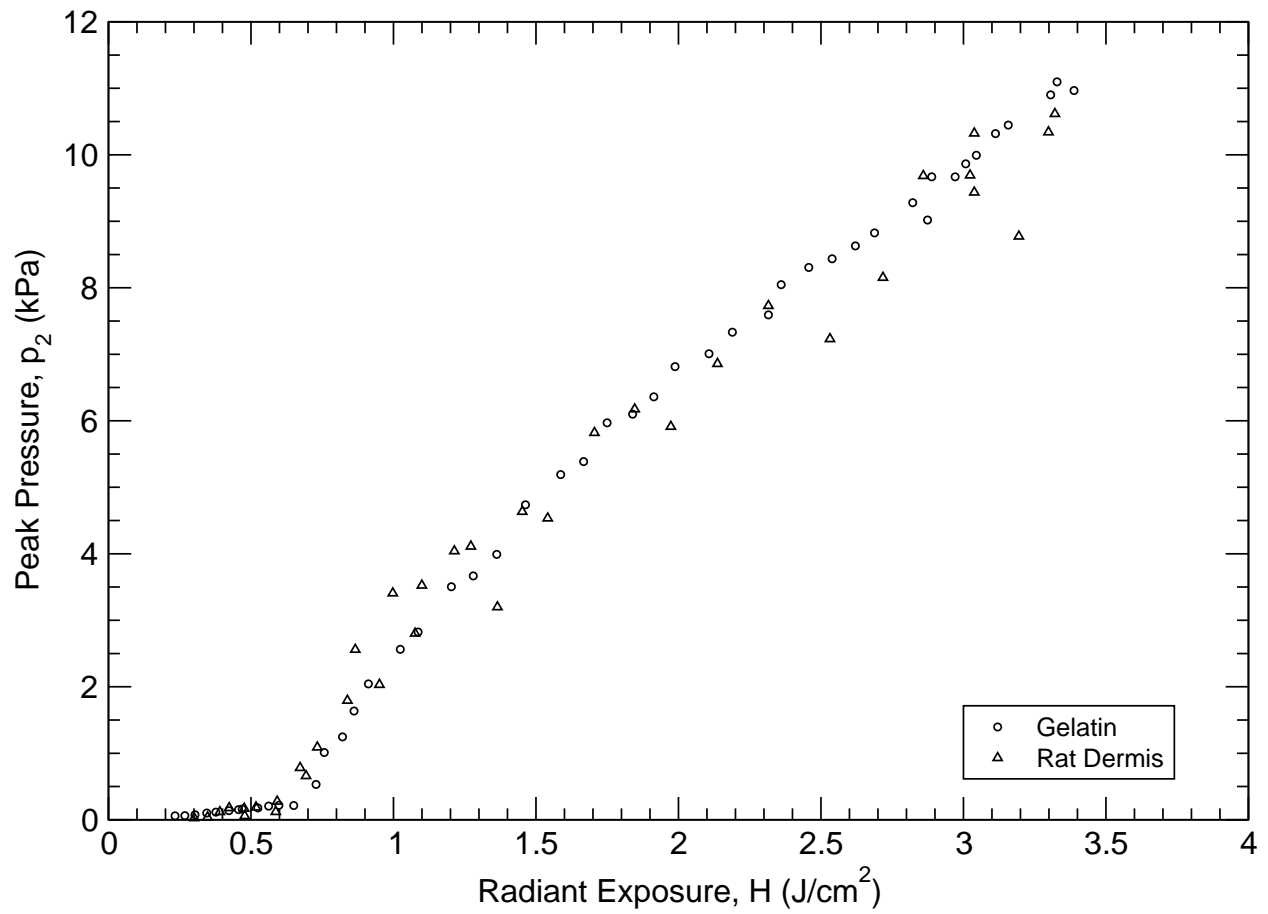


Figure IV.3: Recorded peak pressure as a function of radiant exposure at $3.3 \mu\text{m}$ in gelatin and rat dermis.

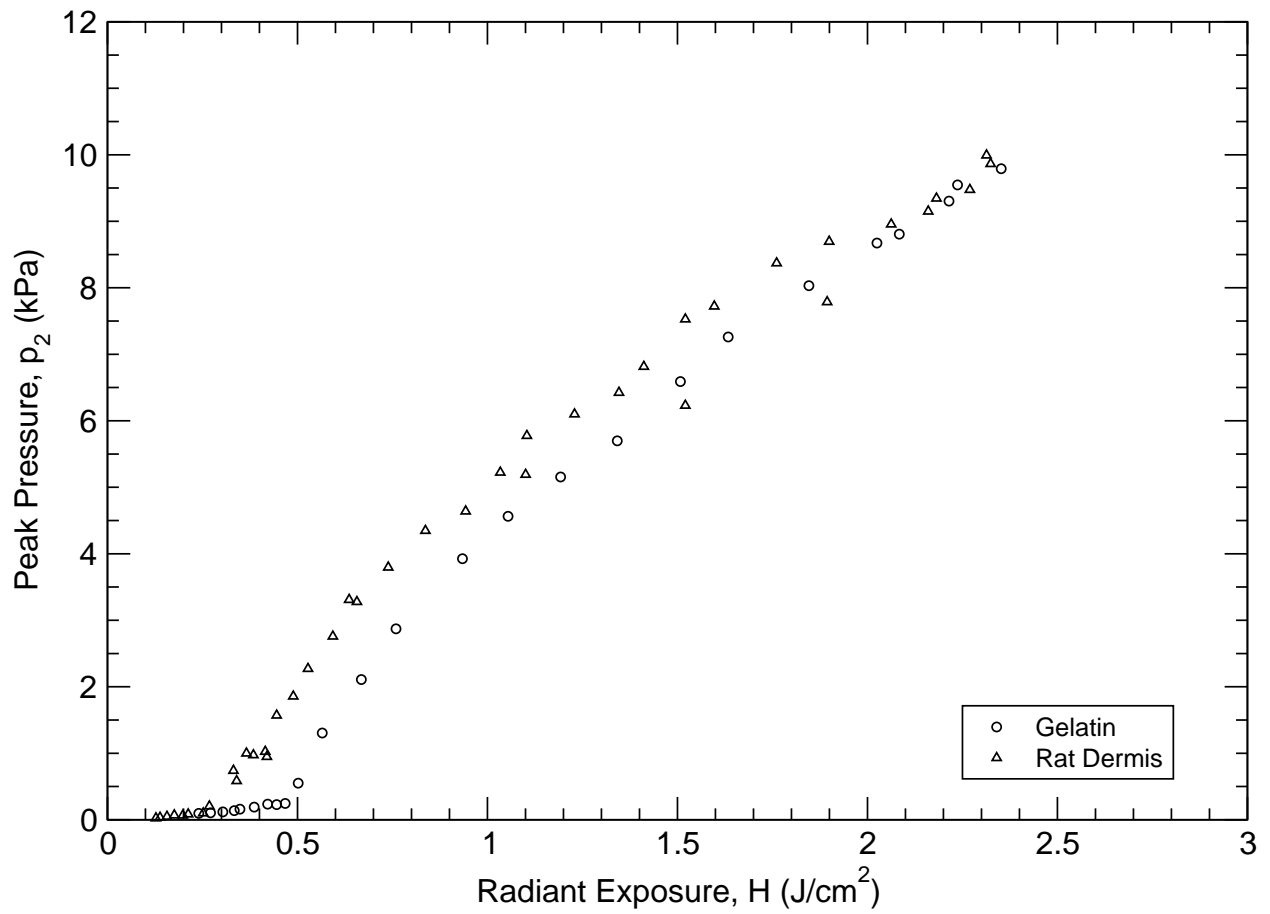


Figure IV.4: Recorded peak pressure as a function of radiant exposure at $6.45 \mu m$ in gelatin and rat dermis.

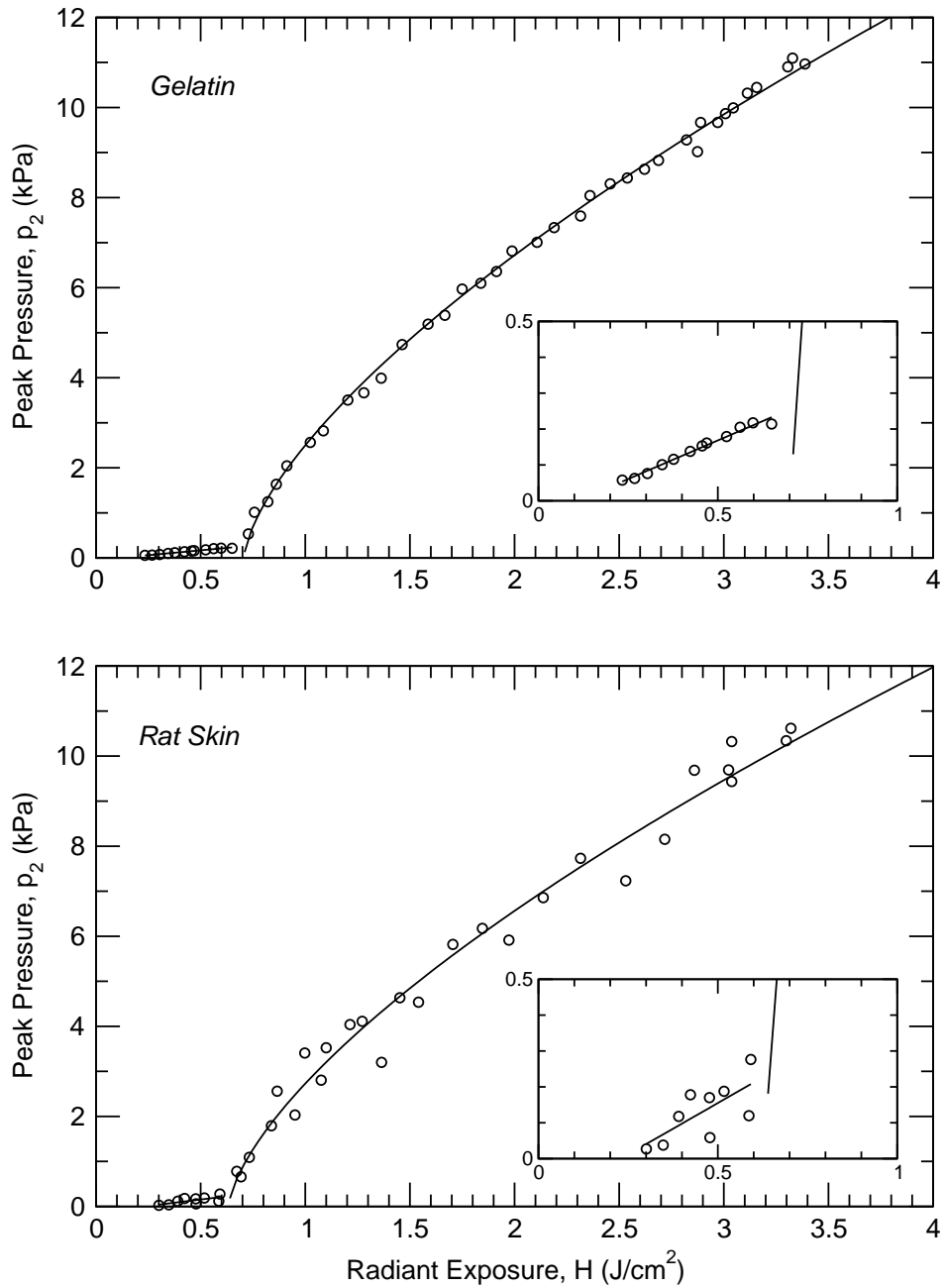


Figure IV.5: Model fit of peak pressure as a function of radiant exposure from irradiation of gelatin and rat dermis at $3.3\ \mu\text{m}$. The ablation data was fit to the steady-state surface vaporization model (Eq. IV.6) for both samples. For gelatin, the data fit calculated $H_{\text{th}} = 0.71\ \text{J/cm}^2$ and for rat dermis, $H_{\text{th}} = 0.63\ \text{J/cm}^2$. The inset plot shows an expanded view of the subablative data which is fit to relationship for thermoelastic expansion (Eq. IV.4).

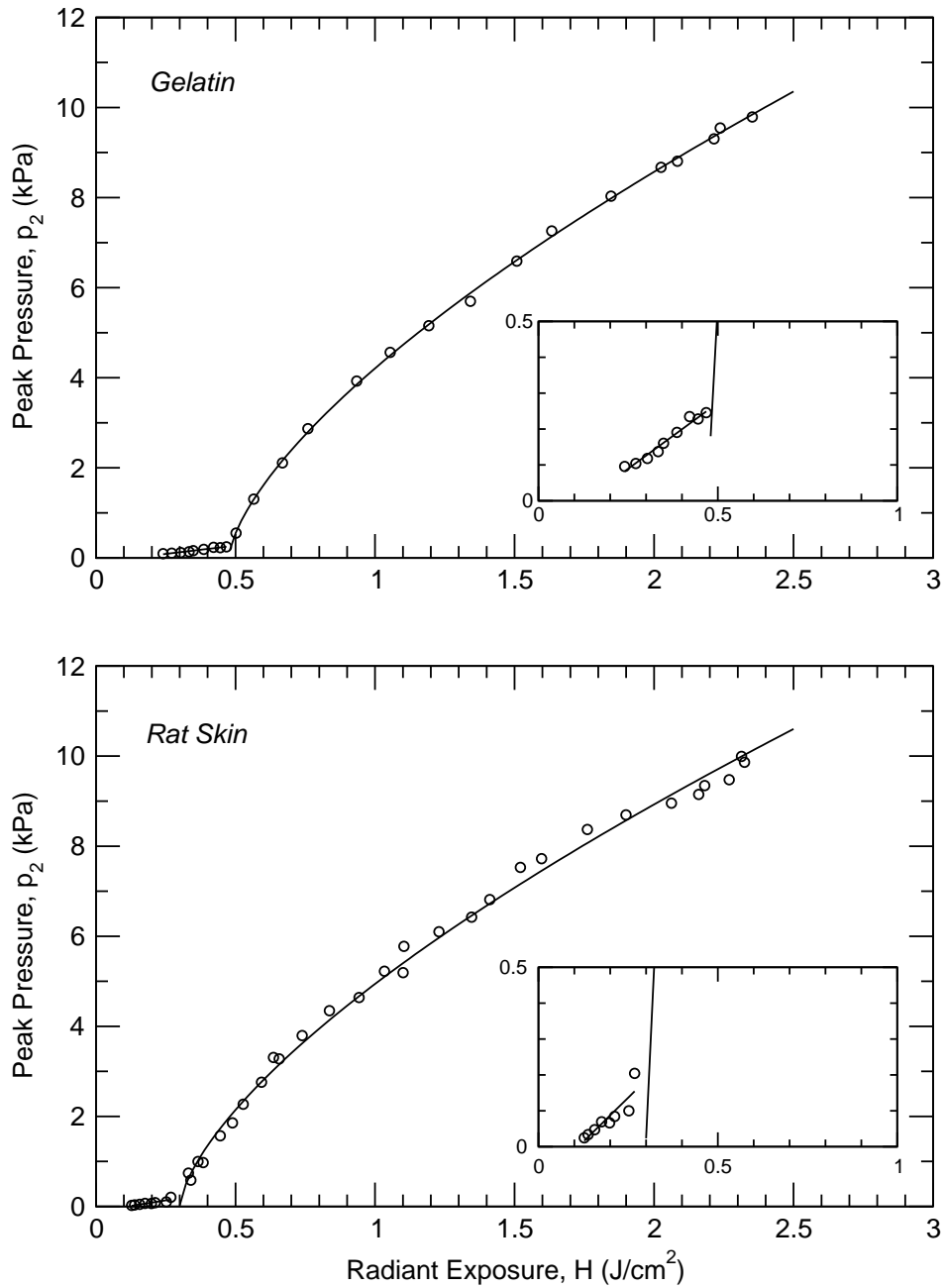


Figure IV.6: Model fit of peak pressure as a function of radiant exposure from irradiation of gelatin and rat dermis at $6.45 \mu m$. The ablation data was fit to the steady-state surface vaporization model (Eq. IV.6) for both samples. For gelatin, the data fit calculated $H_{th} = 0.48 J/cm^2$ and for rat dermis, $H_{th} = 0.30 J/cm^2$. The inset plot shows an expanded view of the subablative data which is fit to relationship for thermoelastic expansion (Eq. IV.4).

CHAPTER V

MODELING THE EFFECTS OF PULSE STRUCTURE AND DYNAMIC ABSORPTION
DURING FREE ELECTRON LASER ABLATION OF SOFT TISSUE

Stephen R. Uhlhorn^{1,2}, E. Duco Jansen¹
and Richard A. London²

¹Vanderbilt University
Department of Biomedical Engineering
Nashville, TN

²Lawrence Livermore National Laboratory
Livermore, CA

In preparation for submission to
Applied Optics

V.1 INTRODUCTION

The Vanderbilt University Mark-III Free Electron Laser (FEL) is a continuously tunable source of pulsed mid-infrared radiation with a wavelength tuning range of $\lambda \approx 2 - 10 \mu\text{m}$. This makes the FEL well suited for tissue ablation since most soft tissues are composed mostly of water, which is highly absorbing in the mid-IR spectrum. There is a growing body of evidence suggesting that by tuning the laser wavelength to protein absorption bands in this region, most notably the amide II absorption band of protein at $\lambda = 6.45 \mu\text{m}$, soft tissues can be ablated with minimal collateral damage and excellent clinical outcome [1–4]. Several models have been proposed to account for these observations [1, 5, 6] but none of the proposed mechanisms account for the unique pulse characteristics of the FEL. The FEL pulse consists of an $\approx 5 \mu\text{s}$ macropulse which contains a 3 GHz train of 1 ps micropulses. This type of structure has the possibility of producing large amplitude stress waves within the tissue, however they are of such short duration that recording the effects of the micropulses experimentally is very difficult due to the limited response time of electronic systems.

It has long been known that the absorption coefficient of water is strongly influenced by temperature [7–10]. This temperature dependence has been attributed to the deposited energy density in the absorbing material [11–13]. One result of this strong temperature dependence is that the water absorption band at $\lambda = 3 \mu\text{m}$ is shifted to shorter wavelengths during rapid energy deposition, i.e.—temperature rise. This causes the absorption coefficient of water to increase at wavelengths on the blue side of the peak (shorter wavelengths), and to decrease on the red side (longer wavelengths). As the absorption coefficient depends both spatially and temporally on the energy distribution in the sample, the development of an analytical expression for the resulting temperature profile is generally not possible, which makes an accurate prediction of the results of ablation very complicated.

Numerical modeling was turned to as a technique for investigating soft tissue ablation with the FEL for several reasons. First, it allows the study of processes on time scales not possible with standard experimental techniques. The FEL micropulses are $\approx 1 \text{ ps}$ in duration, with a delay of $\approx 350 \text{ ps}$ between successive pulses, which eliminates the use of electronic transducers and recording equipment to study the effects of the individual micropulses. Second, modeling allows the variation and control of parameters that are otherwise beyond control. The temporal distribution of the FEL pulse can have a large impact on the ablation process, but is not easily manipulated experimentally. With numerical modeling, the time dependent deposition of the laser energy can be altered to probe the effects. Finally, numerical modeling allows the possibility to track dynamic changes in the material, including the absorption coefficient of water, and view their effects.

A numerical code developed at Lawrence Livermore National Laboratory called Kull was used to simulate the ablation of soft tissues with the FEL. Kull is a comprehensive physics simulation package under development, that eventually will include processes of light transport, material, thermal, and mechanical response. It is written in the computer language C++, and wrapped in the interpreted language Python, which provides a user interface to the underlying numerical code. The most novel aspect of the Kull code is that it is fully three-dimensional, and allows the use unstructured meshes of arbitrary polyhedral zones, making no assumptions or restrictions on the type of zone used. These advanced features make the code ideal for modeling the complicated processes involved in tissue ablation.

The goal of this modeling effort is to determine the effects that the micropulse structure and dynamic absorption have on the ablation process. Specifically, the impact that these features have on the ablation threshold will be investigated performing model simulations and comparing the results.

V.2 MODELLING METHODS

In the current study, the material response to laser irradiation is calculated by solving compressible hydrodynamic equations, coupled with an equation of state for the material. The hydrodynamic response of the material is calculated using the standard equations for the conservation of mass, momentum and energy:

$$\frac{\partial \rho}{\partial t} = -\rho \vec{\nabla} \cdot \vec{v}, \quad (\text{V.1})$$

$$\frac{\partial \rho v^k}{\partial t} = -\frac{\partial P}{\partial x^k} - \rho v^k \vec{\nabla} \cdot \vec{v} + \rho \vec{g}_k, \quad (\text{V.2})$$

$$\frac{\partial \rho \varepsilon}{\partial t} = -P \vec{\nabla} \cdot \vec{v} - \rho \varepsilon \vec{\nabla} \cdot \vec{v}. \quad (\text{V.3})$$

An equation of state for water was used to model soft tissues. The equation chosen allows the existence of negative pressure, or tensile stress, that is often seen during laser irradiation of materials with a free boundary. Modeling soft tissues with water can be a good approximation when considering the optical and thermal properties of tissue [14]. In the mid-IR spectrum, water is the primary chromophore of most soft tissues, typically accounting for 70% or more of the tissue mass. There are however some protein absorption bands, most notably at wavelengths such as $\lambda = 6.1$ and $6.45 \mu\text{m}$, where the amide bonds in protein exhibit reasonable absorption [1, 15]. For the current study however, we assume that water is the dominant chromophore, and is responsible for the thermodynamic response of the tissue.

A one-dimensional geometry is used throughout the simulations. This is a reasonable approximation for laser irradiation in the IR spectrum, since the penetration depth of the laser radiation is typically small compared to laser spot size. The numerical mesh is constructed as a linear strip of 2000 square zones, $0.1 \mu\text{m}$ on each side, for a total mesh depth of $200 \mu\text{m}$. This zoning scheme was chosen so that there would be > 100 zones per acoustic wavelength. Motion of the mesh is fixed in the transverse direction to maintain one-dimensional propagation, and the surface boundary is free to move with a boundary condition of atmospheric pressure outside the mesh.

V.2.1 Laser Irradiation

The laser irradiation was modeled by a time-dependent energy source that is delivered to the surface of the mesh. It is assumed that the incident laser radiation is absorbed and converted to thermal energy instantaneously, since it is assumed that the absorption process occurs on time scale much shorter than the pulse duration. Two types of laser pulses were used to investigate the effect of pulse structure on the ablation dynamics. The first is a pulse-train delivery that is similar to the actual FEL pulse, where a high frequency train of instantaneously absorbed pulses is delivered with a delay of $t_d = 0.35 \text{ ns}$ between them. The second pulse type is a constant-power pulse of the same duration and radiant exposure as the pulse-train. The pulse duration for both pulse types was limited to $t_p = 50 \text{ ns}$ in the interest of computational time. The simulations were run by fixing the radiant exposure at $H = 5.0 \text{ J/cm}^2$, and varying the absorption coefficient $200 \leq \mu_a \leq 10,000 \text{ cm}^{-1}$ for both pulse types. This range of absorption coefficients should produce results both below and above the threshold for ablation. From the simulation results, the surface velocity of the mesh was plotted as a function of time to determine the ablation onset time $t_{\text{abl}}(\text{ns})$, from which the ablation threshold $H_{\text{th}}(\text{J/cm}^2)$ can be calculated according to

$$H_{\text{th}} = t_{\text{abl}} \cdot L, \quad (\text{V.4})$$

where L (W/cm^2) is the laser pulse irradiance.

A shorter duration pulse $t_p = 50 \text{ ns}$ is used to model the actual FEL pulse for most of the simulations in order to decrease the computational time. To determine if this simplification is valid, a limited set of simulations was run investigating the effect of pulse duration on the ablation dynamics. For these simulations, a pulse-train delivery was used with a micropulse delay of $t_d = 0.35 \text{ ns}$, a fixed radiant exposure of $H = 0.2 \text{ J/cm}^2$, and a static absorption coefficient of $\mu_a = 13,300 \text{ cm}^{-1}$. The pulse duration was varied between $50 \leq t_p \leq 1000 \text{ ns}$,

and the ablation onset time was measured to determine if the ablation dynamics from the short pulse simulations could be extrapolated to longer times.

V.2.2 Absorption Model

The effect of dynamic absorption was investigated by comparing the ablation dynamics that result from a pulse-train irradiation using two different absorption models. For both models, a Beer's law absorption profile is used to determine the energy distribution on a zone-by-zone basis according to

$$E_{\text{sp}} = \frac{1}{\rho} \mu_a H \exp[-\mu_a x], \quad (\text{V.5})$$

where E_{sp} (J/g) is the specific energy, ρ (g/cm³) is the density, μ_a cm⁻¹ is the local absorption coefficient, H is the incident radiant exposure, and x (cm) is the mesh depth.

In the first absorption model, a static absorption coefficient is used in Eq. (V.5) to calculate the energy distribution. In this case, local absorption coefficient is calculated by

$$\mu_a = \mu_{a,0} \frac{\rho}{\rho_0}, \quad (\text{V.6})$$

where $\mu_{a,0} = 13,300$ cm⁻¹ is the room-temperature, low-intensity absorption coefficient [13], and ρ_0 is the initial density of the mesh. The local absorption coefficient is scaled by the change in density in order to more accurately reflect the changes in the absorption properties during rapid heating and phase changes.

The second absorption model, initially proposed by Shori et al. [13], models water as a dynamic saturable absorber according to

$$\mu_a = \frac{\mu_{a,0}}{1 + \frac{E/V_{\text{ab}}}{E/V_{\text{sat}}}}, \quad (\text{V.7})$$

where E/V_{ab} (J/cm³) is the local energy absorbed per volume, and E/V_{sat} (J/cm³) is the saturation energy per volume. It has been experimentally determined that $E/V_{\text{sat}} = 450$ J/cm³ for water at $\lambda = 2.94$ μm [13].

V.3 SIMULATION RESULTS

V.3.1 Ablation Time

The surface zone velocity was used as our marker for determining the ablation onset time. This is based on an empirical observation from previous simulations that the velocity and density of the surface zone change drastically at the apparent ablation threshold. Figure V.1 shows typical traces of the surface zone velocity during irradiation with a constant-power pulse of duration $t_p = 50$ ns, and radiant exposure $H = 5.0$ J/cm² for several absorption coefficients. In Figure V.1a, the surface velocity increases as the material expands during irradiation, but relaxes back toward its resting position once the irradiation ceases, characteristic of the standard model of thermoelastic expansion. In Figure V.1b, the velocity of the surface zone does not relax after the irradiation stops, but continues to move away from mesh. Hence, the surface zone has been ejected from the rest of the mesh, and ablation has occurred. The time at which the surface zone acceleration is at a maximum is taken as the ablation onset time, and in Figure V.1b, we can see that this occurs earlier into the laser pulse for increasing values of the absorption coefficient.

V.3.2 Effect of Pulse Structure

The effect of the pulse structure was investigated by comparing the results of irradiation using a constant-power pulse and a pulse-train delivery at a given radiant exposure. Typical simulation results are shown in Figure V.2, where both the pulse-train (a) and constant-power (b) pulses were delivered at a radiant exposure of $H = 5.0$ J/cm², with a static absorption coefficient of $\mu_a = 200$ cm⁻¹. Comparing the two pulse types, there is a slight modulation of the pressure profile for the pulse-train delivery. This is more apparent in Figure V.3 which is a smaller scale view of the pressure near the surface at $t = 10$ ns. The modulation of the pressure profile for the pulse-train delivery (Figure V.3a) is due to the individual micropulses, which is not seen for the constant-power pulse. However, there is a minor oscillation seen in the constant-power pulse at the high magnification of Figure V.3b, which is due to tiny fluctuations in the incident radiant exposure resulting from the variable time-step in the simulations.

The ablation threshold was read from the surface velocity data for both types of pulses and plotted as a function of the static absorption coefficient. In Figure V.4, we see that the extracted ablation thresholds for the pulse-train and constant-power pulses are nearly

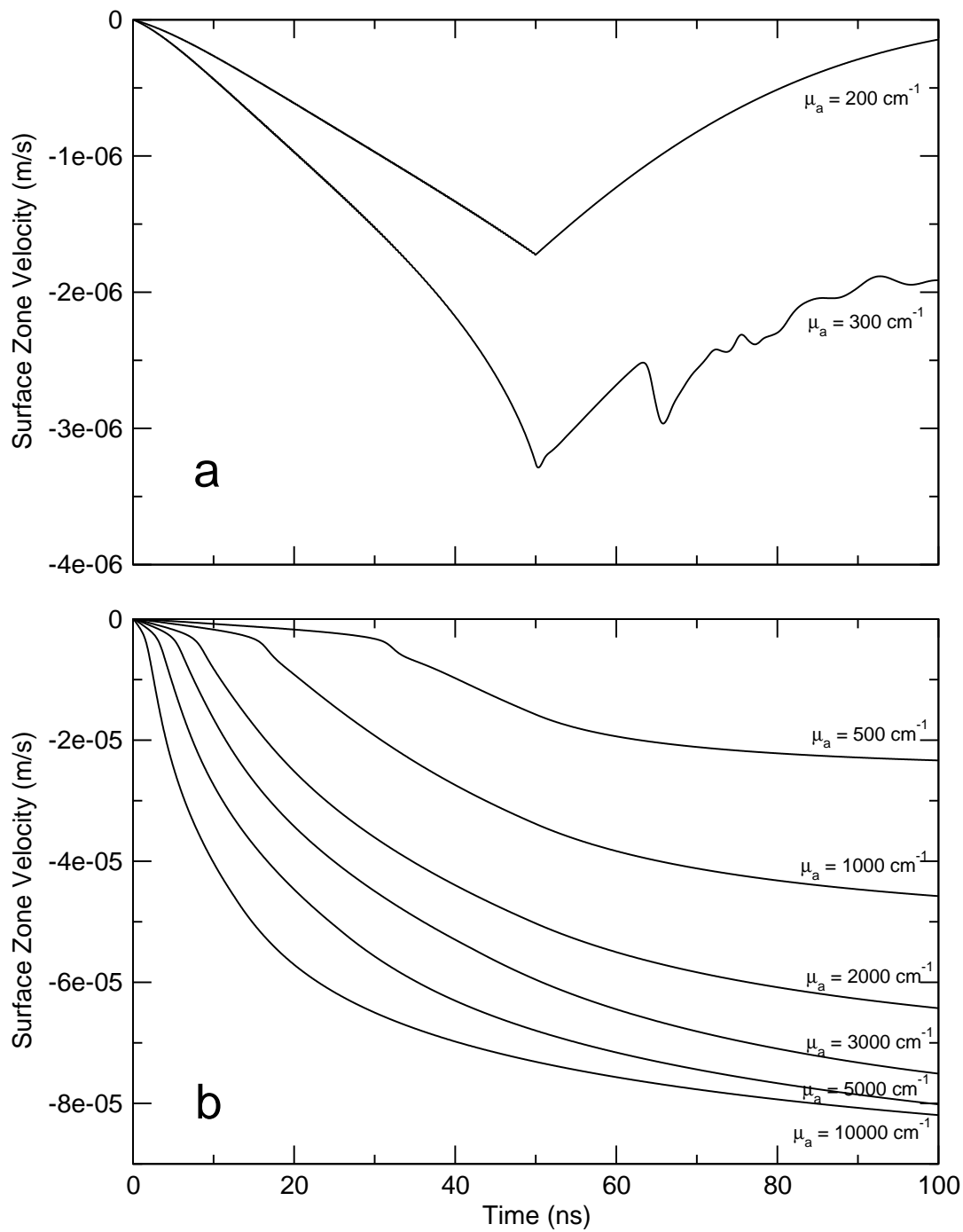


Figure V.1: Ablation time. The velocity of the surface zone is plotted as a function of time for a constant-power pulse with $t_p = 50$ ns and $H = 5.0$ J/cm². In (a), the velocity increases during the laser pulse, but then relaxes after irradiation stops indicating that ablation has not occurred. In (b), the velocity increases drastically at the ablation onset time, which occurs earlier into the pulse for increasing values of the absorption coefficient.

identical. These results were fit to a theoretical model of the predicted ablation threshold,

$$H_{\text{th}} = \frac{1}{\mu_a} W_{\text{abl}}, \quad (\text{V.8})$$

where W_{abl} (J/cm^3) is the heat of ablation. By fitting this model to the data, we find that $W_{\text{abl}} = 1569 \text{ J}/\text{cm}^3$ for the pulse-train delivery and $W_{\text{abl}} = 1573 \text{ J}/\text{cm}^3$ for the constant-power pulse.

V.3.3 *Effect of Dynamic Absorption*

The role of dynamic absorption in the ablation process was investigated by comparing a standard static Beer's law absorption model with a dynamic saturable absorption model [13]. Figure V.5 shows the effect of dynamic absorption on the instantaneous absorption coefficient. In each plot, the absorption coefficient is plotted as a function of the mesh depth at time intervals of $t = 10, 20, 30, 40, 50$ ns for a $t_p = 50$ ns, using both absorption models at a radiant exposure $H = 0.1 \text{ J}/\text{cm}^2$, which is below the threshold for ablation. For the static absorption case, early into the laser pulse the absorption coefficient is nearly constant, but as more laser energy is delivered the absorption coefficient decreases near the surface due to the decrease in density, resulting from the rapid thermal expansion during the laser pulse. For the dynamic absorption case, we see that the absorption coefficient decreases significantly throughout the laser pulse, to become nearly a factor of 2 smaller than the static absorption case for subthreshold radiant exposures.

The ablation threshold was measured as a function of the radiant exposure for the static and dynamic absorption cases. In Figure V.6, we see that the ablation threshold is nearly constant for increasing radiant exposures for both the static and dynamic absorption, and the threshold is ≈ 2.5 times larger for the dynamic absorption.

V.3.4 *Effect of Pulse Duration*

Modeling the FEL pulse ($t_p = 5 \mu\text{s}$) with a pulse of only 50 ns allows considerable computational simplification. To test the validity of this simplification, we ran simulations using the pulse-train delivery with static absorption ($\mu_a = 13,300 \text{ cm}^{-1}$) at a fixed radiant exposure ($H = 0.2 \text{ J}/\text{cm}^2$) for pulse durations of $t_p = 50, 100, 200, 500, 1000$ ns. The results are shown in Figure V.7, where the surface zone velocity is plotted against the normalized ablation time, $\tau = t_{\text{abl}}/t_p$. From this plot we see that the ablation onset time, relative to the pulse duration, is nearly the same for all pulse durations tested. The normalized ablation

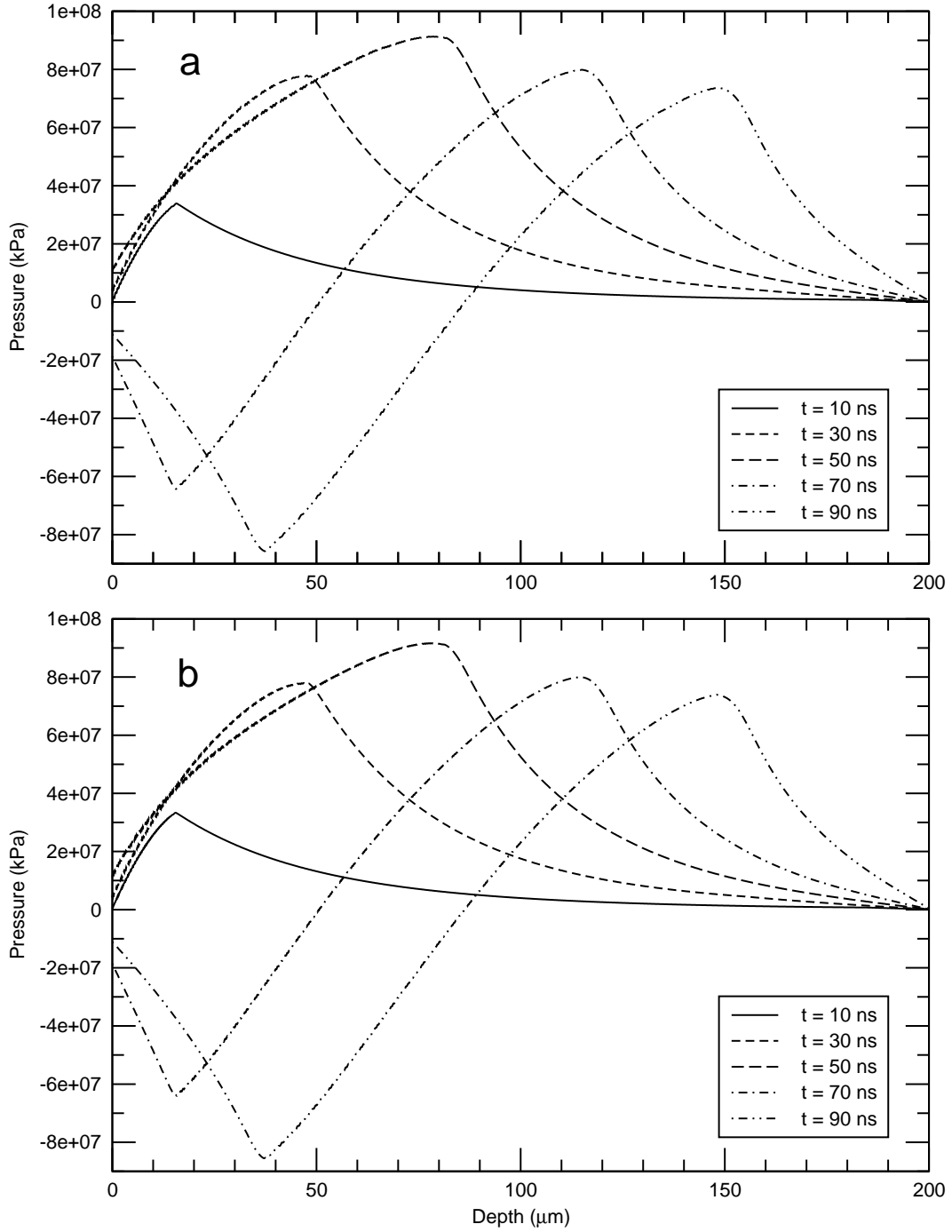


Figure V.2: Pressure profile in the mesh during laser irradiation. Pulse-train (a) and constant-power pulses (b) were delivered at a radiant exposure of $H = 5 \text{ J/cm}^2$ and with a static absorption coefficient of $\mu_a = 200 \text{ cm}^{-1}$.

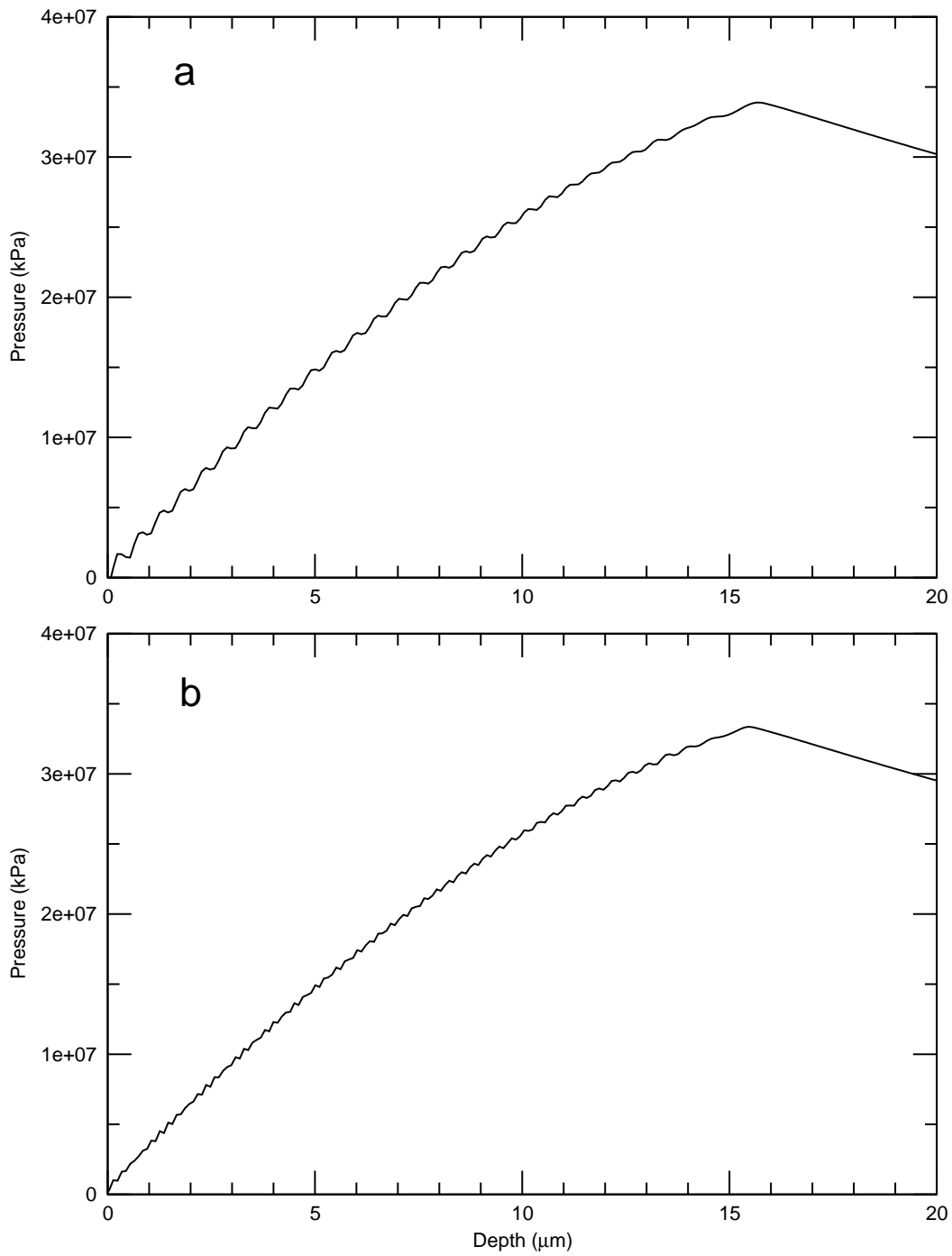


Figure V.3: Expanded view of the pressure profile near the surface. Pulse-train (a) and constant-power pulses (b) were delivered at a radiant exposure of $H = 5 \text{ J/cm}^2$ and with a static absorption coefficient of $\mu_a = 200 \text{ cm}^{-1}$.

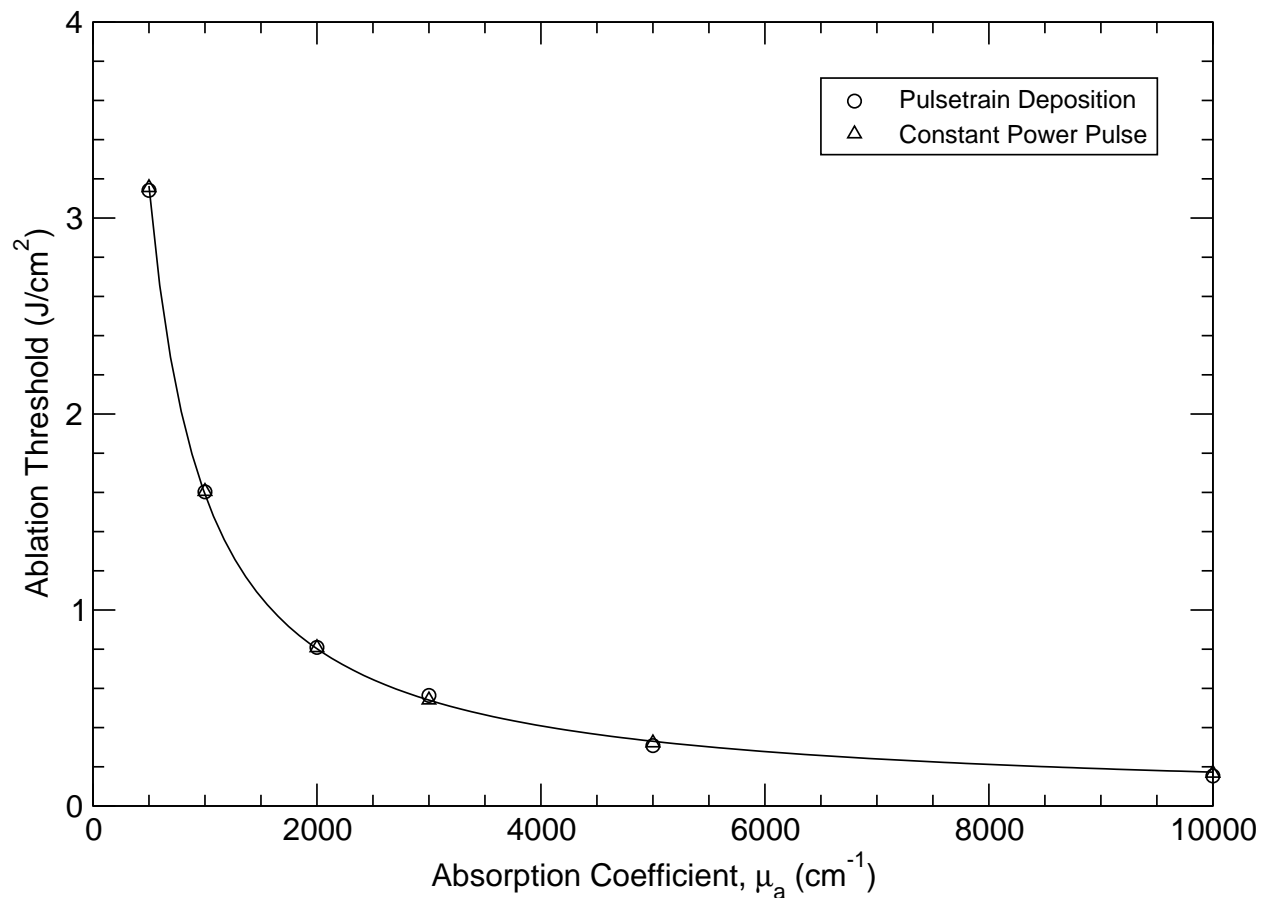


Figure V.4: Effect of pulse structure on the ablation threshold. The ablation threshold extracted from the pulse-train and constant-power pulse depositions are plotted as a function of the absorption coefficient for a radiant exposure of $H = 5 \text{ J}/\text{cm}^2$. The data points were fit to a theoretical model of the ablation threshold which was used to calculate the heat of ablation.

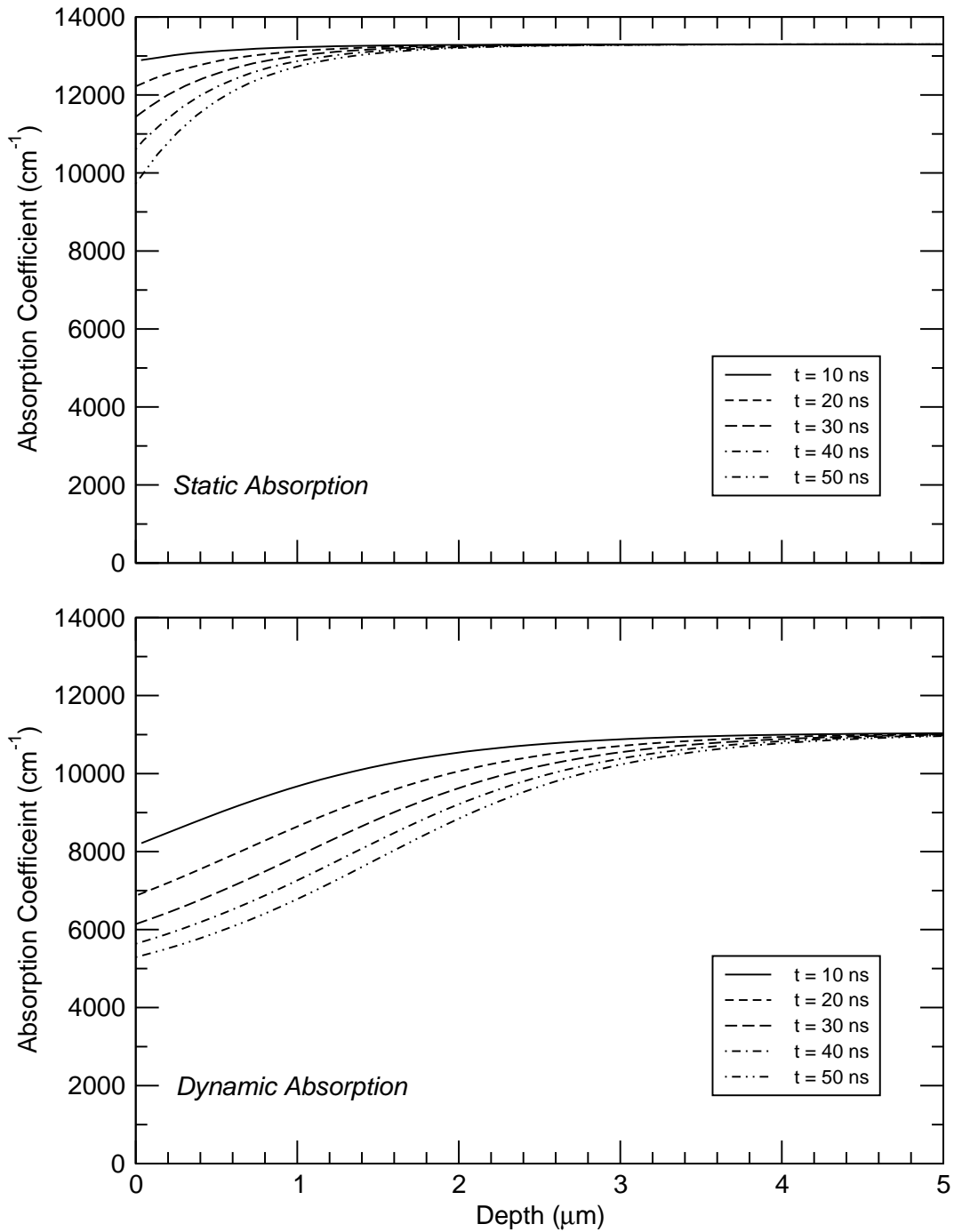


Figure V.5: Absorption coefficient as a function of mesh depth for both static and dynamic absorption at several times during the laser pulse.

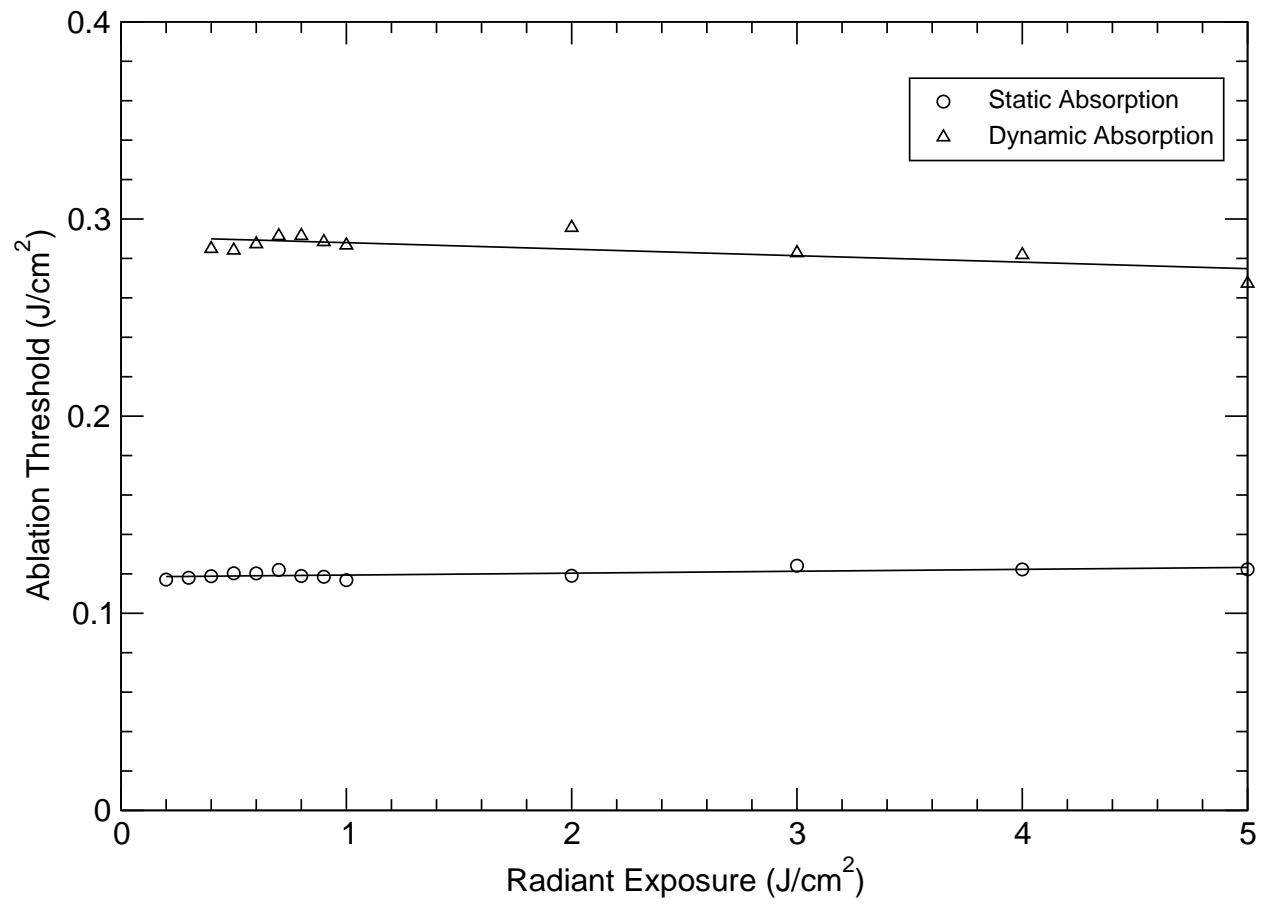


Figure V.6: Effect of dynamic absorption on the ablation threshold. The ablation threshold is plotted as a function of the radiant exposure for the static and dynamic absorption cases.

onset time for the parameters used is $\tau = 0.57$, that is, ablation begins when 57% of the laser pulse has been delivered. An interesting feature of the traces in Figure V.7 are the fluctuations that occur near the ablation threshold for longer duration pulses, namely $t_p = 50$ and 1000 ns. These fluctuations occur just prior the onset of ablation and could be due to relatively large motion occurring below the surface that takes time to reach the surface.

The absolute ablation time was plotted as a function of the laser pulse duration in Figure V.8. From this plot we can see that the ablation time does increase linearly with the pulse duration, indicating that ablation begins when a fixed radiant exposure has been supplied to the sample, regardless of the pulse duration.

V.4 DISCUSSION

V.4.1 Pulse Structure

According to the simulation results in Figures V.2 and V.3, the high frequency, short duration micropulses from the FEL do not exert a strong effect on the stress profiles that are produced in the mesh during irradiation. This is primarily because the radiant exposure that is delivered by a single micropulse is not sufficient to generate a large amplitude response by itself. Since the small amplitude impulses are delivered at a very high frequency, there is not enough time between micropulses for significant stress relaxation to occur, so the pressure build-up from the pulse-train is cumulative in a manner that is similar to the delivery of a constant-power pulse. This is seen by comparing the rising pressure profile during the pulse-train delivery (Figure V.3a) to the constant-power pulse (Figure V.3b). A slight modulation of the pressure profile of the constant-power pulse is visible on a small scale, but this is most likely due to numerical noise in the computation, rather than the irradiation conditions.

The minimal role of the pulse structure on the ablation dynamics is demonstrated by the lack of any significant difference in the ablation threshold for the two pulse types (Figure V.4). It has been postulated that the pressure transients generated by the micropulse structure of the FEL might alter the ablation dynamics by changing the temperature rise that is necessary to begin vaporizing water [16]. If this were true, we would expect the ablation onset time to reflect these dynamic changes, and therefore be manifest in the ablation threshold. However, we do not see any difference in the apparent threshold for the two pulse types, and must conclude that the micropulse structure, by itself, does not impact the ablation dynamics.

The ablation threshold from the simulations was fit to a general ablation model for comparison to previous experimental results. Using Eq. (V.8), the heat of ablation was calculated to be $W_{\text{abl}} = 1570 \text{ J/cm}^3$. This agrees well with experimental measurements,

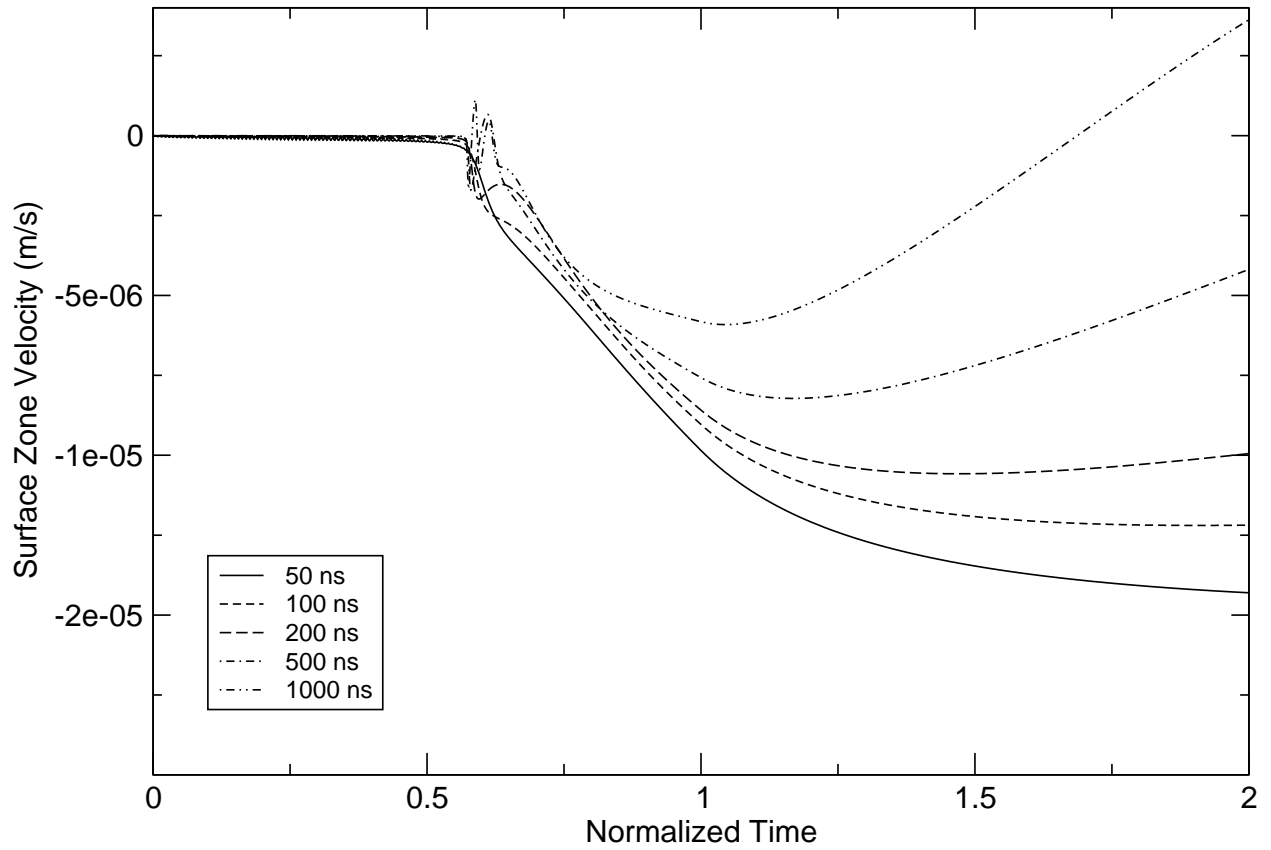


Figure V.7: Normalized ablation time for multiple pulse durations. The normalized time $\tau = t_p/t_{abl}$ shows that the onset of ablation occurs when $\approx 50\%$ of the laser pulse has been delivered at a fixed radiant exposure of $H = 5 \text{ J/cm}^2$ with a static absorption coefficient of $\mu_a = 13,300 \text{ cm}^{-1}$.

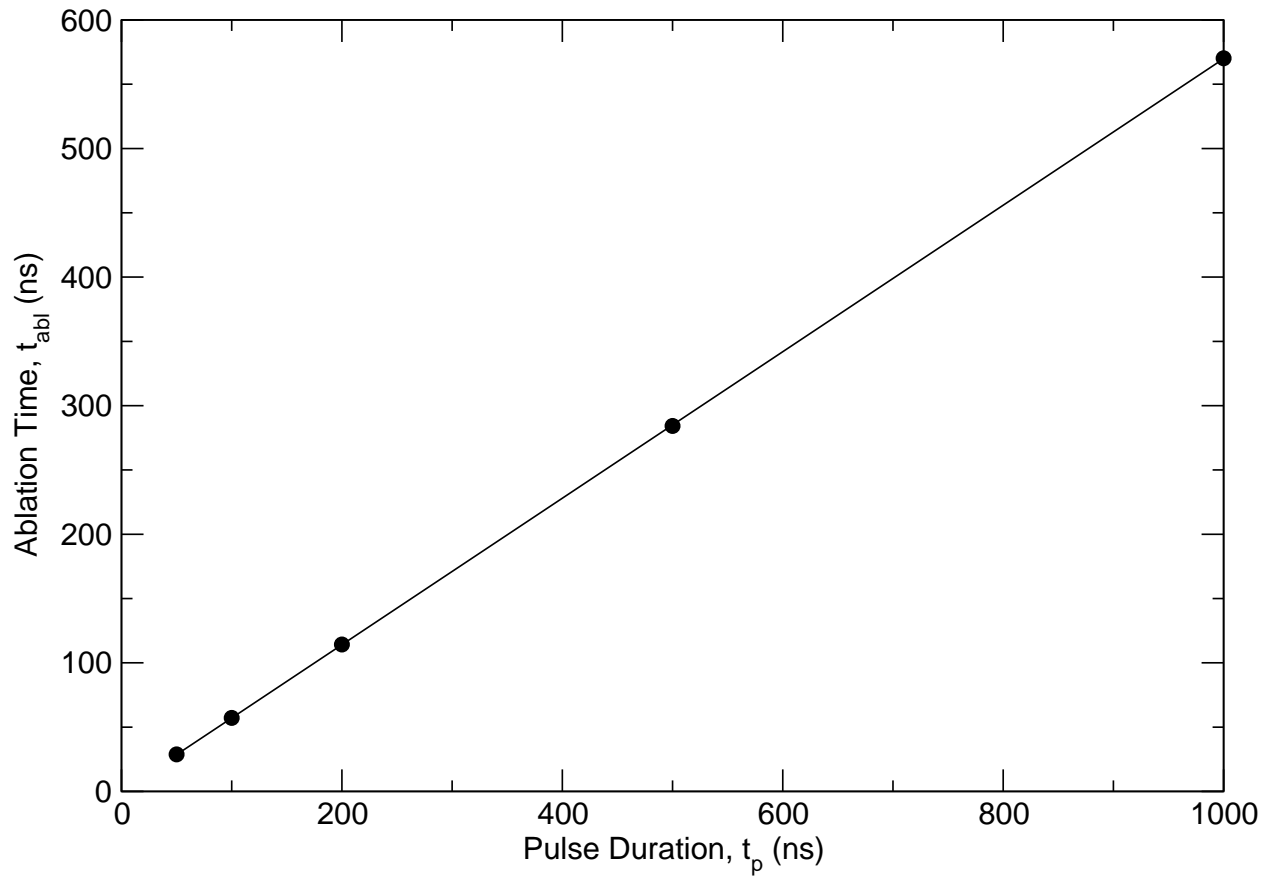


Figure V.8: Effect of pulse duration. The ablation time is plotted against laser pulse duration for a fixed radiant exposure of $H = 5 \text{ J/cm}^2$ and with a static absorption coefficient of $\mu_a = 13,300 \text{ cm}^{-1}$.

where the ablation depth in rat dermis was measured over a broad range of wavelengths using the FEL [16]. The results of the measurements were fit to a steady-state ablation model that predicted a heat of ablation of $W_{\text{abl}} = 1507 \text{ J/cm}^3$.

V.4.2 Dynamic Absorption

The simulation results of the ablation threshold of water for both static and dynamic absorption models reveal two interesting observations. First, the ablation threshold is constant as a function of radiant exposure for both absorption models. Second, the threshold is a factor of 2.5 times larger when considering dynamic, rather than static absorption. Both of these observations can be explained when we consider that the dynamic saturable absorption model of water simply decreases the local absorption coefficient during the irradiation. The effect that this has is to increase the amount of deposited energy that is required to supply the heat of ablation. From a thermodynamic viewpoint, the temperature rise that is required to induce a phase change, which drives the ablation process, is not influenced by the absorption coefficient of the material. Therefore, the dynamic changes in the absorption coefficient only require an increased amount of energy to effect the same temperature rise that is required by static absorption.

V.5 CONCLUSIONS

A developmental set of numerical codes has been used to model FEL ablation of soft tissue. The effects of the FEL micropulse structure and the dynamic absorption of water on the ablation threshold were investigated. Within the constraints of the model, it was found that the FEL micropulse structure exerted no significant effect on the observed ablation threshold. But, it was found that the dynamic absorption of water may increase the ablation threshold by as much as a factor of 2.5.

ACKNOWLEDGEMENTS

This work was performed under the auspices of the U.S. Department of Energy by Lawrence Livermore National Laboratory under contract no. W-7405-Eng-48. I would also like to acknowledge Anthony Makarewicz and the Kull development team at LLNL for much assistance with the Kull code.

REFERENCES

- [1] Edwards G, Logan R, Copeland M, Reinisch L, Davidson J, Johnson B, Maciunas R, Mendenhall M, Ossoff R, Tribble J, Werkhaven J, O'Day D, "Tissue ablation by a free-electron laser tuned to the amide II band," *Nature*, 371:416–419, 1994.
- [2] Auerhammer JM, Walker R, van der Meer AFG, Jean B, "Dynamic behavior of photobleaching products of corneal tissue in the mid-IR: A study with FELIX," *Applied Physics B: Lasers and Optics*, 68:111–119, 1999.
- [3] Joos KM, Shen JH, Shetlar DJ, Casagrande VA, "Optic nerve sheath fenestration with a novel wavelength produced by the free-electron laser FEL," *Lasers Surg. Med.*, 27:191–205, 2000.
- [4] Copeland ML, Cram G, Gabella B, Jansen ED, Mongin JD, Pratisto HS, Uhlhorn SR, Edwards GS, "First human application of a free-electron laser," *Lancet*, submitted.
- [5] Tribble J, Lamb DC, Reinisch L, Edwards G, "Dynamics of gelatin ablation due to free-electron laser irradiation," *Phys. Rev. E*, 55:7385–7389, 1997.
- [6] Edwards GS, Hutson MS, Hauger S, "Heat diffusion and chemical kinetics in Mark-III fel tissue ablation," in *Commercial and Biomedical Applications of Ultrafast and Free-Electron Lasers*, Edwards GS, Neev J, Ostendorf A, Sutherland JC, eds., vol. 4633, pp. 184–193, SPIE, Bellingham, WA, USA, 2002.
- [7] Collins JR, "Changes in the infra-red absorption spectrum of water with temperature," *Physical Review*, pp. 771–779, 1925.
- [8] Hale GM, Query MR, Rusk AN, Williams D, "Influence of temperature on the spectrum of water," *Journal of the Optical Society of America*, 62(9):1103–1108, 1972.
- [9] Falk M, Ford TA, "Infrared spectrum and structure of liquid water," *Canadian Journal of Chemistry*, 44:1699–1707, 1966.
- [10] Pinkley LW, Sethna PP, Williams D, "Optical constants of water in the infrared: Influence of temperature," *Journal of the Optical Society of America*, 67(4):494–499, 1977.
- [11] Vodopyanov KL, "Saturation studies of H₂O and HDO near 3400 cm⁻¹ using intense picosecond laser pulses," *Journal of Chemical Physics*, 94(8):5389–5393, 1991.
- [12] Walsh JT, Cummings JP, "Effect of the dynamic optical properties of water on mid-infrared laser ablation," *Laser in Surgery and Medicine*, 15:295–305, 1994.

- [13] Shori RK, Walston AA, Stafsudd OM, Fried D, Walsh JT, “Quantification and modeling of the dynamic changes in the absorption coefficient of water at $\lambda = 2.94\mu\text{m}$,” *IEEE Journal of Selected Topics in Quantum Electronics*, 7(6):959–970, 2001.
- [14] Welch AJ, van Gemert MJC, eds., *Optical-Thermal Response of Laser-Irradiated Tissue*, chap. 21, pp. 709–763, Plenum Press, New York, 1995.
- [15] Yannas IV, “Collagen and gelatin in the solid state,” *Journal of Macromolecular Science—Reviews in Macromolecular Chemistry*, C7(1):49–104, 1972.
- [16] Uhlhorn SR, Mackanos MA, Jansen ED, “Free electron laser ablation of soft tissue: Measurement of ablation depth and threshold,” *Lasers in Surgery and Medicine*, 2001.

CHAPTER VI

CONCLUDING REMARKS

VI.1 SUMMARY

The manuscripts presented in this dissertation represent a collection of work that was aimed to investigate the mechanisms involved in soft tissue ablation with a FEL. Several techniques were used in the investigations in order to view the processes involved from different perspectives, ranging from an integrative viewpoint studying the gross effects of the ablation process over a wide range of parameters, to a detailed view studying the dynamics of the processes under a small set of conditions.

From an integrative viewpoint, chapter III described the results of the analysis of ablation craters produced in rat dermis over a wide range of mid-IR wavelengths produced with the FEL. The results of the analysis were compared to steady-state ablation models that predict the ablation depth based primarily on the optical properties of the tissue. Several important results were revealed in this study. First, the ablation process can be described by a steady-state model over a broad range of wavelengths and tissue absorption coefficients. This is further supported by the fact that the ablation crater depth decreased for wavelengths with a large absorption coefficient. This was attributed to attenuation of the incident beam by ablation debris ejected during the laser pulse. Second, to a first approximation, the ablation of soft tissue with the FEL is a water absorption dominated process. This is demonstrated by the analysis of both the ablation threshold and ablation depth, where the measured data fit theoretical models for both, assuming the optical and thermal properties of water to be representative of soft tissue. Furthermore, much of the data that did not directly fit the theoretical predictions could be explained when we considered the dynamic absorption properties of water. Finally, wavelengths where protein absorption represented a significant percentage of the total absorption cross section, namely $\lambda = 6.1$ and $6.45 \mu\text{m}$, were not consistent with wavelengths where water was the dominant chromophore, that is, the data from $\lambda = 6.1$ and $6.45 \mu\text{m}$ did not fall on the curves predicting the ablation threshold and ablation depth, and could not be explained by any of the previous arguments. This suggested an important role for protein absorption during ablation of soft tissues, which is consistent with the results of several studies, and warranted further investigation.

Taking a more detailed view of the ablation process, chapter IV investigated the ablation dynamics by measuring the peak pressures generated during FEL irradiation of dermal

tissue, and comparing the results to theoretical models in order to gain insight into the role of protein absorption in mid-IR ablation. The experiments were carried out at two wavelengths: $\lambda = 3.3 \mu\text{m}$, for which water is the dominant chromophore in soft tissue, and $\lambda = 6.45 \mu\text{m}$, for which protein is the dominant chromophore. Additionally, two samples with similar absorption characteristics, but different material properties were studied: rat dermis, which has protein distributed in the structural matrix of the tissue, and gelatin, which has protein distributed in small fragments and globular structures that are not capable of supporting significant stresses. Two important results were found in this study. First, the ablation dynamics were governed by a steady-state, surface mediated process, regardless of the chromophore. This was demonstrated by the fact that the surface vaporization model fit the data for the peak pressure recorded in the ablation plume for both wavelengths and both samples. This result is consistent with those from chapter III which showed that FEL ablation of soft tissue can be described by a steady-state model over a broad range of wavelengths. A possible explanation for chromophore independence is that the FEL micropulse structure enhances the surface mediated effect by only removing a fine layer of tissue with each micropulse once the heat of ablation has been supplied. Second, for $\lambda = 6.45 \mu\text{m}$ irradiation, where protein absorption is strong, there is a significant decrease in the ablation threshold of rat dermis, relative to that of gelatin, that is not seen at $\lambda = 3.3 \mu\text{m}$ where there is effectively no protein absorption. This suggests that the mechanical strength of the tissue is being compromised by the targeted destruction of the structural matrix, since in the gelatin samples the protein is distributed in small fragments and globular structures that are not capable of supporting stress. This result is consistent with both previous observations of FEL ablation at $\lambda = 6.45 \mu\text{m}$, and those of UV ablation of soft tissues, where protein in the structural matrix is the chromophore.

Finally, chapter V presents the results of numerical simulations that were performed to further investigate some of the effects that were observed in the experiments, namely the dynamic absorption of water and the effect of the FEL micropulse structure. The simulations were performed by calculating the hydrodynamic response of a sample, coupled with an equation of state for the material that was irradiated with a time dependent energy source. Soft tissues were modeled with liquid water which is a good approximation for the optical and thermal properties. The simulations revealed several interesting points. First, comparing a pulse train delivery with a constant power pulse of equivalent radiant exposure showed no difference in the ablation threshold. This does not support an explanation that was proposed in chapter III for the artificially low heat of ablation. It was postulated that the micropulses could generate large tensile stresses that would decrease the temperature rise that was necessary for material ejection to occur. While the simulation results appear to

eliminate this possibility, they do not show that the micropulse structure has no effect on the ablation mechanics. Specifically, the model does not incorporate mechanical properties, such as the tissue material strength, that might be affected by the micropulses. Second, the simulations showed that dynamic absorption has a strong effect on the ablation threshold, increasing it by as much as a factor of 2.5 at $\lambda = 2.94 \mu\text{m}$. This supports the results presented in chapter III, which attributed much of the error in the ablation depth data to the dynamic absorption characteristics of water.

By viewing the results of the studies together, several conclusions can be drawn about the mechanics of soft tissue ablation with the FEL:

1. The ablation process is steady-state in nature. This fact is supported by all of the experiments, as well as the model simulations, and is primarily due to the macropulse duration, which is longer than the requirement for a blow-off situation, but is still short enough to remain thermally confined.
2. The ablation process is surface mediated in nature, regardless of the chromophore. The most plausible explanation for this is the micropulse structure, which may enhance this effect by removing a very fine layer of tissue for each micropulse, once the heat of ablation has been supplied.
3. Dynamic absorption of water plays a significant role. The ablation depth and threshold data support this from a qualitative standpoint, and the model simulation results suggest that the ablation threshold may be increased by as much as a factor of 2.5 at $\lambda = 2.94 \mu\text{m}$.
4. Protein absorption results in the targeted destruction of the tissue structural matrix at wavelengths where the absorption by protein represents a significant fraction of the overall absorption cross section, primarily $\lambda = 6.45 \mu\text{m}$. This is demonstrated by the significant decrease in the ablation threshold for dermal tissue, relative to that from gelatin. This is attributed to denaturation of the protein in the tissue matrix which compromises the mechanical strength of the tissue.

While the results presented in this work represent a significant contribution to the body of knowledge regarding soft tissue ablation with the FEL, further work is required to lend more support to these findings and determine other processes that may play a role.

VI.2 FUTURE DIRECTIONS

One area of the research where further work is warranted are the acoustic measurements presented in chapter IV. Previous studies that have used this technique to measure ablation dynamics most often used thin film piezoelectric transducers to measure the acoustic stresses that propagate in the tissue. Furthermore, thin tissue samples are used for the irradiation to ensure that the signals detected are in the acoustic near-field. For the experiments presented in this work, the acoustic pressure wave that propagates in air is detected with a piezoelectric microphone. While it is argued that this signal is representative of the peak pressure in the expanding vapor plume, it is acknowledged that these signals are in the acoustic far-field, where other effects including acoustic and geometric attenuation may play a role. A thorough investigation correlating the near-field acoustic stresses in the tissue to the far-field acoustic pressure in the surrounding air would give valuable insight into the dynamics involved in these regions during material ejection.

The numerical modeling results presented in chapter V represent a solid foundation upon which significant development can be made. In the simulations, soft tissue was modeled using an equation of state for liquid water. This is a good approximation when considering the optical and thermal properties of tissue, but not when mechanical effects such as the material strength are involved. Recently, improvements in the numerical codes have included the ability to incorporate the effect of material strength into the model. Coupled with a modified equation of state, processes such as the targeted destruction of the tissue structural matrix can be investigated. In the model of explosive vaporization of tissue, material ejection is thought to commence when the pressure in an expanding subsurface water vapor bubble exceeds the strength of the structural matrix. By incorporating these effects into the ablation model, the contribution of explosive processes that are typical of mid-IR ablation with other sources, can be studied for FEL ablation.

APPENDIX A

BEAM DELIVERY OF THE VANDERBILT FREE ELECTRON LASER WITH HOLLOW WAVE
GUIDES: EFFECT ON TEMPORAL AND SPATIAL PULSE PROPAGATION

Hans S. Pratisto, Stephen R. Uhlhorn
and E. Duco Jansen

Department of Biomedical Engineering
Vanderbilt University
Nashville, TN, USA

Published in
Fiber and Integrated Optics **20**:83–94, 2001.

ABSTRACT

Hollow Wave Guides were evaluated as a beam delivery system for the Free Electron Laser (FEL) at Vanderbilt in preparation of surgical applications. They can transmit the mid-infrared wavelength range ($2\ \mu\text{m} - 9\ \mu\text{m}$) and tolerate the high peak intensity ($> 10^{14}\ \text{W}/\text{m}^2$) in the micropulse of the FEL. Changes in the temporal and spatial beam characteristics induced by the transmission through 1.5 meter Hollow Wave Guides with bore radii of $250\ \mu\text{m}$ and $530\ \mu\text{m}$ were investigated. Temporal broadening of the micro pulses was studied using intensity autocorrelation measurements and beam profile measurements were performed with a pyroelectric camera. Results demonstrate significant pulse broadening and development of higher order modes induced by sub-optimal coupling of the beam into the Hollow Wave Guide. Bending of the Hollow Wave Guide induced additional losses and reduced propagation of higher modes responsible for broadening the pulse. Calculations with a geometrical ray model support the findings on pulse broadening. Optimal coupling conditions are extremely critical for maximal transmission performance of the Hollow Wave Guide. Design consequences for a FEL delivery system are discussed.

A.1 INTRODUCTION

The Free Electron Laser (FEL) at Vanderbilt University has a wavelength tunability range between 2 and 9 μm . In this mid-infrared spectral range, biological tissue shows strong absorption and therefore selected wavelengths are well suited for efficient and precise tissue ablation. Previous studies have demonstrated that the FEL tuned to the amide-II band at 6.45 μm ablates tissue very precisely [1, 2]. Another wavelength of interest is 2.94 μm where water has its main absorption peak. Reasonable transmission of both of these wavelengths with optical fibers is possible: zirconium fluoride or apophire fibers for 2.94 μm and arsenic selenide or chalcogenide fibers for 6.45 μm . However, none of these materials tolerate the peak intensity of up to 10^{14} W/m^2 in the unique pulse structure of the FEL (described in detail in the next section).

Currently, the use of an articulated mirror arm [3] or a Hollow Wave Guide (HWG) appears to be the only alternative for transmitting the FEL pulses to the operation field. The articulated arm, although it is fairly well accepted as a surgical beam delivery device for wavelengths where fiber optics are not amenable (in particular for the CO_2 laser), has severe limitations in surgery with regards to maneuverability and size. The hollow wave guides have reasonable transmission in the mid-IR range, a high damage threshold, and an acceptable flexibility [4–6] but suffer from losses induced by bending.

The aim of this study was to evaluate the performance of the HWGs in view of FEL pulse delivery for surgical applications. Investigations on the micropulse propagation and the beam profile as a function of coupling conditions were performed to study the temporal and spatial alteration of the FEL pulses transmitted through the HWG.

A.2 MATERIALS AND METHODS

A.2.1 *Characteristics of the Vanderbilt Free Electron Laser*

The Free Electron Laser at the Vanderbilt University is a tunable radiation source with a wavelength range between 2 and 9 μm [7]. For this study the laser was tuned to a center wavelength of $\lambda = 2.94 \mu\text{m}$ (3401 cm^{-1}). The spectral width is 0.8% of the center wavelength (25 cm^{-1}) and typically showed a shoulder towards the longer wavelength. The beam is linearly polarized. The FEL operates in a pulsed mode with a pulse repetition rate of 1–30 Hz. One pulse has a unique structure: it consists of a train of $\approx 1 \text{ ps}$ micropulses, separated from one another by 350 ps, together forming a 4 – 5 μs so called “macropulse”. The radiation is directed from the laser cavity of the FEL to the laboratories and the clinical

operating rooms within the FEL Center (distance up to 90 meters) using mirrors placed in an evacuated pipe system. A macropulse energy of around 50 mJ at a wavelength of $2.94\ \mu\text{m}$ can be delivered to the user.

A.2.2 Pulse width and beam profile measurement

A series of measurements were performed using the setup shown in Figure A.1. The hollow wave guides used were obtained from the Fiber Optic Material Program at Rutgers University, Piscataway, NJ. The FEL beam, which has a diameter of 15 mm at a wavelength of $2.94\ \mu\text{m}$, was either focussed into a straight HWG, into a HWG that was bent into two loops (bending radius 9 cm) or was sent directly into the diagnostic setup. For each set of data a separate reference FEL pulse was characterized with its pulse width and beam profile. For all experiments a calcium fluoride (CaF_2) lens with a focal length of $f = 300\ \text{mm}$ and a diameter of 50 mm was used as coupling lens. An aperture placed in front of the coupling lens allowed changing the beam size, (i.e., change the f-number ($f/\#$) of the coupling system) and therefore varying the coupling conditions into the HWG. The diameter of the aperture was either 3, 6, 12 or 15 mm (15 mm corresponds to a totally unblocked beam). The spotsize of the focussed beam was measured with a scanning knife-edge. Silica glass hollow wave guides (length $l = 1.5\ \text{meter}$) with a bore diameter of $250\ \mu\text{m}$ and $530\ \mu\text{m}$ were placed in the setup. The thickness of the silver iodide coating of the HWG is optimized to transmit a wavelength of $2.94\ \mu\text{m}$ with minimal losses [5]. The coupling end of the HWG was placed at the focal plane of the lens and the tilt angle and x-y displacement of the HWG relative to the beam axis were adjusted carefully to maximize for power throughput and beam profile quality. The transmission was measured without the coupling or the collimating lens in the setup and the input energy was measured behind the aperture which blocked part of the beam (i.e., the percentage indicates the losses in the HGW itself). Additionally the polarization state of the beam was analyzed with a polarizer-analyzer-attenuator (PAZ, II-VI, Saxonburg, PA, USA).

The beam exiting the HWG was recollimated with a lens, and directed to the beam profiler (Pyrocam I, Spiricon, North Main Logan, UT, USA) or into an optical autocorrelator setup to measure the micropulse width. Two-photon absorption in germanium (substrate thickness of 5 mm) at $2.94\ \mu\text{m}$ was used as an optical multiplier for the intensity autocorrelation [8]. The FWHM pulse width was calculated considering the optical path length difference in the scanning mirrors and the transmission signal through the two-photon absorber material. The mean and standard deviation was calculated from eight individual pulse width measurements. Pulse dispersion induced in the CaF_2 lens system was determined to

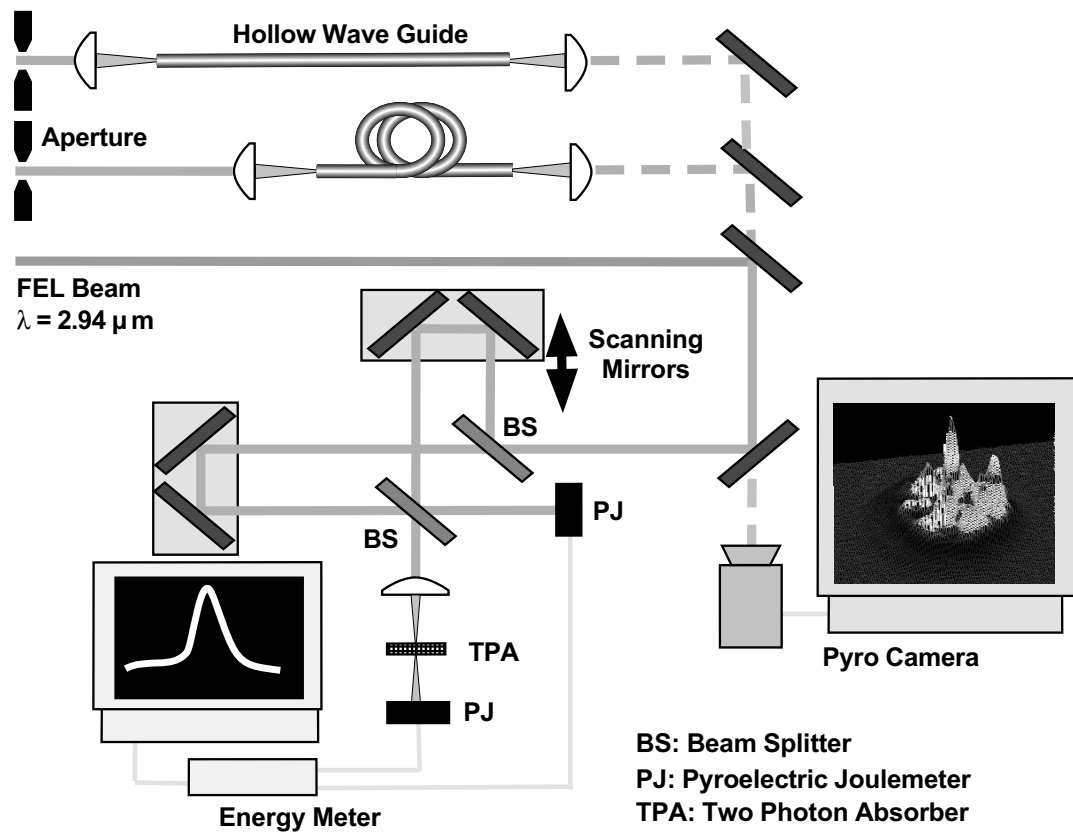


Figure A.1: Setup for beam profile and pulse width measurement.

be negligible (< 0.05 ps) compared to the pulse broadening in the HWG. Beam profiles from the pyroelectric camera were stored on a computer. The resolution of the camera and the algorithm to calculate the beam diameter is only accurate for beam diameters larger than 1 millimeter [9]; therefore the images of the beam profiles were taken out of the focus and are not quantitative. The spotsize diameter of the focussed beam was calculated from the knife-edge measurement [10].

A.3 RESULTS

In Table A.1 an overview of the parameters used to couple the laser beam into the HWG is summarized. The $f/\#$ is given by dividing the aperture diameter by the focal length of the lens ($f = 300$ mm) which was the same for all experiments. The spotsize in the focus was obtained from the knife-edge measurements and the beam profiles were measured several centimeters out of the focus. Refraction at the aperture edge caused the beam shape to change from a clean Gaussian profile (the 15 mm aperture corresponds to the totally unblocked beam) to an almost flat top or even crown shape profile (profiles at an aperture diameter of 3, 6 and 12 mm). The symmetry of the profiles are shown as a two-dimensional (2D) graphs and an intensity profile through the center of this plot illustrates the steep edges of the profiles. The ratio of the measured spotsize and a $250 \mu\text{m}$ or $530 \mu\text{m}$ inner diameter HWG is listed.

Figure A.2 shows the beam profiles and the micropulse width through a $250 \mu\text{m}$ bore size, 1.5 meter straight HWG as a function of the aperture diameter in front of the coupling lens. The alignment of the HWG with respect to the beam axis was carefully adjusted to maintain a low order beam profile. The incident FEL shows a clean Gaussian profile and the autocorrelation of the micropulse reveals a pulse duration of 1.16 ± 0.09 ps (FWHM). The profiles of the beam exiting the HWG show that a main mode propagates through the HWG and for an aperture diameter of 3 and 6 mm the mode is squeezed in one direction. For all the different apertures the micropulse width of the transmitted pulse is maintained within the accuracy of the autocorrelation setup. At an aperture of 3 mm the error bar is the largest because the least amount of energy is available to measure the pulse width.

Figure A.3 shows the beam profiles and the micropulse width through a $250 \mu\text{m}$ bore size, 1.5 meter HWG as a function of the aperture diameter in front of the coupling lens where the HWG was tilted ($\pm 0.9^\circ$) and displaced ($\pm 30 \mu\text{m}$) with respect to the beam axis (thus “misaligning” the system while maintaining the focussed spot on the waveguide and the still matching the acceptance angle of the HWG). The incident FEL shows the clean Gaussian profile and the autocorrelation of the micropulse reveals a pulse duration of 1.18 ± 0.05 ps

(FWHM). The profiles of the beam exiting the HWG show two main modes that propagate. The intensity distribution in the two main modes changes relative to each other by increasing the diameter of the aperture. The intensity in the mode appearing in the upper part of the pictures is dominating and, therefore, considered as the main mode. The micropulse width increases from 1.4 ± 0.05 ps for an aperture of 3 mm up to 2.28 ± 0.18 ps for an aperture of 15 mm (i.e., when the whole beam is coupled into the HWG).

In Figure A.4, the transmission value of the $250 \mu\text{m}$ bore size HWG is displayed as a function of the size of the aperture in front of the coupling lens. This set of data represents the transmission measured for the well-aligned mode propagating in the HWG setup shown in Figure A.2, as well as the misaligned HWG setup shown in Figure A.3. No significant difference in the transmission of the 1.5 meter HWG was noted for these two setups. A transmission maximum of 54 ± 5 % is found for an aperture diameter of 12 mm which corresponds to an HWG inner diameter to spotsize ratio of 0.78 (Table A.1).

Figure A.5 shows the measurements of pulse width and beam profile for HWG with a bore size of $530 \mu\text{m}$. The beam profile reveals that many modes propagate through the 1.5 meter straight HWG. Some of the modes maintain their position for the different aperture diameters, but only change their intensity relative to each other. The pulse duration broadens up to 1.54 ± 0.14 ps for an aperture of 15 mm. The beam profile of the FEL and its native pulse width of 0.98 ± 0.06 ps are displayed for comparison.

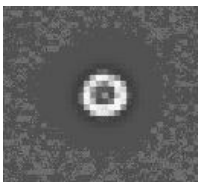
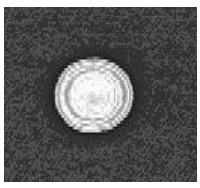
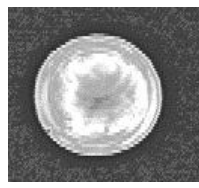
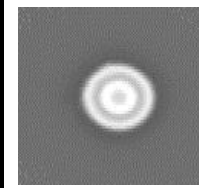
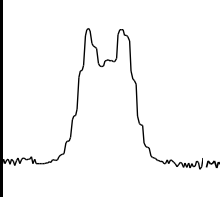
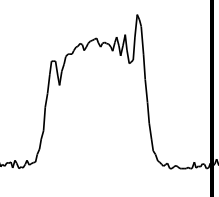
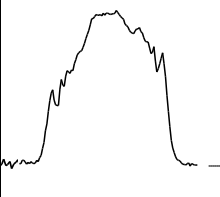
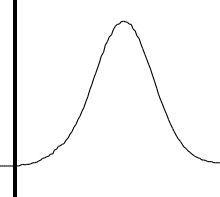
The data in Figure A.6 shows the results for the $530 \mu\text{m}$ bore size, 1.5 meter HWG bent into two loops (i.e., 720°) with a 9 cm radius. The beam profiles reveal several modes that remain almost constant in their position and relative intensity, independent of the aperture. The micropulse width broadens for each of the different aperture by about 0.2 ps, but the increasing trend as seen in Figure A.5 is not present.

Figure A.7 shows the transmission values for the 1.5 meter HWG with the bore size of $530 \mu\text{m}$. For the straight HWG the maximal transmission is around 83 % for an aperture of 12 mm and decreases to 53 % for an aperture of 3 mm. For the HWG bent into two loops (radius 9 cm), the transmission was measured to be 53 % for an aperture of 12 mm indicating the induced bending losses. The transmission decreases to 35 % if the aperture is reduced to a diameter of 3 mm.

A.4 DISCUSSION

Transmission, autocorrelation and beam profile measurements obtained for different coupling conditions makes it obvious that a precise alignment of the HWG with respect to the beam axis is critical. A coupling lens with a $f/\#$ of 11 is required to match the acceptance

Table A.1: Overview of the coupling conditions used in the experiments.

Aperture Diameter	3 mm	6 mm	12 mm	15 mm
f/#	100	50	25	20
Spotsize	624 μm	281 μm	195 μm	125 μm
Beamprofile 2D				
Beamprofile Trough the center				
Ratio 250 μm HWG	2.5	1.12	0.78	0.5
Ratio 530 μm HWG	1.18	0.53	0.37	0.24

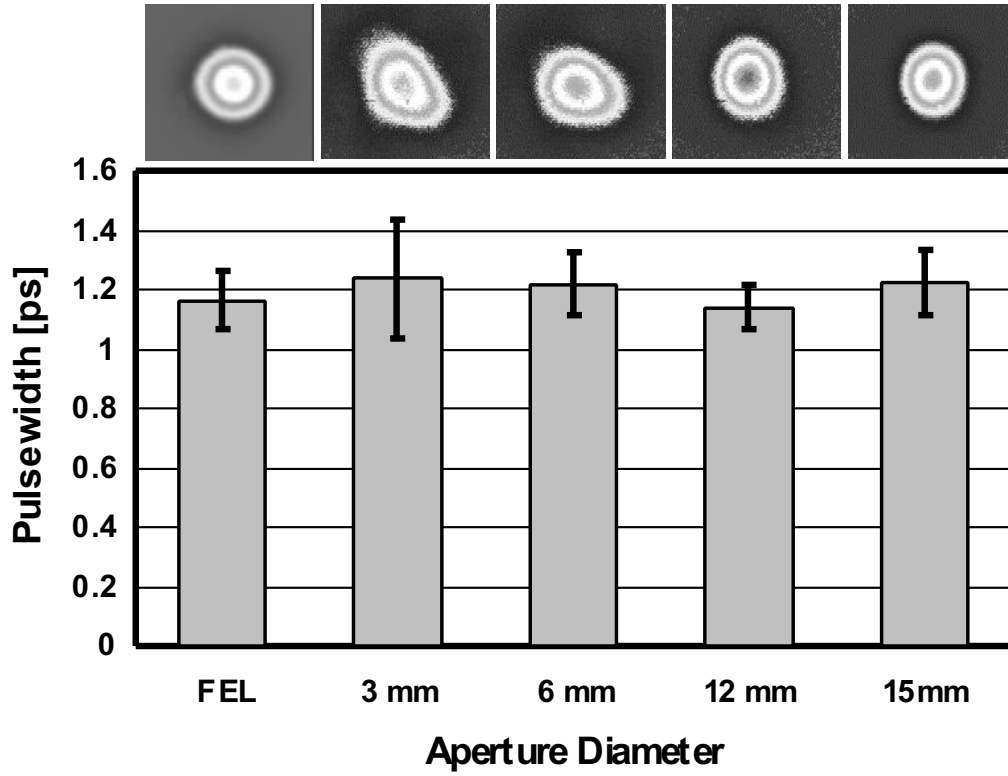


Figure A.2: Beam profile and micropulse width measured after transmission through a $250\ \mu\text{m}$ straight HWG. Coupling is aligned for optimal mode propagation.

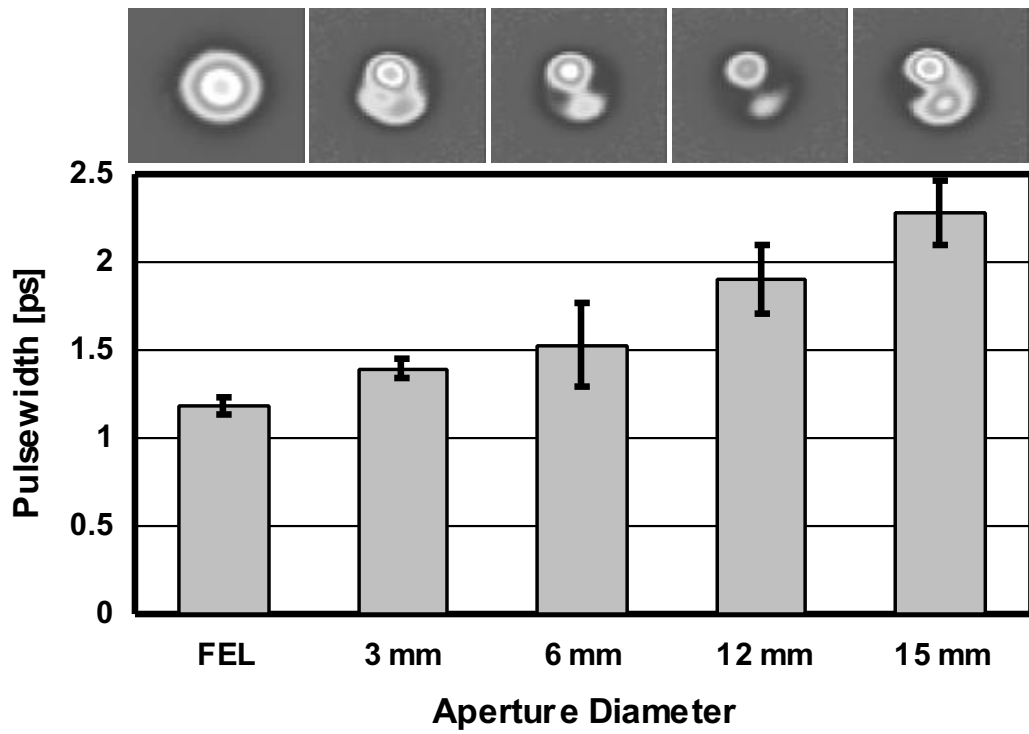


Figure A.3: Beam profile and micropulse width measured propagating in a misaligned $250 \mu\text{m}$ straight HWG.

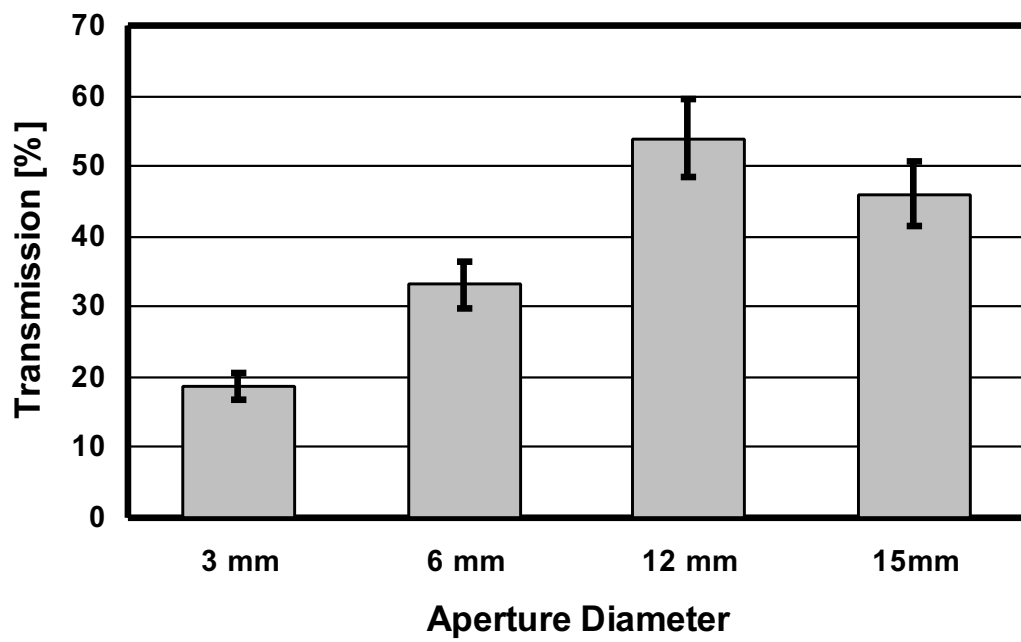


Figure A.4: Transmission through a straight 250 μm HWG (length = 1.5 m).

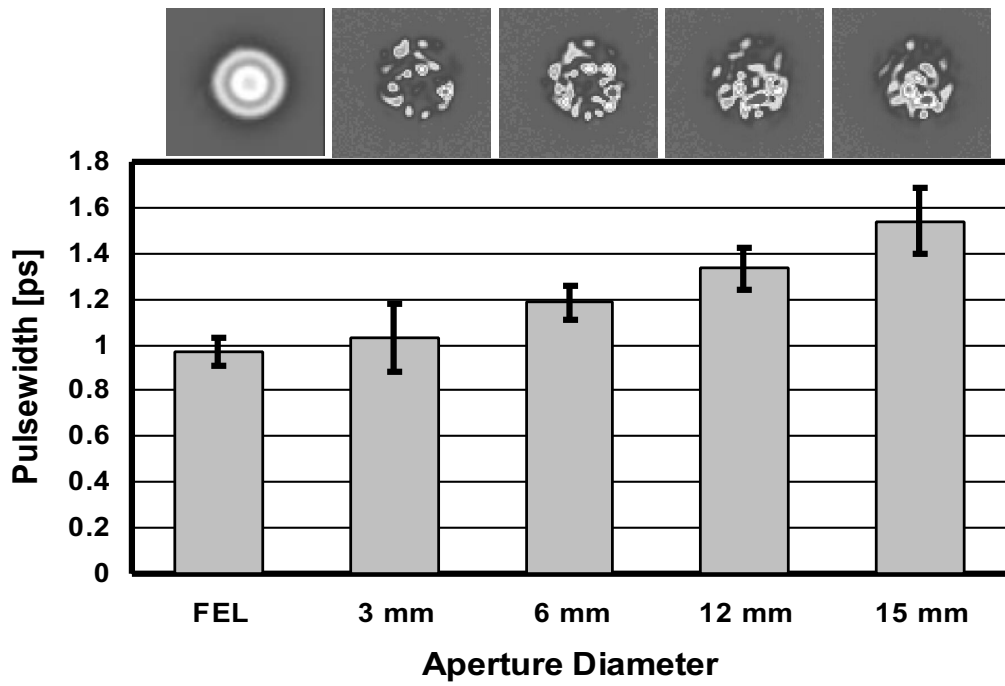


Figure A.5: Beam profile and micropulse width measured after transmission through a $530\ \mu\text{m}$ straight HWG.

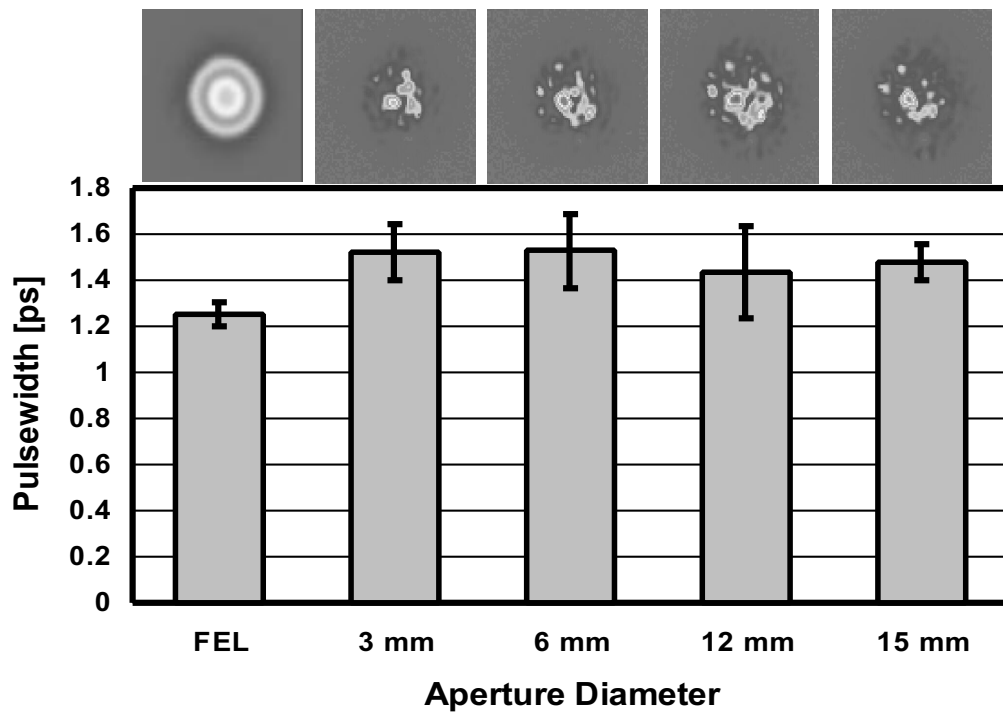


Figure A.6: Beam profile and micropulse width measured after transmission through a $530\ \mu\text{m}$ HWG bent through two loops (720° , bending radius = 9 cm.)

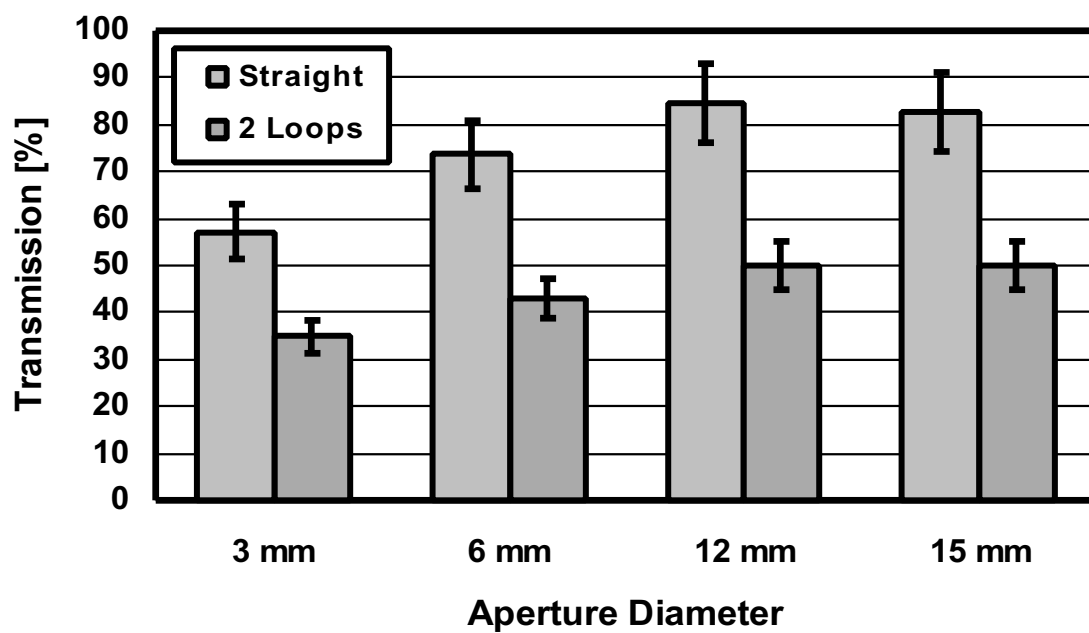


Figure A.7: Transmission through a straight and bent $530 \mu\text{m}$ HWG (length = 1.5 m, bending through 2 loops, bending radius 9 cm.)

angle of the HWG which was determined to be about 2.5° (half angle). This corresponds to a numerical aperture NA (equivalent) of 0.044 and was calculated from the beam profile diameter and the distance between the distal HWG end and the chip of the beam profiler. In our setup, a single lens with a constant focal length was chosen to investigate the influence of different $f/\#$ and spotsizes in a simple way. These parameters were obtained by reducing the opening of an aperture in front of the lens. Maximal transmission and best maintenance of the mode pattern is expected by using a spotsize diameter to HWG bore size ratio between 0.5 and 0.7 [11]. For a ratio larger than 1 (i.e., if the spotsize is larger than the bore diameter of the HWG) not all the energy in the beam can be transmitted. This is indicated by decreased transmission for smaller aperture diameters. The $250\ \mu\text{m}$ HWG has a lower transmission than the $530\ \mu\text{m}$ HWG because the transmission is inversely proportional to the third power of the bore radius [5]. Bending losses, which are inversely proportional to the bending radius, explain lower transmission of the $530\ \mu\text{m}$ HWG bent into two loops. Misalignment of the HWG with respect to the optical axis had no influence to the transmission (i.e., if the x-y misalignment was compensated with the angular adjustment) but had drastic impacts on the mode propagation and micropulse broadening.

The beam profiles through the HWG are often not as clean as the original FEL. The drastic effect of misalignment is obvious by comparing the results shown in Figure A.2 and Figure A.3 where the same coupling setup was used. In the smaller HWG, the low order mode propagation is independent of the aperture diameter. The effect induced by the change of the incident beam shape from Gaussian to flat top could not be investigated. The transmitted high-order modes can not be refocused as well as a Gaussian beam profile and this can be a drawback for interaction processes. Furthermore, it was confirmed that the polarization state of the beam is not maintained upon transmission through the HWG. Additionally, the modes are disturbed by misalignment of the coupling system and mechanical stress by pressing and bending the HWG, which can cause a significant change in the transmitted mode pattern [12]. The transmitted mode patterns were stable if the HWG lay untouched on the optical table; however, a movement or rearrangement of the HWG influenced the mode structure drastically. Using HWGs with a thicker glass wall may overcome this problem and are more resistant to external forces, but will also be less flexible. The transmitted profiles through the *unit*[530] μm HWG are not in agreement with the theory of maintaining the beam shape optimal and with minimal loss in the HWG if the spotsize to bore diameter ratio is between 0.4 and 0.7 [12]. A low-order mode propagation in the $530\ \mu\text{m}$ HWG was only achievable with drastic reductions in transmission. The transmitted mode pattern was independent of the aperture diameter; however, it changed the energy distribution significantly. Since more modes can theoretically propagate in larger diameter HWGs, these HWGs are more sensitive

to alignment and the influence of bending and pressing.

Significant micropulse broadening was found if the mode pattern propagating through a straight HWG consists of several modes. The pulse width increased for larger aperture diameters and therefore a smaller $f/\#$ of the coupling lens. For a reduced aperture, the contribution of the lower modes to the pulse width is dominant. It is speculated that the energy distribution in the higher modes is negligible compared to the energy transmitted in the main modes. The pulse broadening is less dominant if bending the HWG restricts the mode propagation. Results shown in Figure A.6 demonstrate an almost constant micropulse width in a bent HWG. This indicates that higher order modes are not propagating in the HWG, although the beam profile reveals that several lower order modes are propagating in the HWG. A geometrical ray model explains the significant pulse broadening investigated for the propagation of several modes. It is assumed that a ray, originating on the edge of the aperture, undergoes more reflections in the HWG and therefore travels a slightly longer distance than a ray that propagates on axis through the HWG. The path length difference is calculated considering the aperture diameter, the focal length and the length of the HWG. Assuming that the rays are propagating in the HWG with the speed of light in vacuum, the path length difference is converted to a delay time. In Figure A.8 the theoretical maximal pulse width increase is compared to the experimental findings. The experimental data represents the pulse width increase from the measurements shown in Figure A.3 and A.5 (absolute pulse width minus reference pulse width of the FEL). The model only predicts results in the right order of magnitude and does not take parameters like bore diameter, beam profile or bending into account. Therefore, it is not obvious why the temporal pulse broadening in the $530\ \mu\text{m}$ HWG is not as significant as for the $250\ \mu\text{m}$ HWG. It is speculated that the higher order modes may not propagate in the HWG and, therefore, do not transmit enough energy, which can contribute to a pulse broadening. The lower order modes do not undergo as much path length difference and, therefore, the pulse length is shorter for micro pulses traversing the $530\ \mu\text{m}$ HWG. The pulse broadening mechanism is explained by the propagation of transverse modes. Propagation of these mode structures can induce pulse broadening on the order of pico seconds. The accuracy of the autocorrelation setup and the fluctuations in the FEL (with the not bandwidth-limited pulses) did not allow the investigation of broadening mechanisms for single-mode propagation in HWG. The structural dispersion of the wave guide will broaden single-mode propagating pulses but should be investigated with femtosecond pulses.

Optimal performance of the HWG is only possible with optimal coupling conditions. A design for a coupling system for HWGs with different bore diameters (and adaptable to use with different wavelengths delivered from the FEL) must be considered to match the spotsize

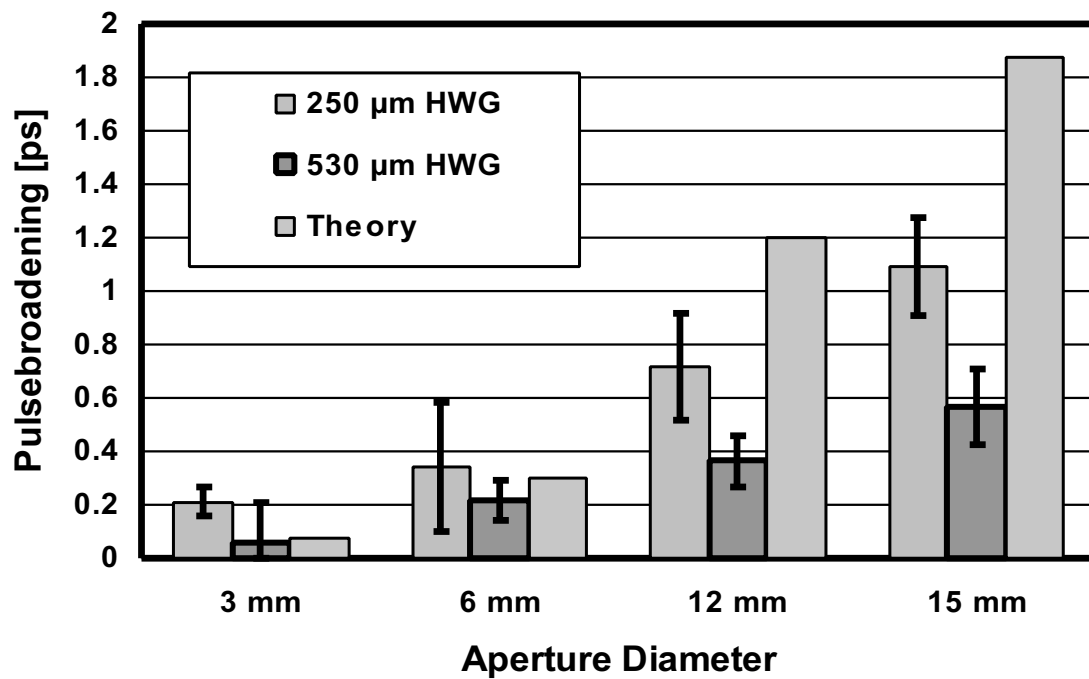


Figure A.8: Pulse broadening caused by propagation of a 1 ps FEL micropulse through 1.5 m HWG. Shown are the results of waveguides with bore sizes of 250 μm and 530 μm , and theoretical pulse broadening based on a simple theoretical model.

to bore diameter ratio of 0.5–0.7. Furthermore, a precise alignment of the HWG with respect to the optical axis is essential. The results of this study need to be taken into account for the design of a surgical probe [13]. Alteration of the FEL pulses propagating in HWGs is critical in terms of specifying the laser parameters delivered through a surgical probe. An increase in the micropulse duration by a factor of 2 reduces the pulse intensity (and thus peak power and peak radiant exposure) to half its original value. This needs to be considered if the underlying physical process in the laser-target interaction is not simply based on an average energy deposition value (e.g., threshold and break-down effects often correlates with the peak intensity rather than the average power of the incident pulse). Design consequences involve good protection of the HWG against mechanical stress. The HWG must be mounted in a way that does not degrade pulse propagation.

A.5 CONCLUSION

This study has demonstrated how critical the beam coupling setup for a HWG is for the delivery of a clean Gaussian pulse. Investigations on pulse broadening, propagated beam profile, and transmission measurements revealed induced changes on three critical parameters for interaction processes. Calculations based on a geometrical model delivers estimation of pulse broadening through a HWG at the right order of magnitude. The coupling condition should be as ideal as possible, which will result in one single mode propagating through the HWG with maximal transmission.

ACKNOWLEDGMENTS

The authors thank the FEL core group for running the laser so reliably and Dr. James Harrington (Rutgers University) for helpful discussion about the HWG. This study was supported by the ONR Contract No. N00014-94-1-1023 and the Swiss National Science Foundation.

REFERENCES

- [1] Edwards G, Logan R, Copeland M, Reinisch L, Davidson J, Johnson B, Maciunas R, Mendenhall M, Ossoff R, Tribble J, Werkhaven J, O’Day D, “Tissue ablation by a free-electron laser tuned to the amide II band,” *Nature*, 371:416–419, 1994.
- [2] Edwards G, “Biomedical and potential clinical applications for pulsed lasers operating near 6.45 μm ,” *Optical Engineering*, 34:1524–1525, 1995.

- [3] Edwards GS, Evertson D, Gabella W, Grant R, King TL, Kozub J, Mendenhall M, Shen J, Shores R, Storms S, Traeger RH, “Free-electron lasers: Reliability, performance, and beam delivery,” *IEEE Journal of Special Topics in Quantum Electronics*, 2(4):810–817, 1996.
- [4] Matsuura Y, Abel T, Harrington JA, “Optical properties of small-bore hollow glass waveguides,” *Applied Optics*, 34(30):6842–6847, 1995.
- [5] Matsuura Y, Matsuura K, Harrington JA, “Power delivery of free electron laser light by hollow glass waveguides,” *Applied Optics*, 35(27):5395–5397, 1996.
- [6] Gannot I, Inberg A, Oksman M, Waynant R, Croitoru N, “Current status of flexible waveguides for ir laser radiation transmission,” *IEEE Journal of Selected Topics in Quantum Electronics*, 2(4):880–889, 1996.
- [7] Brau CA, Mendenhall MH, “The vanderbilt free-electron laser center,” *Nuclear Instruments and Methods in Physics Research A*, 319:47–50, 1992.
- [8] Amirmadhi F, Brau C, Becker K, Mendenhall M, “New autocorrelation technique for the ir fel optical pulsewidth measurements,” *Nuclear Instruments and Methods in Physics Research A*, 375:427–429, 1996.
- [9] *Spiricon Operator’s Manual*, Spiricon, Inc., 1997.
- [10] Khosrofian JM, Garetz BA, “Measurement of a gaussian laser-beam diameter through the direct inversion of knife-edge data,” *Applied Optics*, 22(21):3406–3410, 1983.
- [11] Gregory CC, Harrington JA, “Attenuation, modal, and polarization properties of $n < 1$, hollow dielectric waveguides,” *Applied Optics*, 32(27):5302–5309, 1993.
- [12] Matsuura Y, Rabii CD, Matsuura K, Harrington JA, “Low order multimode generation in hollow glass waveguides,” *Electronics Letters*, 32(12):1096–1098, 1996.
- [13] Pratisto HS, Uhlhorn SR, Copeland M, Jansen ED, “Clinical beam delivery of the Vanderbilt FEL: Design and performance of a hollow waveguide based handheld probe for neurosurgery,” in *Specialty Fiber Optics for Medical Application*, Katzir A, Harrington JA, eds., vol. 3596, pp. 55–61, SPIE, 1999.